COMPUTATIONAL DESIGN AND EXPERIMENTAL VALIDATION OF DIAMOND-BASED QUANTUM EMITTERS

by

Oluseye Akomolede

A Dissertation

Submitted to the Faculty of Purdue University

In Partial Fulfillment of the Requirements for the degree of

Doctor of Philosophy

School of Electrical and Computer Engineering

West Lafayette, Indiana

December 2021

THE PURDUE UNIVERSITY GRADUATE SCHOOL
STATEMENT OF COMMITTEE APPROVAL

Dr. Peter Bermel, Chair

School of Electrical and Computer Engineering

Dr. Andrew Weiner

School of Electrical and Computer Engineering

Dr. Dimitrios Peroulis

School of Electrical and Computer Engineering

Dr. Daniel Elliot

School of Electrical and Computer Engineering

Approved by:

Dr. Dimitri Peroulis

To my family

ACKNOWLEDGMENTS

I acknowledge my advisor Peter Bermel for his help throughout the years.

TABLE OF CONTENTS

LIST OF TABLES

LIST OF FIGURES

ABSTRACT

The enhancement of the emission from nitrogen vacancy color centers will help facilitate advancements in quantum information technology. To this end, the reduction of the excited state lifetimes of NVs as well as the design of devices which support electroluminescence of nitrogen vacancies, as well as the broadband enhancement of the emission from these centers is of great importance.

In this study, we create diamond thin films containing nitrogen vacancy color centers using salt-assisted ultrasonic disaggregation techniques and electrophoretic deposition. These films are implanted with xenon atoms and the resulting structures are characterized optically. We report a reduction in the bulk emission lifetime of nitrogen vacancy color centers of two orders of magnitude. A coupled-mode theory approach is used to analyze the emission from the xenon-doped nanodiamond species. It is determined that the lifetime reduction occurs due to coupling between nitrogen vacancy color centers and xenon color centers within the diamond lattice.

A diamond field effect transistor is investigated via simulations utilizing Sentaurus TCAD software. The device is scaled by three orders of magnitude from previous experiments involving the same structure. Transport characteristics are obtained from simulation results. We confirm the existence of a decreasing saturation voltage with a decrease in gate length in the diamond field effect transistor. Further investigation into the device's viability as a quantum emitter is conducted.

The design of a single photon source utilizing plasmonic structures to enhance emission from nitrogen vacancy color centers is proposed. The plasmonic structure is investigated to extract operating parameters and to quantify the optical coupling and propagation characteristics for various physical dimensions

The design of a plasmonic device which features both electroluminescence via nitrogen vacancy color centers and their enhancement via plasmonic effects is numerically simulated. The device features large Purcell enhancement factor and good photon emission rate. In summary, this work paves the way towards the advancement of the nitrogen vacancy color center as a stable source of room temperature photons for quantum information applications.

1. INTRODUCTION

Over the course of several decades, there has been an advent of a new computing technology utilizing quantum mechanics. This new paradigm of computing may change the way that we interact with our world. Modern applications typically involve dilution fridges and cryogenic temperatures, but there is great interest to improve this technology, so that these computations can be performed at room temperature.

Quantum photonic emitters are a new platform that has sprung forth from those efforts. The unique properties, of these emitters, such as non-classical light emission, photon antibunching, and, in some implementations, photon indistinguishability, have made these objects a tool of great interest for applications in quantum information processing. These emitters are not without their shortcomings, however. The viability of quantum emitters is currently held back by their relatively low photon count rates, compared to classical (Poissonian) sources. These low rates are the result of their longer radiative lifetimes and low photon collection efficiencies.

Single photon sources are a type of quantum emitter that are of great importance to the field of quantum information technology. They can facilitate quantum entanglement [1], serve as an emitter for flying qubits [2], act as a framework for quantum key distribution [3], and are a robust technology for quantum information processing [4]. Several types of single photon sources currently exist, such as quantum dots [5], [6], attenuated lasers [7], and color centers within diamond [8]. Several of these single photon sources come with limitations, however. Quantum dots, for example, do not typically provide indistinguishable photons, though recent work shows promise in overcoming this design problem [9]. Attenuated lasers suffer from non-deterministic output; their output differs from true single photon emission due to a non-zero probability of obtaining two photons [10]. Therefore, the design problem at hand is to choose a single photon emitter capable of generating indistinguishable photons, preferably at room temperature.

Of particular interest is a quantum emitter found within bulk and nanometer sized diamond, known as the nitrogen vacancy (NV) color center. While the nitrogen vacancy color center does offer broadband emission and stable, room temperature single photon emission, significant advancements are required to position the nitrogen vacancy color center as the ideal quantum emitter for quantum information applications. One such enhancement is photon indistinguishability. NVs are currently limited in their generation of indistinguishable photons due

to four factors. The excited state lifetime of NV centers is relatively long (12 ns). Only a small fraction of NV emission goes into the zero phonon line (ZPL). The photon extraction efficiency out of diamond is limited due to its large refractive index. And finally, there are spectral fluctuations at random in the exact frequency of NV emission due to charge noise in the diamond itself [11]. Thus, to position the NV center for quantum information applications, one can improve their operation via various methods: lowering the excited state lifetime, increasing the extraction efficiency, and enhancing emission from the ZPL. The NV may also serve as a source of entangled single photons.

1.1 Nanodiamond Synthesis

For the creation of quantum photonic emitters, nanometer sized diamond is required for the integration with nanophotonic devices. These devices include photonic crystal cavities [12], plasmonic waveguides [13], [14], and plasmonic cavities [15]. The synthesis of nanodiamond remains an important study in the field of quantum optics.

There are many techniques available for the synthesis of nanodiamonds [16]. Common techniques include the detonation technique[17] laser assisted synthesis [18], high temperature high pressure (HTHP) high energy ball milling of microcrystalline diamond [19], and chemical vapor deposition (CVD) synthesis [20].

In the detonation technique, the energy of an explosion is used to synthesize nanodiamonds. There are three variants according to the carbon precursor that is used. In the first variant, graphite is transformed into nanodiamond using the energy of shockwaves originating from explosives. This technique is one of the popular methods to synthesize polycrystalline diamond particles [21]. The second variant involves explosives such as TNT, hexogen, octogen, or a mixture of these materials with a negative oxygen balance undergoing detonation in a closed chamber. In this variant, the explosives provide the required carbon and high energy for nanodiamond formation [22]. The chamber containing the explosives is usually filled with argon, nitrogen, CO_2 hydrogen or ice, which act as coolants. The third variant combines various compositions of explosives, such as RDX/Carbon and RDX/graphite and diamond precursors, yielding different nanodiamond products [23].

In the high energy ball milling technique, microsized diamond samples with haphazard shape are milled to produce nanodiamond particles. Quasi-spherical nanodiamond particles with

size below 10 nm have been synthesized [24]. This method involved nitrogen jet milling followed by bead milling and size selection.

The CVD technique is an incredibly popular method used to synthesize films of carbon nanostructures. These nanostructures include carbon nanotubes [25], graphene [26], and nanodiamonds [27]. In this method, carbon precursors in gas phase are used to deposit nanodiamond films. There are several techniques, such as Hot filament CVD [28], Microwave assisted CVD [29], and radio plasma enhanced CVD [30]. Nanodiamond sizes obtained using the various CVD methods range from 5 nm to several hundred nm [31], [32].

Apart from the creation of nanodiamonds, diamond nanostructures may also enable the creation of new optical technologies[33], [34]. With plasma-assisted reactive-ion etching as the primary fabrication technique, diamond nanostructures of several shapes and dimensions can be created to further facilitate integration with other nano-optical devices.

Many of these techniques incorporate the creation of nitrogen vacancy color centers, either as a byproduct of the nanodiamond synthesis, or as a step during the synthesis itself. The nitrogen vacancy color center in diamond is widely recognized as a leading candidate for the generation of single photons at room temperature, as will be explained next.

1.2 The Nitrogen Vacancy Color Center in Diamond

The nitrogen vacancy color center exists as a very attractive option for applications in quantum information and quantum computation. This is owing to previous experiments, which have shown nitrogen vacancy color centers to be capable of photostable single photon generation [35]–[37] as well as the capability to optically prepare and readout the electronic spin of the color center [38], [39]. The ability to manipulate and readout the electronic spin of NV^- color centers positions them as a possible solid-state spin qubit for quantum information processing and quantum metrology devices [40].

The NV center is a point defect in diamond with C_{3v} symmetry consisting of a substitutional nitrogen-lattice vacancy pair oriented along the [111] crystalline direction [40], [41]. This structure is shown in Fig. 1.1.

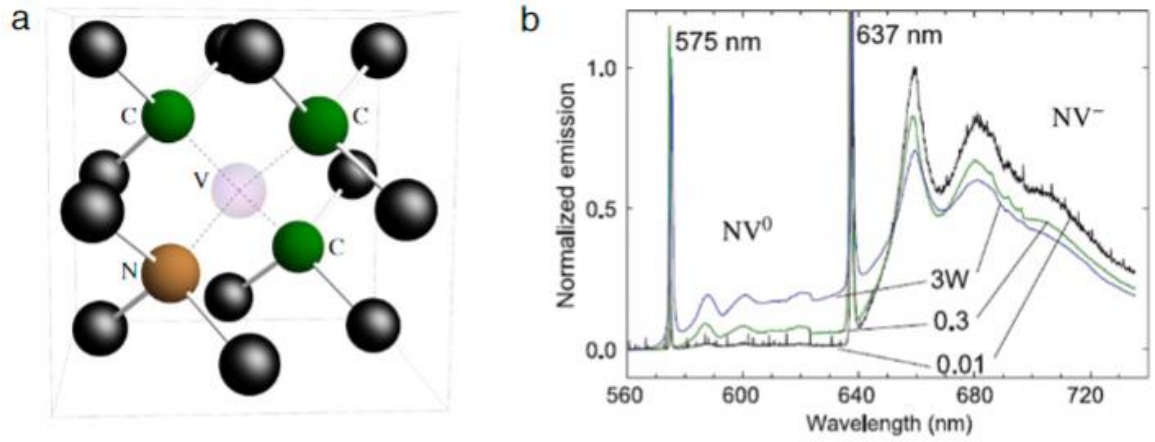

Fig. 1.1 The other carbon atoms are depicted in black. (b) Normalized emission spectra of an ensemble of NV^- and NV^0 color centers at different excitation powers. Source: (a) and (b) are reprinted from [40].

The NV center can be found 'in grown' during the CVD process [42], or as a product of radiation damage and annealing [43] or ion implantation and annealing in bulk and nanodiamond [44]. The nitrogen vacancy color center is known to have two charge states: negative NV^- and neutral NV^0 [45], [46]. The identifying features of these charge states are their optical zero phonon lines (ZPLs) at 1.945 eV (637 nm) and 2.156 eV (575 nm) for NV^- and NV^0 color centers respectively [47], [48]. Optically, these centers also exhibit vibronic bands that extend from their ZPLs to higher/lower energy in absorption/emission. Due to the sharp ZPLs and well-defined vibronic bands of NV^0 and NV^- color centers, it has been found that optical transitions within these color centers occur between discrete defect levels deep within the diamond bandgap such that the valence and conduction band levels are not involved in the optical transitions. Because of this, the NV center is known as a deep-level defect in diamond [45], [46]. The known aspects of the electronic structures of NV^- and NV^0 color centers are depicted in Fig. 1.2. This information allows us to understand electroluminescence in NV centers, as will be discussed next.

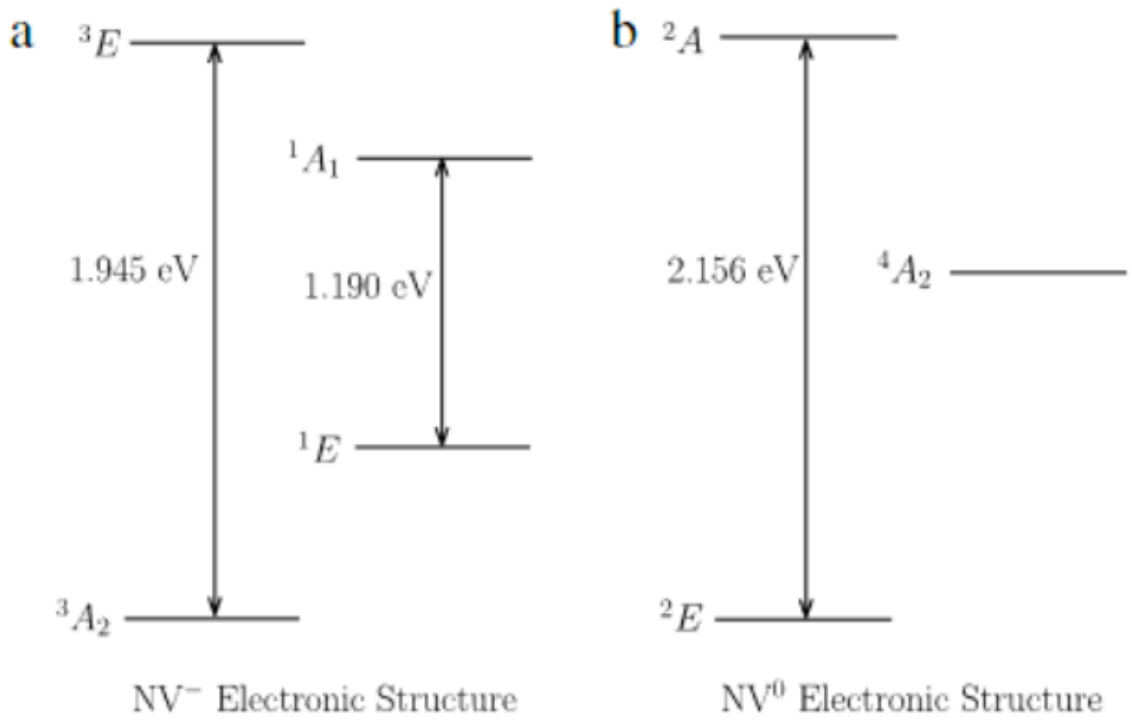

Fig. 1.2 Schematics of (a) known information of the NV^- electronic structure [49] and (b) known aspects of the NV^0 electronic structure [50]. The observed infrared and optical ZPLs are indicated. Source: (a) and (b) are reprinted from [40].

1.3 Electrical Generation of Single Photons Through Charge Capture Processes

Another attractive feature of nitrogen vacancy color centers is the ability to electrically stimulate single photon emission via recombination at the color center [51]. The basic principle for electroluminescence in NV centers can be understood as a three-stage process (Fig. 1.3).

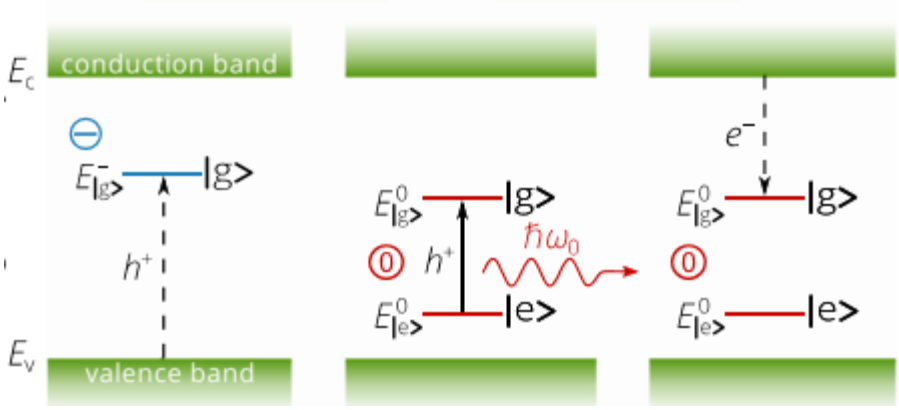

Fig. 1.3 Illustration of the three-stage process of single photon emission via electrical injection from the nitrogen vacancy color center in diamond. In the first stage, a hole is trapped by the negatively charged NV^- color center and brings it to the excited level. At the same time, the hole trapping alters the charge of the NV to the neutral state and changes its energy level structure. The trapped hole appears at the excited state for holes in the neutral center, which is the excited state of the NV^0 center. In the second stage, the NV^0 relaxes to the ground state via photon emission. In the final stage, the NV^0 center returns to the initial negative charge state via the capture of an electron. Source: figure reprinted from [51].

We assume the color center to be negatively charged in equilibrium. A negatively charged defect is an attractive center for holes and has a large capture cross-section σ_p of up to 10^{-12} cm^2 due to the low mobility of free carriers in heavily doped diamond [52]. The NV^- accepts a hole from the valence band of diamond, which alters its charge state to neutral and changes its energy level structure. Simultaneously, a hole is trapped into the excited level, which is the excited level for holes in the neutral center [53]. This level corresponds to the excited state of the NV^0 center [54]. Following this, the excited state of the NV^0 relaxes to the ground state via radiative transition. The wavelength of the emitted photon corresponds to that of an optically excited NV^0 color center. Finally, the color center returns to its initial negatively charged state via the capture of an electron with a capture cross section σ_n of about 10^{-15} cm^2.

By considering a detailed balance between the radiative transition from the excited level to the ground level, electron and hole trapping from the conduction and valence bands in diamond to the NV center, and thermal carrier escape from the NV back to the conduction and valence bands, the photon emission rate R_{ph} in the steady state can be expressed as

$$R_{ph} = \Phi c_n n \frac{\left(1 + \frac{p_1}{p} + \frac{n_1 p_1}{np}\right) f - \frac{n_1 p_1}{np}}{1 + \frac{p_1}{p} + \frac{c_n n_1}{c_p p}} \tag{1.1}$$

Here, Φ is the quantum efficiency, n and p are the electron and hole densities respectively, c_n and $c_p$are the electron and hole capture rate constants. Finally, n_1 and p_1 are the electron and hole equilibrium carrier densities when the fermi level in diamond corresponds with the ground level of the NV^- color center and the excited level of the NV^0 color center. Lastly, f is the occupation probability of the neutral ground state, which is given by

$$f = \frac{1}{c_n n} \frac{1 + \frac{c_n n_1}{c_p p} + \frac{p_1}{p}\frac{c_n n_1}{1/\tau}}{\frac{1}{c_n n} + \frac{1}{c_p p}\left(1 + \frac{n_1}{n}\right) + \tau\left(1 + \frac{p_1}{p} + \frac{n_1 p_1}{np}\right)}, \tag{1.2}$$

where τ is the excited-state lifetime. If the ground and excited levels of the color center are located deep within the bandgap of diamond, the effective densities n_1 and p_1, which represent thermal emission rates from the NV center to the conduction and valence bands, are reduced to zero, and the photon emission rate R_{ph} is simply defined as the inverse of the sum of the three inverse rates: electron capture rate ($c_n n$), hole capture rate ($c_p p$) and transition rate from the excited to ground level ($1/\tau$).

$$R_{ph} = \Phi \frac{1}{\frac{1}{c_n n} + \frac{1}{c_p p} + \tau} \tag{1.3}$$

Electroluminescence from nitrogen vacancy color centers can allow for robust devices suited to quantum information applications. Another way by which the stable room-temperature emission of single photons can be improved is via the enhancement of emission from NV centers. The field of plasmonics offers robust solutions to this end.

1.4 Plasmonic Enhancement of Nitrogen Vacancy Color Center Emission

Plasmonic nanostructures are an attractive option to increase the detected fluorescence rate of NV centers as they can offer direction emission along with high Purcell broadband enhancement across the NV spectrum [55], [56], which has not been demonstrated in NV-coupled dielectric nanostructures [57]. The basic principle for the enhancement of emission from NVs follows from

the fact that the coupling of emitters to a resonator mode allows for modification of the excited state lifetime, spectral distribution and spatial spontaneous emission (SE) pattern [58]–[61]. This coupling rate can be optimized by maximizing the quality factor to mode volume ratio of the resonant mode [51]. Plasmonic cavities offer an attractive platform for maximizing the coupling rate due to their small mode volumes, which yield large Purcell enhancement factors [63]. These small mode volumes follow from the ability of plasmonic systems to localize light in volumes significantly smaller than the diffraction limit of light [63].

1.5 Justification of the Thesis

Many of the concepts presented in this thesis are in their infancy with very little experimental demonstration or commercial application. There have been recent experiments showing the ability to enhance and guide emission from nitrogen vacancy color centers using silicon nitride waveguides [246]. There has also been recent work showing experimental validation of the enhancement of NV photoluminescence via plasmonic cavity [247]. A group has also shown the electrical generation of single photons experimentally using charge capture processes for NVs situated in a p-i-n diode [248]. These results represent groundbreaking advances within the field, but many of them are still in the proof-of-concept regime. Thus, this work succeeds in advancing the field by advocating for more robust and mature designs that offer performance metrics that exceed these experimental works. This thesis is situated within the cutting edge of work involving the enhancement of NV emission for quantum information applications.

1.6 Outline of the Thesis

To position the nitrogen vacancy color center as a reliable source of single photons for quantum information applications, the enhancement of their emission is of paramount importance. This thesis will first focus experimental demonstration of emission enhancement via the reduction in NV excited state lifetime via doping (Chapter 2). It will then discuss numerical simulation of potential devices to further enhance emission from NVs via electro generation of single photons, plasmonic enhancement, or both methods (Chapter 3 to 5). The following outlines the content and significance of each chapter.

- Chapter 2 experimentally demonstrates the reduction of the excited state lifetime of nitrogen vacancy color centers via doping with xenon impurities. A coupled-mode theory model is employed to understand the mechanism by which the lifetime reduction occurs.
- Chapter 3 introduces the design of a highly scaled diamond field effect transistor utilizing transition metal oxide deposited onto a hydrogen terminated diamond layer. Transport characteristics are quantified before the device is evaluated as a potential source of room-temperature single photons via electroluminescence.
- Chapter 4 discusses the design of a plasmonic cavity for enhanced NV emission. The plasmonic cavity uses an asymmetrical design to achieve different propagation and coupling features which allows for its use in a wide variety of nanophotonic applications involving NV centers.
- Chapter 5 introduces the design of a plasmonic device capable of electroluminescence via NVs. This device also combines the electroluminescence capability with enhancement of emission of single photons via a plasmonic cavity, which is incorporated into the device design itself.

2. XENON IMPLANTATION OF NANODIAMOND FILMS FOR TARGETED COLOR CENTER EMISSION AT SUB-NANOSECOND TIME SCALES

Previously Published in Optical Materials Express:
O. Akomolede and P. Bermel, "Xenon implantation of nanodiamond films for targeted color center emission at sub-nanosecond time scales," *Optical materials express*, vol. 11, no. 8, p. 2369, 2021, doi: 10.1364/OME.431743.

2.1 Introduction

Quantum information technology is a rapidly growing field that calls for technologies that prepare, evolve, and measure quantum bits (qubits) to be successful [64]. Evolution technologies that allow qubits to be transferred and interact optically are likely to include solid-state optical quantum emitters [65]. Quantum emitters, comprising a host of technologies such as quantum dots, rare earth impurities, and color centers in diamond have many applications. They can produce indistinguishable single photons on demand [66]–[70], enable interactions between single photons[71], and can store and process quantum information in the spin states[72]–[74]. Quantum emitters can also sense electromagnetic fields[75], [76] at nanoscale dimensions. The color centers in nanodiamond are an example of a set of quantum emitters that have been studied extensively[77].

Many varieties of nanodiamond color centers have been evaluated, such as iron, titanium, and xenon[77]. Each one exhibits different optical properties. The nitrogen-vacancy (NV) color center is the most commonly studied color center with over 50 years of research[78].

The NV center is a point defect in diamond with C_{3v} symmetry consisting of a substitutional nitrogen-lattice vacancy pair oriented along the [111] crystalline direction. It is created in the chemical vapor deposition of diamond, or by radiation damage and annealing, or by ion implantation and annealing in bulk and nanocrystalline diamond. The NV center is known to have negative (NV^-) and neutral (NV^0) charge states. These charge states are identified by their optical zero phonon lines (ZPLs) at 1.945 eV (637 nm) and 2.156 eV (575 nm) respectively[79]. The associated vibrionic bands extend from their ZPLs to higher/lower energy in absorption/emission.

Both charge states of the NV color center have been identified as room temperature single photon sources[80]–[82]. This was confirmed through statistically-significant antibunching dips observed through second-order autocorrelation measurements [often abbreviated as $g^{(2)}(\tau)$].

While NV color centers offer the attractive feature of room temperature single-photon emission, one of the key obstacles to the utilization of nitrogen vacancy color centers in quantum information technologies are their long bulk emission lifetimes, typically 80 ns [83]. These lifetimes do not support the fast repetition rates necessary for most quantum information applications [84].

Attempts have been made to shorten the emission lifetimes of NVs using various methods, such as coupling to surface plasmons [83], modifying the substrate refractive index[85], [81]or introducing radiation induced lattice defects (RILDS) [86]. These methods have been largely successful, but come with various tradeoffs, such as decreased emitter intensity when applying RILDs, or difficult and irregular construction when plasmonic methods are utilized.

In this work, we describe a precise fabrication method for the shortening of NV color center lifetimes while preserving their broadband emission and intensity.

We discuss first the fabrication and initial optical characterization of nanodiamond films and their subsequent ion implantation with xenon. The post-implant optical characterization is discussed before concluding with an analysis of our findings using coupled mode theory. In our analysis, we create a model of our system using idealized components, and the associated coupled-mode system of equations. Next, we solve the system of equations to obtain analytical expressions for the spectral intensity lifetime before generating a Voigt profile, representing our model's frequency response, that is in good agreement with the experimentally observed lineshape of our color centers.

2.2 Methods

We conducted the nanodiamond film assembly process in two stages: film deposition and ion implantation. In the first stage, we created a very dense film to increase the chances of successful ion implantation using the Salt-Assisted Ultrasonic disaggregation (SAUD) [85], [86][87]–[91]. In the second stage, ion implantation of xenon was performed at Sandia National Laboratories.

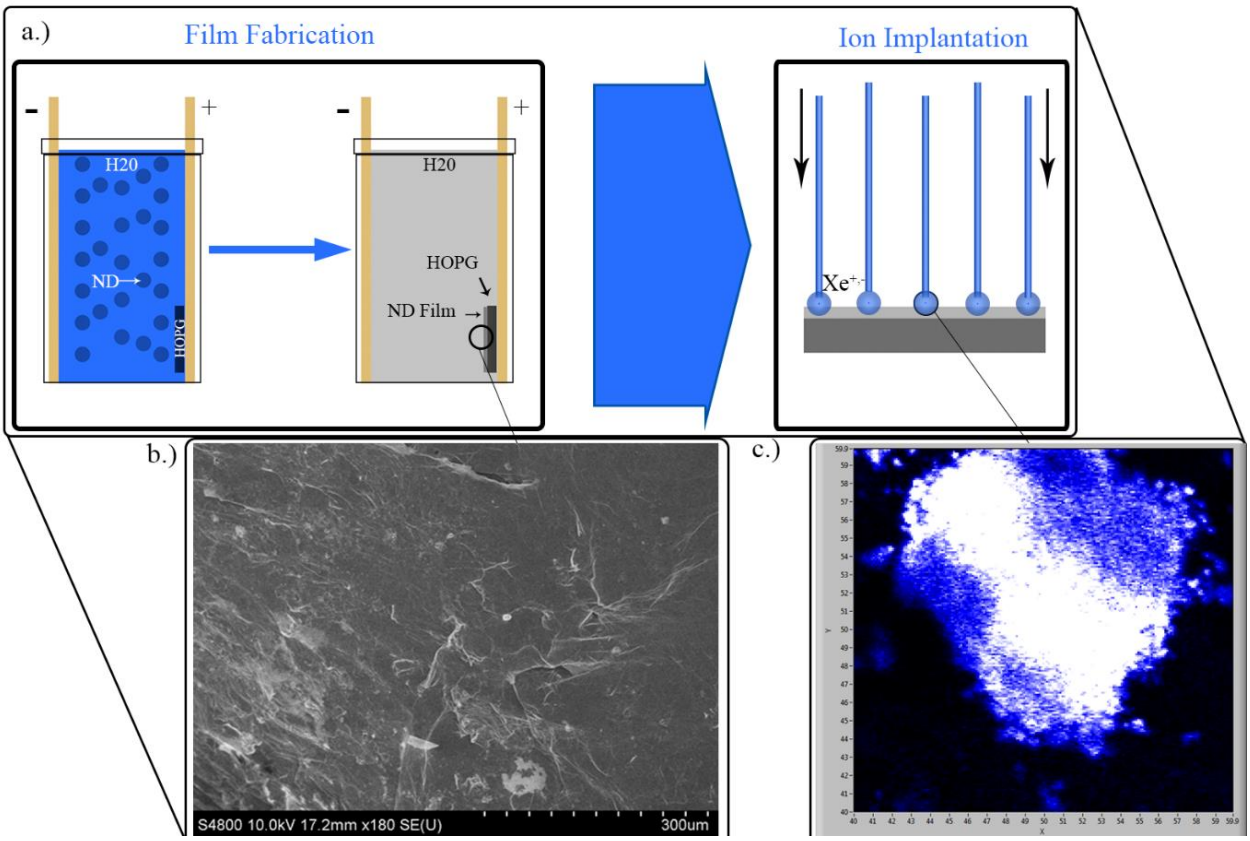

Fig. 2.1 Process flow diagram for Xe color center fabrication. a.) A nanodiamond film is deposited using disaggregated nanodiamonds in solution via electrophoretic deposition prior to ion implantation. b.) The resultant film is characterized via scanning electron microscopy and reveals good surface coverage. c.) The resulting film is implanted with Xe species at a fluence of $\mathbf{10^{14}\ ions/cm^2}$; the resulting color centers are characterized via scanning photoluminescent (PL) spectroscopy (this image has a field of view of 20x20 μm^2).

All optical characterization was performed using a custom-made scanning confocal microscope. Further details of all these procedures are included in the supplementary information provided.

2.3 Results and Analysis

2.3.1 Film Characterization

Dynamic Light Scattering (DLS) measurements were conducted with the Malvern Zetasizer ZS Nano. Post-SAUD, DLS measurements indicated that the z-average (intensity-weighted mean hydrodynamic size of the particles) decreased from 43 nm to 18 nm, with a

polydispersity index decrease from 0.203 to 0.100. After analysis of the surface with a scanning electron microscope, the film was deemed to have good surface coverage.

Photoluminescence Spectroscopy was subsequently performed on the film with a custom scanning confocal microscopy setup. PL measurements revealed the presence of several color centers. Those color centers were analyzed, and a spectrum matching with that of a typical nitrogen-vacancy (NV) Color Center was observed from all regions of the film investigated.

2.3.2 Optical Characterization

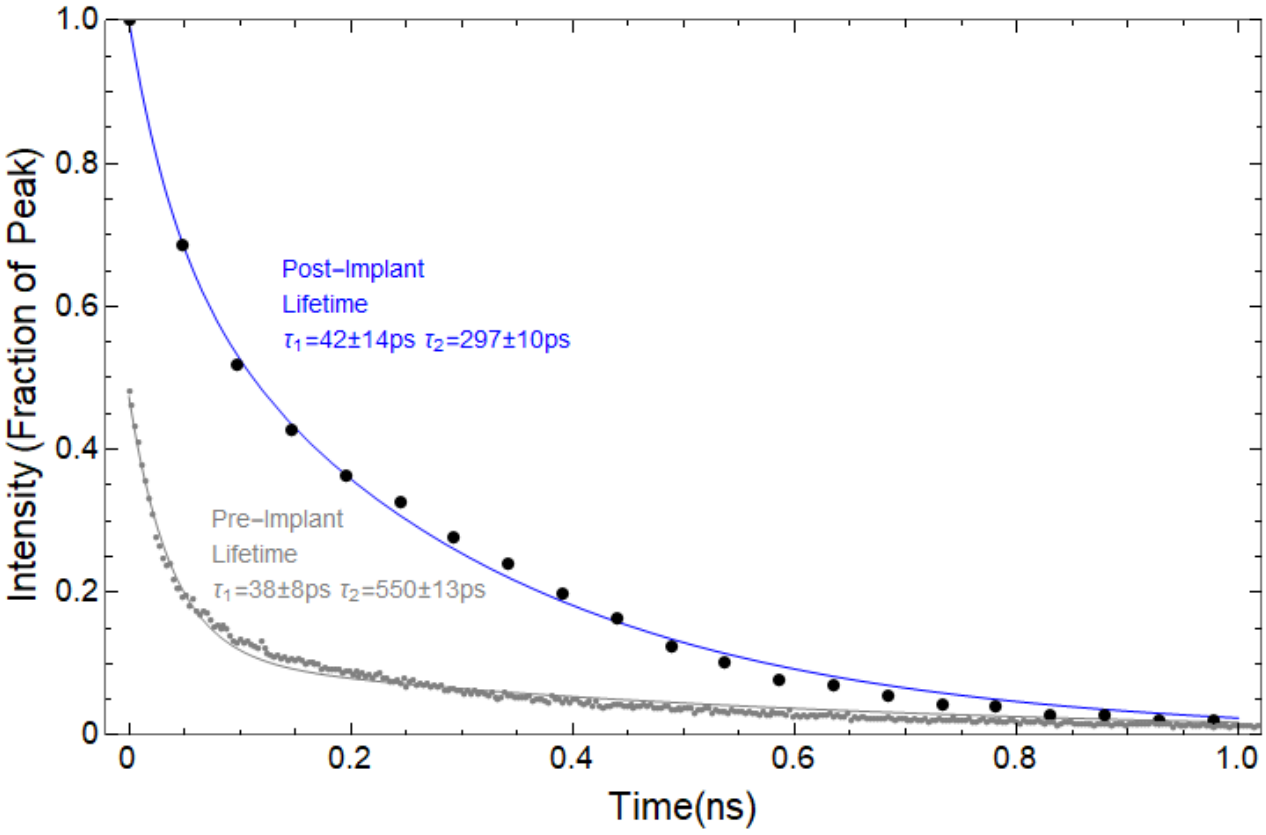

Fig. 2.2 Lifetime measurements are conducted on pre-implant (gray) and post-implant (blue) color center species. Pre-Implant and post-implant data is represented by the grey and black circles, respectively. Post-Implant color centers show a bulk lifetime of $\boldsymbol{\tau_2}$ =297 ps. This is a 43% reduction in bulk lifetime compared to pre-implant color centers. The sharp decline in the pre-implant data is due to the higher contribution of surface effects ($\boldsymbol{\tau_1}$ = 38 ps) in the observed fluorescence.

The film was implanted with xenon ions at Sandia National Laboratories, and subsequently annealed at 500°C for one hour. After implantation, the film was optically characterized using the same custom scanning confocal microscopy setup and was found to still contain several color

centers. The spectrum shows a peak at ~624 nm. This peak is red-shifted by 30 nm with respect to previous experiments, where photoluminescence spectroscopy was performed on nanodiamond agglomerates[87], as well as previous work detailing the size dependence of fluorescent nanodiamond emission[88]. Previous experiments have shown that the emission spectrum of nitrogen vacancy color centers will vary according to excitation wavelength [89], [90][91] Our excitation wavelength was 532 nm, while the previous xenon-related work was excited at 514.5 nm. In this previous work, a characteristic NV^0 zero phonon line (575 nm) was reported for samples annealed at 700℃, showing good evidence of the contribution of NV-related emission in samples annealed at these temperatures. Our measured spectrum is also very similar to previous experiments involving the implantation of xenon into type 1A diamond [91]. Combining these papers supports our understanding that the measured spectrum reflects fluorescence from nitrogen-vacancy color centers.

Several scans were conducted, and no photobleaching was observed. Fluorescence lifetime measurements of color centers within the film were conducted at random within the field of view, which was made possible by the abundance of individual color centers. The measured lifetimes of color centers within the film were remarkably short (below 1 nanosecond), and displayed low variance across the sample, as expected, given the fluence rates of the implantation.

In our experiment, the measured fluorescence lifetimes of the color centers within the film typically exhibit a bi-exponential relationship, with two exponential lifetimes τ_1 and τ_2. The longer lifetime, τ_2, is typically associated with color centers within the bulk of the nanodiamond, while the shorter lifetime τ_1 is associated with surface effects[83], [86].

Results from time-resolved photoluminescence are provided in Fig. 2.2. The fluorescence lifetime of implanted color centers within the bulk were found to be $\tau_2 = 297$ ps, with the surface effect lifetime $\tau_1 = 42$ ps. This is a remarkable reduction in lifetime for nitrogen vacancies in nanodiamond, which typically have a fluorescence lifetime on the order of 40-80 ns [86]. A comparison to pre-implantation lifetimes yielded a similar bi-exponential relationship with the surface-associated lifetime $\tau_1 = 38$ ps and the bulk lifetime $\tau_2 = 550$ ps. The pre-implant bulk lifetime observed can be attributed to the presence of C-Centers (single nitrogen substitution within the lattice), as has been reported in the literature[86], since the pre-Implant diamonds were type 1A diamonds that are known to contain several C-Centers[86]. The intensity of the post-implant fluorescence compared with the pre-implant fluorescence was also measured, and the post-implant

fluorescence intensity was approximately twice that of the pre-implant fluorescence intensity. The two fluorescence measurements are documented in Fig. 2.2. The observed sharp decay from the pre-implant species is due to the higher contribution of surface effects ($\tau = 38$ ps) in the observed fluorescence.

Several attempts were made to explain the peculiar fluorescence characteristics of the post-implant film, such as the introduction of additional point C-Centers or other radiation-induced lattice defects. The results, specifically the increase in fluorescence intensity, the relatively unchanged surface lifetime, and shortening of only the bulk lifetime, are contrary to the predictions of prior work. The literature predicts a shortening of both bulk and surface lifetimes, as well as the lowering of the fluorescence intensity of nitrogen vacancy color centers as the number of C-Centers and other lattice defects grows [84]. This quenching effect is from the creation of non-radiative energy transitions within the ground and excited states of the nitrogen vacancy color centers. As these effects are not present here, it is fair to assume a different mechanism is responsible for the decreased lifetime, and increased fluorescence of the color centers. Coupled-mode theory calculations can be employed to help elucidate this mechanism in detail.

2.4 Discussion

Coupled mode theory was developed in the 1950s to analyze and design of a broad range of devices including microwave traveling-wave tubes, parametric amplifiers, oscillators, and frequency converters. Central to the theory is the analysis of lossless resonances, and their coupling to similarly lossless waveguides, and one-another. The theory serves as an approximate, yet insightful and accurate mathematical description of the electromagnetic oscillations and wave propagation for coupled systems [92]–[94].

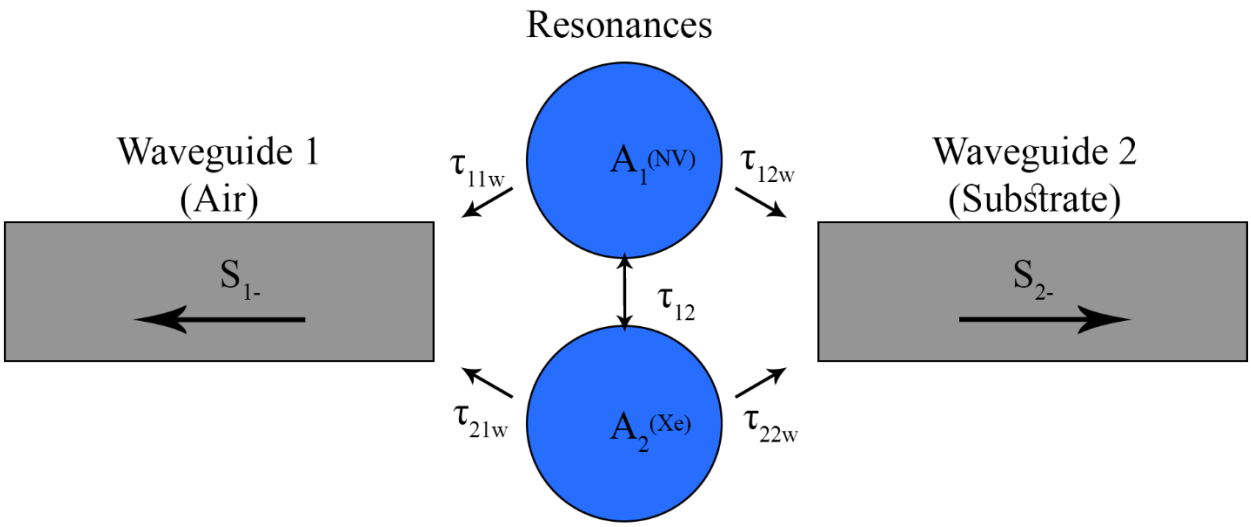

Fig. 2.3 Schematic diagram showing the essential features of our coupled-mode theory model: two single-mode waveguides 1, and 2, with output field amplitudes $\boldsymbol{s_{1,2-}}$; two resonances of field amplitudes $\boldsymbol{A_{1,2}}$ and fequencies $\boldsymbol{\omega_{01,02}}$ coupled to waveguides 1 and 2, and one another with lifetimes $\boldsymbol{t_{11w}}$, $\boldsymbol{t_{12w}}$, $\boldsymbol{t_{21w}}$, $\boldsymbol{t_{22w}}$, and $\boldsymbol{t_{12}}$. $\boldsymbol{s_{1,2-}}$ are normalized so that $\left|\boldsymbol{s_{1,2-}}\right|^2$ is power in the waveguide, and $\boldsymbol{A_{1,2}}$ are normalized so that $\left|\boldsymbol{A_{1,2}}\right|^2$ is energy in the cavities.

For the purposes of our analysis, we considered only the lifetime reduction associated with the nitrogen-vacancy color center in the bulk. The system was described as a two-resonator system with the field amplitudes of the lowest-order resonator modes in each resonator given by A_1 and A_2, corresponding to resonator 1 and 2 respectively. Each resonator possesses a resonant frequency denoted by $\omega_{01,02}$. A coupling term representing the weak coupling between the resonators was denoted by τ_{12}. In our analysis, resonator 1 represents our pre-implant nitrogen-vacancy color center while resonator 2 represents a typical Xe color center and we consider asymmetric and symmetric coupling between the two resonances. This two-resonator system is symmetrically coupled to two identical waveguides representing the propagation of EM waves in air on one side, and into the substrate on the other. These waveguides are known as waveguides 1 and 2, respectively. The coupling constants of resonance 1 to waveguides 1 and 2 are given by τ_{11W}, and τ_{12W}. The coupling constants of resonance 2 to waveguides 1 and 2 are given by τ_{21} and τ_{22w}. All coupling constants are known via experiment or the literature. The resonances and coupling constants give rise to two simultaneous differential equations for symmetric coupling:

$$\frac{dA_1}{dt} = -i\omega_{01}A_1 - \frac{1}{\tau_{11w}}A_1 - \frac{1}{\tau_{12w}}A_1 - \frac{1}{\tau_{12}}A_1 + \frac{1}{\tau_{12}}A_2 \qquad (2.1)$$

$$\frac{dA_2}{dt} = -i\omega_{02}A_2 - \frac{1}{\tau_{21w}}A_2 - \frac{1}{\tau_{22w}}A_2 - \frac{1}{\tau_{12}}A_2 + \frac{1}{\tau_{12}}A_1 \tag{2.2}$$

The case of asymmetric coupling between resonances 1 and 2, with energy coupling from resonance 1 to resonance 2, was also investigated with corresponding rate equations:

$$\frac{dA_1}{dt} = -i\omega_{01}A_1 - \frac{1}{\tau_{11w}}A_1 - \frac{1}{\tau_{12w}}A_1 - \frac{1}{\tau_{12}}A_1 \tag{2.3}$$

$$\frac{dA_2}{dt} = -i\omega_{02}A_2 - \frac{1}{\tau_{21w}}A_2 - \frac{1}{\tau_{22w}}A_2 + \frac{1}{\tau_{12}}A_1 \tag{2.4}$$

A schematic corresponding to the system is provided in Fig. 2.3. The solution for the symmetrically coupled resonances involves a second order differential equation. It yields the following roots:

$$r_{1,2} = \frac{-i(\omega_{01}+\omega_{02}) - \left(\frac{1}{\tau_{11w}}+\frac{1}{\tau_{12w}}+\frac{1}{\tau_{21w}}+\frac{1}{\tau_{22w}}+\frac{2}{\tau_{12}}\right)}{2} \pm \frac{\sqrt{\left[i(\omega_{01}-\omega_{02}) + \left(\frac{1}{\tau_{11w}}+\frac{1}{\tau_{12w}}-\frac{1}{\tau_{21w}}-\frac{1}{\tau_{22w}}\right)\right]^2 + \left(\frac{2}{\tau_{12}}\right)^2}}{2} \tag{2.5}$$

The coupling term, τ_{12}, was found by matching the field amplitude A_1 with our post-implant experimental spectral measurement results shown in Fig. 2.4, and was found to equal 647.5 ps. The solution for the asymmetrically coupled resonances contains a single exponential term:

$$r_1 = -i\omega_{01} - \left(\frac{1}{\tau_{11w}} + \frac{1}{\tau_{12w}} + \frac{1}{\tau_{12}}\right) \tag{2.6}$$

As in the symmetrically coupled regime, τ_{12} was found to equal 647.5 ps. Therefore, we cannot use the decay rate alone to distinguish between the symmetric and asymmetric descriptions.

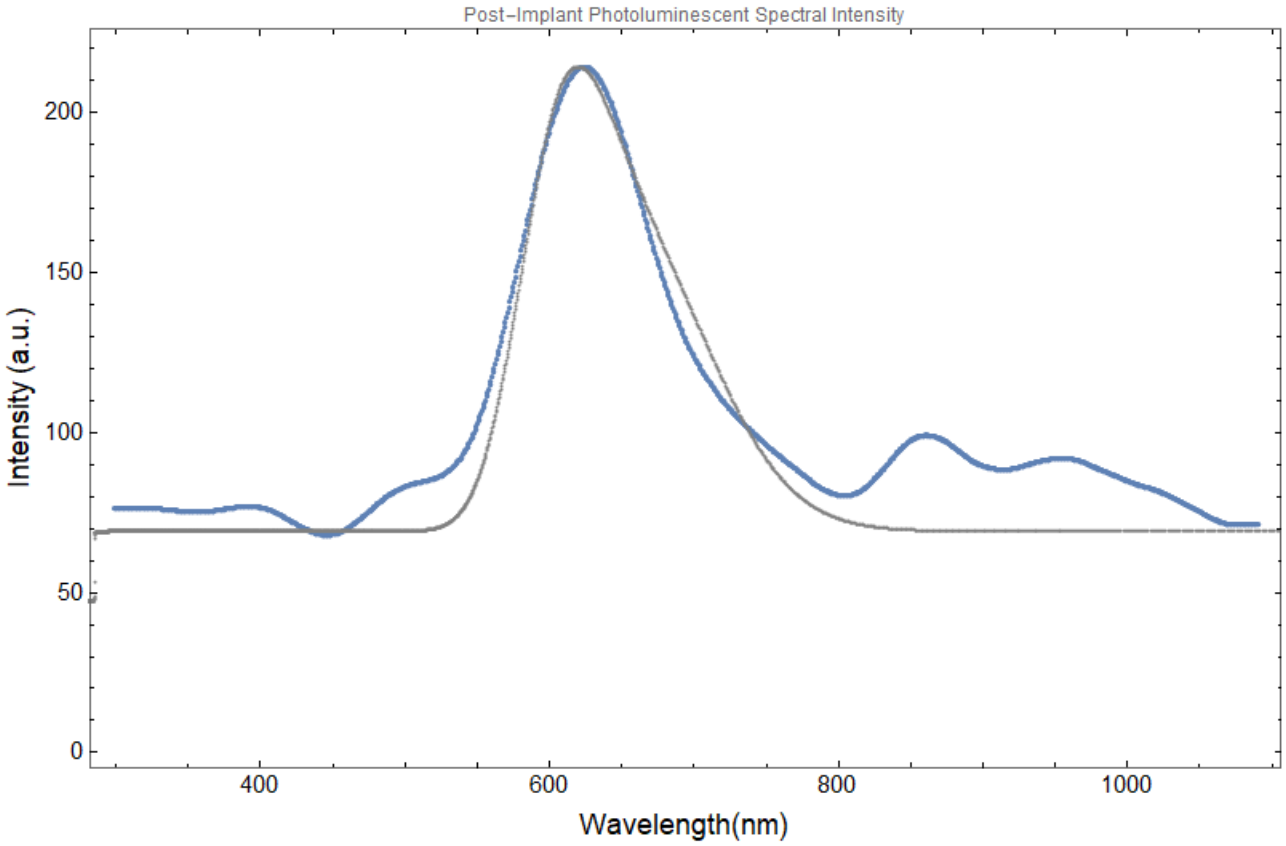

Fig. 2.4 Photoluminescence spectrum of post-implant color centers (blue) with Voigt profile generated by coupled-mode system of equations overlaid in grey. A good match between our experiment and theoretical analysis is achieved by considering inhomogeneous broadening effects, specifically strain broadening, within the diamond sample.

The decay rate and field amplitude A_1, when evaluated in the symmetric and asymmetric coupling frameworks, showed a good match with the bulk lifetime decay and intensity measured in our post-implant color centers. The spectral data was also considered. Our measured spectral intensity shown in Fig. 2.4 features a strong peak at 624 nm that likely results from inhomogeneous broadening, or vibrionic broadening as measured in previous experiments involving NVs [95]. In both cases, we would expect a Gaussian broadening to be induced by the presence of these phenomena. To investigate this, our coupled-mode system of equations was solved in the frequency domain. In both coupling frameworks, this output features two Lorentzian peaks with linewidths less than 1 nm, corresponding to two resonances with peaks at 637 nm and 811 nm. These were then convolved with a single Gaussian with standard deviation of 85 nm, representing inhomogeneous broadening effects, and the resulting Voigt profiles generated for both coupling frameworks shows a good match with our measured results. A Voight profile results from the convolution of two broadening mechanisms, one which would produce a Gaussian profile,

typically inhomogeneous broadening, and the other would produce a Lorentzian profile, likely homogeneous broadening. Voigt profiles are common in many branches of spectroscopy.

It is a fair assumption that inhomogeneous broadening effects are prevalent throughout our sample and contribute to the observed lineshape. Nanodiamonds feature several defects with a range of surface functionalizations [96]. These defects give rise to strain broadening, which is an inhomogeneous broadening effect arising from differences in the local environment of emitters at different spatial locations[97]. This Voigt profile generation method has been used previously to describe other diamond color center species, specifically silicon-vacancy color centers [98] where inhomogeneous distributions have also been observed. Therefore, it can be concluded that the observed lineshape is predicted by our coupled-mode analysis. Another explanation may involve vibrational broadening effects observed in previous experiments involving NVs [95]. Vibrational transitions, and their associated lineshape broadening, could also be responsible for our observed photoluminescence spectra. The distinction between these two hypotheses is not resolved by either the time-domain or frequency-domain data, and thus will require additional investigation in future work.

From our results, it appears the coupling of nitrogen-vacancy color centers and xenon color centers within nanodiamonds gives rise to an overall lifetime reduction. This reduction in lifetime is not accompanied by a reduction in intensity, as is typical of shunting effects due to nitrogen-vacancies coupling to other lattice defects, such as C-centers and A-centers. Instead, we observe an almost two-fold increase in intensity. Coupled-mode theory provides a suitable explanation for these effects.

2.5 Summary

In conclusion, we have shown that the implantation of xenon into nanodiamonds and subsequent annealing gives rise to an increase in color center intensity as well as a reduction in color center lifetime. Our measured pre-implant lifetime was 550 ps, while our measured post-implant lifetime was 297 ps. This corresponds to a lifetime reduction of 46%. We employed coupled-mode theory to determine that this lifetime reduction is consistent with a coupling between the nitrogen-vacancy and xenon color centers in the bulk, corresponding to a coupling time constant of 647.5 ps. These parameters were also consistent with the observed spectral

lineshape, described by a Voigt profile with two Lorentzian peaks at 637 nm and 811 nm that is convolved with a single Gaussian reflecting inhomogeneous broadening effects.

Our method of lifetime shortening lacks many of the drawbacks of other conventional methods, such as a decrease in emitter intensity and difficult fabrication requiring specialized equipment prone to user error. Instead, quantum emitters produced with our method feature increased emitter intensity and simpler fabrication. Ion implantation and subsequent annealing serves as an attractive option for the fabrication of room-temperature quantum emitters.

The results obtained within the work address a shortcoming of the nitrogen vacancy color center in its application towards quantum information: its excited state lifetime and thus its repetition rate of single photon emission. An alternate approach to address this fundamental issue while also providing a method for on-demand operation would involve the electrical stimulation of single photon emission. Diamond field effect transistors are an attractive option to realize this technology.

3. MODELING AND SIMULATION OF A HIGHLY SCALED DIAMOND FIELD EFFECT TRANSISTOR WITH QUANTUM INFORMATION APPLICATIONS

3.1 Introduction

Quantum information processing is a rapidly growing field supported by photonic quantum emitter technologies. Many examples of photonic quantum emitters have been proposed, such as recent work involving fluorescent toluene molecules [99] and semiconductor quantum dots[100]. Photonic emitters are one of the fundamental systems for a large variety of quantum technologies, such as quantum metrology [101], quantum communication [102], and quantum computing [103], [104]. Photonic quantum technologies require an efficient, on-demand, and entangled sources of highly indistinguishable single photons [105]. The nitrogen vacancy (NV) color center within diamond exists as a highly attractive photonic quantum emitter, capable of single photon emission at room temperature [106]. The NV center is a point defect in diamond with C_{3v} symmetry consisting of a substitutional nitrogen-lattice vacancy pair oriented along the [111] crystalline direction. It is created in the chemical vapor deposition of diamond, or by radiation damage and annealing, or by ion implantation and annealing in bulk and nanocrystalline diamond. The NV center is known to have negative (NV^-) and neutral (NV^0) charge states. These charge states are identified by their optical zero phonon lines (ZPLs) at 1.945 eV (637 nm) and 2.156 eV (575 nm) respectively [107]. The associated vibrionic bands extend from their ZPLs to higher/lower energy in absorption/emission.

The optical triggering of NV transitions and their subsequent spectral response has already been extensively studied [108]–[112], but recent developments involving diamond field effect transistors may enable the electrically triggering of NV optical transitions. Many designs of diamond field effect transistors have been proposed [113]–[115], but recent experimental work involving hydrogen-terminated diamond and transitional metal oxides (TMOs) shows great promise [116]. The hydrogen-termination of diamond is constructed using surface transfer doping (STD), which gives rise to a subsurface two-dimensional hole gas (2DHG) [117], [118]. The 2DHG channel can be exploited for quantum emission purposes. As demonstrated experimentally in recent work, incorporating a thin transition metal oxide layer [119]–[126], namely H_yMoO_{3x}, enhances the stability of the 2DHG. H_yMoO_{3x} is an attractive material for this purpose because,

like most TMOs, it features a large electron affinity, a high robustness to the transistor fabrication process, and offers good electronic energy level alignment with the 2DHG channel [116].

Although these findings were a significant advance for the field, the physical dimensions of this previous work are too large for applications involving plasmonic structures. The design features a gate length of 24 μm, which is too long for any integration with photonic cavities, or other quantum platforms. Thus, it would be of great interest to scale the design to smaller dimensions that would be more conducive to optical, plasmonic, and/or quantum applications. In this study, we characterize the design and performance of a highly scaled diamond field effect transistor and its potential applications to quantum information processing. The device in question has a scaled gate length of 24 nm – 3 orders of magnitude smaller than prior work, and more comparable to the dimensions of current state-of-the-art CMOS processes. We first conduct simulations using Sentaurus TCAD software to confirm the transport characteristics of the scaled diamond field effect transistor and compare those transport characteristics to a device modeled after previous work, thus validating the model chosen. In the course of our simulation, we confirm the existence of short channel effects, such as the decrease in drain saturation voltage V_{Dsat} and drain current overshoot, associated with the scaled gate length. Sentaurus is also employed to extract quantum parameters, such as the electrostatic potential profiles at different operating gate-source voltages and the hole wavefunctions and eigen-energies at zero bias conditions. A time-dependent perturbation theory model is employed to calculate the hole transition rates from the obtained ground state and excited state wavefunctions at differing gate-source and drain-source bias conditions using Fermi's golden rule. Our simulations predict the enhancement of the hole transition rate within the 2DHG by increasing the drain-source current within the device. Finally, a new design is proposed for the electrical triggering of Nitrogen Vacancy Color Centers located at the diamond/TMO interface using charge capture processes.

3.2 Numerical Model

Sentaurus TCAD by Synopsys is a commercial semiconductor device simulation software with the capability to solve the Poisson equation coupled to the electron and hole continuity equations on a discretized domain represented by a mesh of a given structure. By specifying certain parameters, the equations can account for quintessential semiconductor quantities, such as Fermi-statistics for carrier concentrations, doping-dependent mobilities, the effective masses of electrons

and holes, the conduction and valence band density of states for electrons and holes, band to band tunneling, and generation and recombination phenomena. The device under investigation is a three-layer device as shown in Fig. 5(a). The device layers consist of a 20 nm thick gate oxide layer with a gate length, L_g of 24 nm on top of a TMO layer of 4 nm thickness comprised of hydrogenated molybdenum trioxide. This layer contains the source and drain contacts with total length of 102 nm and a gate-source and gate-drain separation of 15 nm. The third layer is the diamond layer, which is 26 nm thick. The material parameters for HfO_2 were supplied with the Sentaurus TCAD software. The material parameters for the diamond and hydrogenated molybdenum trioxide layers are compiled from various sources [113], [116], [127]–[133] and are summarized in Table 1. The device parameters for molybdenum trioxide are readily available from many sources, however hydrogenated molybdenum trioxide has not been studied extensively. To estimate the effects of the incorporation of hydrogen into the molybdenum trioxide lattice, a constant active acceptor doping profile of 1.27×10^{15} cm^{-3} is incorporated into the device structure, spanning the entire hydrogenated molybdenum trioxide region. The two-dimensional hole gas channel is represented using a constant linear active acceptor doping profile situated between the hydrogenated molybdenum trioxide and diamond layers. This doping profile has a value of 3.75×10^{21} cm^{-3}. Figure 1(b) depicts the band structure under zero bias conditions of the device with the gate oxide layer on the left. At the interface between the TMO and diamond layer, the two-dimensional hole gas is predicted by the proximity of the valence band to the electron and hole quasi-fermi potentials. For the contacts, a series resistance of 2.25 MΩ is applied. In order to confirm the validity of the model, a separate device with gate length L_g of 24 μm, consistent with previous experiments, is also investigated.

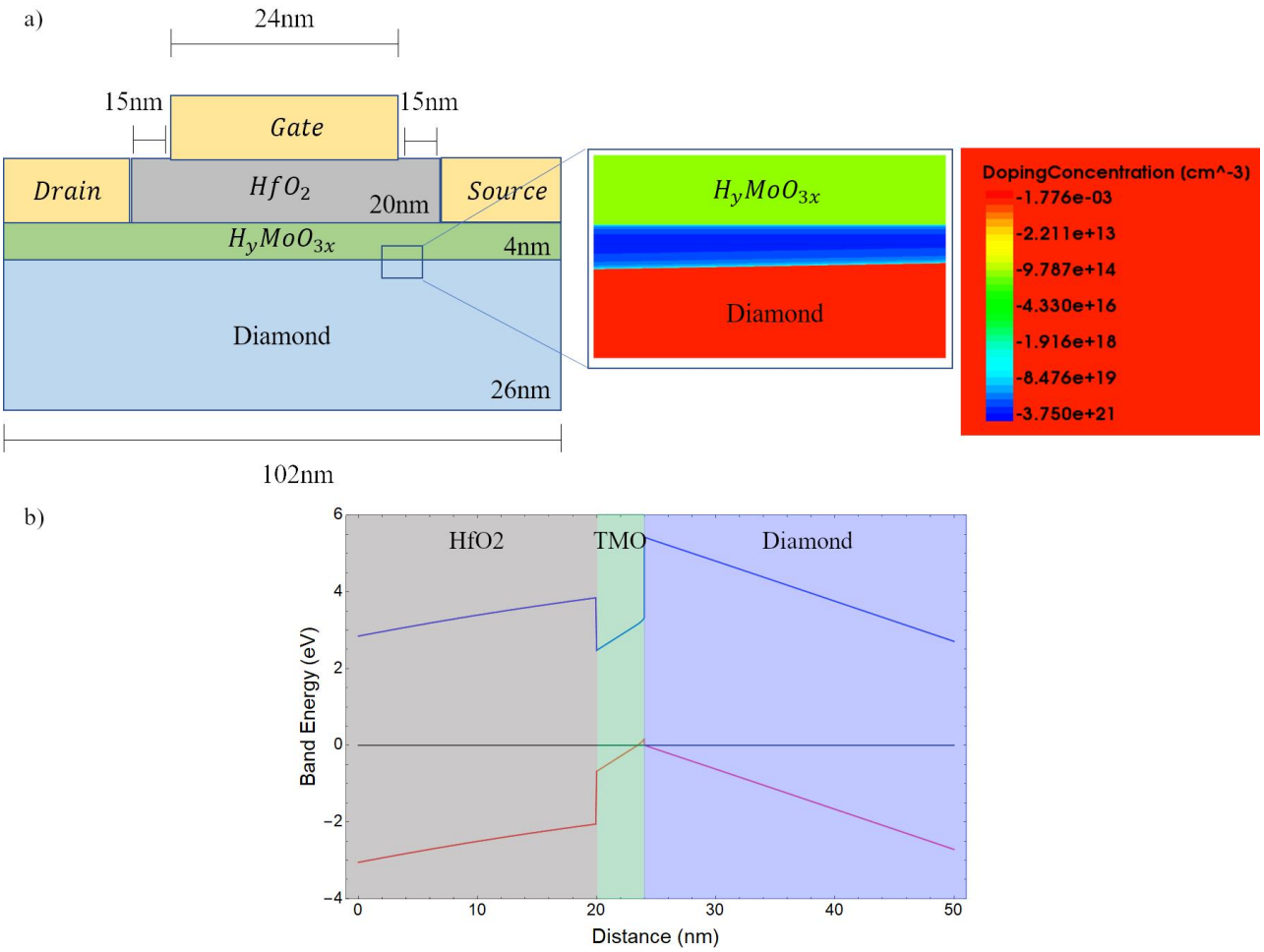

Fig. 3.1 (a) Schematic Design of diamond field effect transistor showing (from top to bottom) HfO_2, TMO, and diamond layers. Inset shows the doping profile of acceptors forming the 2DHG (b) Accompanying band diagram showing formation of 2DHG at TMO/Diamond interface

Table 3.1. Diamond and Molybdenum trioxide device parameters. Hydrogenated molybdenum trioxide is simulated using constant acceptor doping profiles.

Diamond Parameter	**Value**	**Reference**
epsilon	5.7	[134]
Bandgap (eV)	5.47	[128]
Electron Affinity (eV)	1.3	[129]
Maximum Electric Field (MV/m)	20	[128]
Electron Mobility ($\mathrm{cm}^2/\mathrm{Vs}$)	20.2	[117]
Hole Mobility ($\mathrm{cm}^2/\mathrm{Vs}$)	20.2	[117]
Thermal Conductivity ($\mathrm{W/cm \cdot K}$)	20	[128]
Hole Saturation Velocity <100> ($10^7 \mathrm{cm/s}$)	1.1	[114]
Electron Saturation Velocity <100> ($10^7 \mathrm{cm/s}$)	1.5	[114]
Hole Density of States (cm^{-3})	1.80E+19	[114]
Electron Density of states (cm^{-3})	6.41E+19	[114]

Molybdenum Trioxide Parameter	**Value**	**Reference**
Epsilon	4.5997	130]
Bandgap (eV)	3.2	[117]
Electron Affinity (eV)	3.4	[131]
Electron Mobility ($\mathrm{cm}^2/(\mathrm{V \cdot s})$)	1100	[132]
Hole Mobility ($\mathrm{cm}^2/(\mathrm{V \cdot s})$)	1100	132]
Thermal Conductivity (W/(cm·K))	0.241	[133]
HyMoO3 Work function (eV)	5.9	[117]

3.3 Device Simulation

Device simulation is carried out using Sentaurus Device software package for a variety of gate-source and drain-source voltages to characterize the transport characteristics of the proposed design. Fermi statistics are utilized in the simulation along with a high-field saturation mobility model. For recombination, Schottky-Reed Hall recombination is employed. Due to the relatively high bandgap of diamond ($E_g = 5.47$ eV) [127] and its relatively low electron affinity (1.3 eV) [128], a robust simulation strategy involving increased meshing at the diamond/TMO and TMO/HfO_2 interfaces, combined with numerical methods such as line search damping and relative error control is required to ensure simulation convergence.

$I_d - V_d$ plots are obtained by ramping the gate contact voltage to the desired value followed by slowly ramping the drain contact voltage in increments of 1 mV to the desired value of -10 V before extracting the current using supplied tools in the Sentaurus workbench suite. $I_d - V_g$ plots are obtained by ramping the drain contact voltage to the desired value of -6 V before

ramping the gate contact voltage in increments of 1 mV from -3 V to 3 V. For calculations involving the stimulated emission transition rate of holes within the two-dimensional hole gas, the non-perturbed wavefunctions, their associated eigen-energies, and the electrostatic potential at various gate bias conditions are required. The non-perturbed wavefunctions and their associated eigen-energies are obtained via solving Schrodinger's equation for holes on a nonlocal mesh spanning the entirety of the TMO region and penetrating 10 nm into the diamond region. The electrostatic potential within the same region under differing bias conditions is extracted from the simulation results using Sentaurus Visual software package. The matrix element involved in the calculation of the hole transition rates in the two-dimensional hole gas is computed numerically using MATLAB.

3.4 Results and Discussion

The obtained electrical characteristics of the device representing previous experiments (gate length L_g of 24 μm) is shown in Figs. 3.2(a) and 3.2(b) and are in good agreement with the experimental results from previous works [116]. In agreement with experimental data, the simulated diamond field effect transistor displays p-type behavior. Present is the well saturated output characteristic with an ON/OFF ratio of several orders of magnitude, as previously reported. This validates the model and shows that the supplied parameters accurately predict the performance of the previous experimental work. When applying the model parameters to a device with gate length L_g of 24 nm, there is a major difference in the $I_d - V_d$ output characteristic as shown in Figs. 3.2(c) and 3.2(d). The results predict the existence of "short-channel" effects associated with the scaling of the gate length by three orders of magnitude from 24 μm, as reported in the literature, to a new value of 24 nm. Of particular interest is the "current overshoot regime" that the model predicts for devices at this scale.

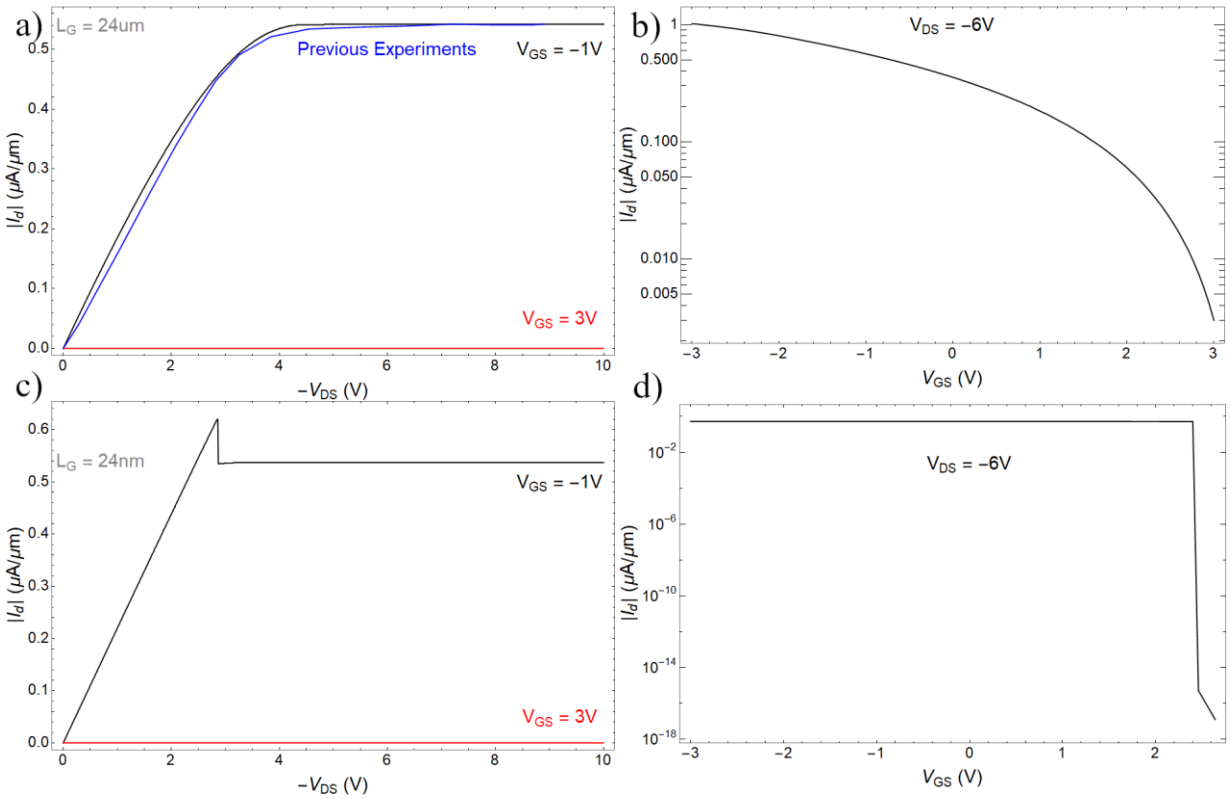

Fig. 3.2 Diamond FET transport characteristics. (a) and (b) ON/OFF Transport characteristics of diamond FET with gate length of 24um representing previous works. Shown in blue is curve representing previous experiments. (c) and (d) transport characteristics of the highly scaled diamond FET displaying p type behavior. Of note is the lower saturation voltage preceded by the "current overshoot" regime.

In the current overshoot regime of the 24 nm device's transport characteristic, we observe drain-source current larger than saturation, followed by a rapid decay to the saturation current. Current overshoot occurs in semiconductors because of the nonequivalence of the energy relaxation time and the momentum relaxation time for carriers [244].

Current overshoot decay in sub-micron field effect transistors at large drain biases, corresponding to the saturation drain current region, is caused by the rapid decrease of the momentum relaxation time arising from the effect of velocity-randomizing intervalley scattering [245].

There exists an interest to study the potential of the device if utilized to facilitate an electrical triggering of the emission of single photons via stimulated emission. The valence band offset which creates the 2DHG defines the confined energy levels, and the allowed optical transitions. This is modeled as a two-level system with ground state wavefunction and eigen energy ψ_a and E_a and excited state wavefunction and eigen energy ψ_b and E_b respectively. The

wavefunctions and eigen-energies are calculated using Sentaurus Device's built-in Schrodinger equation solver on a nonlocal mesh. The basic concept for device operation would involve a sinusoidal voltage applied at the gate of the device which would cause the holes within the two-dimensional hole gas to transition between the ground and excited states. The potential within the region would take the form

$$V(t) = V(\vec{r})\cos(\omega t) \tag{3.1}$$

Where $V(\vec{r})$ is calculated using Sentaurus Device. The perturbed Hamiltonian is given by:

$$H'(t) = q\,V(\vec{r})\cos(\omega t), \tag{3.2}$$

which is just the electrostatic potential within the region multiplied by the elementary charge q. The final form of the transition rate, given by Fermi's golden rule simplifies to

$$\Gamma = \frac{\pi q^2 |V_{ba}|^2}{2\hbar^2} \times \frac{\omega_0^2}{\pi^2 c^3} \tag{3.3}$$

where

$$V_{ba} = \langle \psi_b | V(\vec{r}) | \psi_a \rangle \tag{3.4}$$

represents the matrix element and

$$\omega = \omega_0 = \frac{E_b - E_a}{\hbar} \tag{3.5}$$

is the driving frequency. The second term of equation 3 is simply the photonic density of states given in the literature[134], [135]. The driving frequency ω_0 is calculated to be $3.53 \times 10^{13}\ \mathrm{s}^{-1}$ which comes from the estimated energy difference between the ground state and excited state eigen-energies of 0.146 eV. A sinusoidal potential with an amplitude of 1 V applied at the gate of the diamond field effect transistor is found through calculations to yield a transition rate $\Gamma = 2.436 \times 10^7\ \mathrm{s}^{-1}$ This is comparable to previous works that report optical transitions at ~150 kHz [136], though it exceeds those previous works. This transition rate can be further modulated by the application of varying gate source voltage amplitudes and varying drain-source voltages across the channel. The results of simulations are detailed in Fig. 3.3.

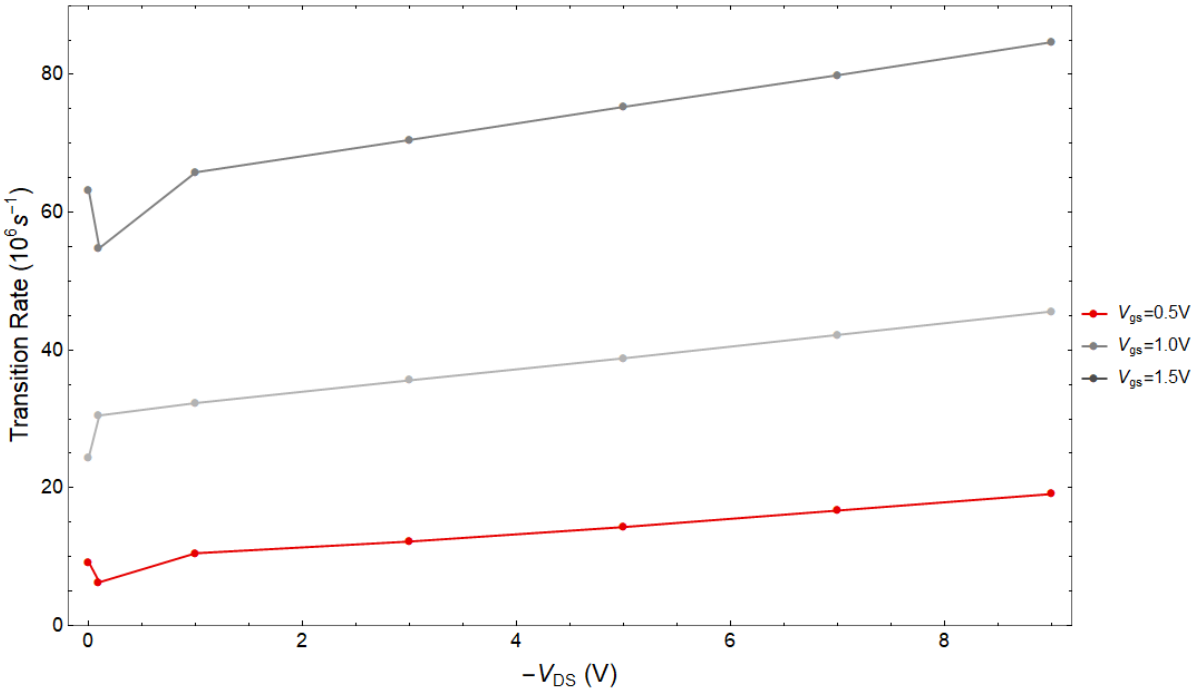

Fig. 3.3 Modulation of the transition rate by varying drain-source voltage. Increasing drain-source voltage is shown to have a positive correlation with the transition rate calculated via Fermi's golden rule.

From Fig. 3.3, it is shown that increasing the drain-source voltage amplitude has a positive correlation with an increasing transition rate. The amplitude of the bias applied at the gate is also shown to modulate transition rates. Modulation of the transition rate may allow for expanded control over the generation of single photons. The high transition rates for correspondingly low driving frequencies, combined with the capability to modulate transition rates presents the diamond field effect transistor as a promising device for quantum information applications.

There exists further interest to electrically control the generation of single photons using nitrogen-vacancy color centers within the structure. This can be achieved through the charge capture processes that govern the transitions of NV^- color centers to NV^0 color centers before their emission of single photons and transition back to the NV^- ground state. The charge capture process provides a means of electrically triggering single photon emission [137]. In this process, an NV^- color center absorbs a hole and becomes an NV^0 color center in the excited state. The NV^0 color center relaxes into the ground state by emitting a photon before eventually absorbing an electron, putting the color center back into the NV^- configuration. The governing equation for the photon emission rate due to the charge capture process is given by:

$$R_{ph} = \Phi \frac{1}{\frac{1}{c_n n} + \frac{1}{c_p p} + \tau}, \tag{3.6}$$

where Φ is the quantum efficiency, c_n and c_p are the electron and hole capture rate constants, n and p are the electron and hole densities in diamond, and τ is the excited state lifetime of NV^0 color centers. For electrons the capture cross-section of NVs in the neutral state is equal the lattice constant of diamond, which is estimated to be 10^{-15} cm^2 [138]–[140]. This corresponds to an electron capture rate constant of $c_n \approx 1.7 \times 10^{-8}$ cm^{3}s^{-1}. Based on previous work incorporating the cascade capture model [141], c_p is evaluated as $c_p = \frac{4\pi r_T^3}{3\tau_E} = 3.9 \times 10^{-7}$ cm^{3}s^{-1}, where r_T is the critical radius in the Thomson model[142] and τ_E is the relaxation time of the hole energy due to interaction with acoustic phonons[143]. For our calculations, $\tau = 29.41$ ns, which is based on previous experiments involving the excited state lifetimes of NV^0 color centers[144], and $\Phi = 30\%$.

In our simulations, we consider a new design consisting of diamond FET with an NV located at the diamond/TMO interface at the center of the gate region. This FET incorporates an n-doped hydrogen-terminated diamond layer with all other parameters remaining the same. The gate length L_g is 24 nm, the TMO layer still consists of hydrogenated molybdenum trioxide. N-doped diamond is selected due to previous works featuring its fabrication[145], as well as its ability to be hydrogen terminated [146]. The doping concentration of phosphorous in the diamond layer is 8.85×10^{15} cm^{-3}, which is in line with previous experiments[146]. The new structure is shown in Fig. 3.4. Under different bias conditions, there exists different electron and hole densities, which facilitates the cycling of the charge capture process.

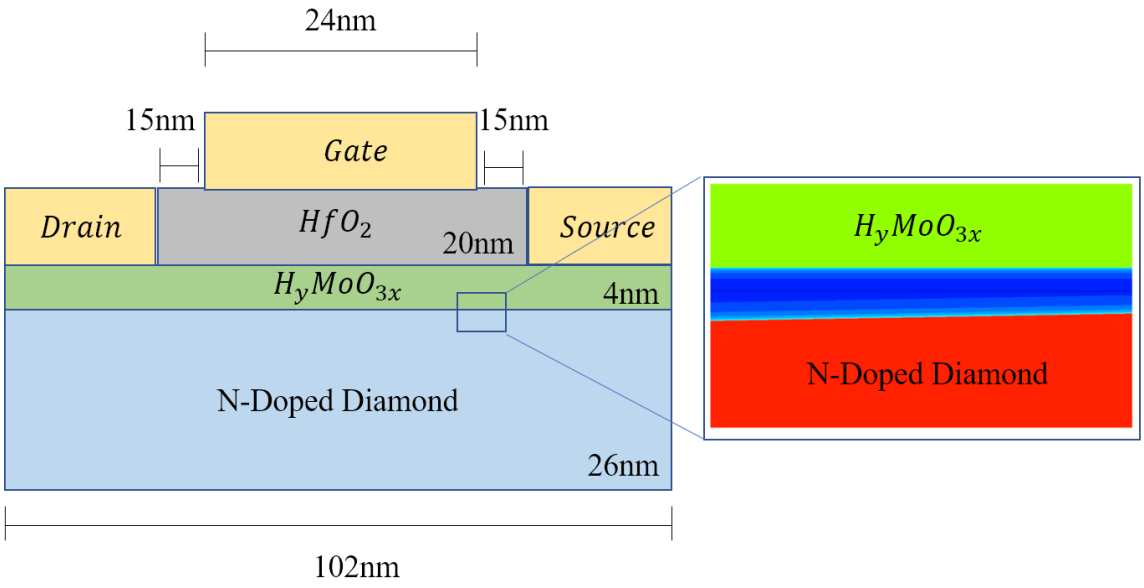

Fig. 3.4 New design of diamond FET incorporating n-doped diamond to facilitate the charge capture process. The dopant used is phosphorous with a concentration of $8.85 \times 10^{15}\ cm^{-3}$

Under negative bias of -5V applied at the gate, there is an abundance of holes at the diamond/TMO interface with $p = 1.58 \times 10^{15}\ \text{cm}^{-3}$. Under positive bias of +5V applied at the gate, there is an abundance of electrons at the diamond TMO interface with $n = 2.91 \times 10^{14}\ \text{cm}^{-3}$. Thus, the photon emission rate from the charge capture process at the diamond/TMO is $R_{ph} = 3.98 \times 10^{6}\ \text{s}^{-1}$. The results are tabulated in Fig. 3.5.

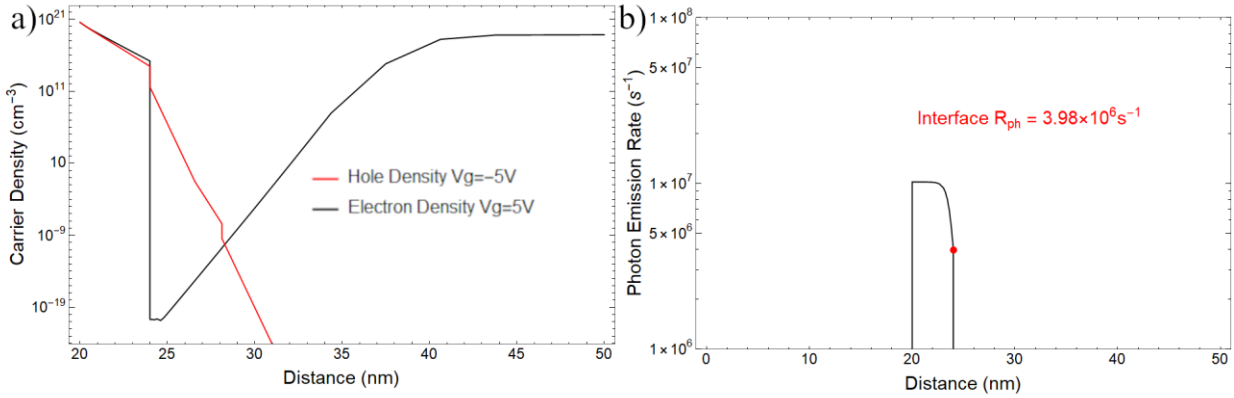

Fig. 3.5 (a) Carrier concentrations as a function of position taken vertically through the center line of the device. (b) Photon emission rates at 30% quantum efficiency as a function of position. The photon emission rate in the vicinity of the diamond/TMO interface is $\text{R}_{\text{ph}} = 3.98 \times 10^{6}\text{s}^{-1}$

The basic operation of the device involves the application of a square wave with amplitude $\pm 5V$ applied at the gate contact, which is similar to previous works involving the electrical triggering of NVs using diamond FETs[147]. Due to the high photon emission rate, the charge capture process would theoretically be limited by the frequency of the applied voltage and is a topic for further study.

3.5 Summary

In this work we have presented a diamond field effect transistor with a gate length scaled from 24 um to 24 nm. We have explored the transport characteristics of the device through simulations and have applied an approach utilizing Fermi's golden rule to ascertain the capabilities of the device as a platform for single photon emission. Simulated transport characteristics are in good agreement with the literature, and we have confirmed through simulations the existence of a short channel effect concerning the saturation voltage of diamond field effect transistors with varying gate lengths. Calculations involving Fermi's golden rule found transition rates of particles within the two-dimensional hole gas to exceed $\Gamma = 2.436 \times 10^{7}\ \mathrm{s}^{-1}$, at a driving frequency of $\omega_0 = 3.533 \times 10^{13}\ \mathrm{s}^{-1}$, which can be further modulated by varying applied voltages across the device. A new device was evaluated to determine the photon emission rates of NVs situated at the n-doped diamond/TMO interface. This evaluation found the photon emission rate at the interface to be $R_{ph} = 3.98 \times 10^{6}\ \mathrm{s}^{-1}$. These results position the diamond field effect transistor as a promising technology for single photon emission and thus, quantum information applications.

Through this work, we have quantified the ability for diamond field effect transistors to be utilized towards the on-demand emission of single photons from NV centers. One fundamental feature of this emission is that the repetition rate is still controlled by the excited state lifetime of the NV^0 centers. The use of plasmonic structures and their resulting modification of the photonic density of states, as well as their high Purcell enhancement factors may enable us to obtain even faster repetition rates. In the next chapter, we will explore this possibility in further detail.

4. INVESTIGATION OF PLASMONIC CAVITIES FOR THE ENHANCEMENT OF NITROGEN VACANCY COLOR CENTER EMISSION

4.1 Introduction

Enhancement of the emission of single photon sources [148], such as the nitrogen vacancy (NV) color center in diamond is of great interest in the field of quantum information processing [149], quantum chemistry [150], and biology [151]. The greatest limiting factors for the detected photon rate from nitrogen vacancies color centers are radiative lifetime and photon collection efficiency. An approach for brightness enhancement centers on greatly increasing the local density of states (LDOS) in the vicinity of the color center, leading to faster photon emission [152]. Dielectric [153]–[155] and plasmonic [156] resonators, among other methods, are typically used for LDOS enhancement.

Plasmonic resonant cavities are of great interest as their physical sizes can be below the diffraction limit of light [157]–[166]. This capability is in stark contrast to those of conventional dielectric cavities such as photonic crystals [167]–[169], microdisks [170]–[172], nanowires [173]–[175] and metal cladding cavities [176]–[179], which are limited by wavelength. This property allows for smaller mode volumes in plasmonic resonant cavities than that of typical dielectric cavities. The LDOS is proportional to the ratio of the resonance quality factor and the localized volume of the fields. Therefore, plasmonic cavities offer an attractive option for the enhancement of the LDOS due to their broadband (low quality factor) LDOS enhancement and their theoretical potential for lifetime shortening has been estimated to be two magnitudes higher than other methods [180], [181]. A design limitation of plasmonic resonant cavities is the high loss resulting from non-radiative quenching of excitation and plasmon absorption in metals.

In this work we explore a plasmonic cavity design of varying physical parameters and its enhancement of the LDOS with applications for enhancement of emissions from nitrogen vacancy color centers. To this end, we have employed FDTD methods using the MIT. Electromagnetic Equation Propagation (MEEP) simulator, which is an open source FDTD simulation tool that has been used in previous work concerning plasmonic devices [182]. Device parameters, such as the resonant wavelengths, quality factors, mode volumes and Purcell enhancement factors are extracted from simulation results.

4.2 Numerical Model

MEEP performs simulations by solving Maxwell's equations in two and three dimensions while exploiting device symmetry. The device under consideration is shown in Fig. 4.1. The device features a silver (Ag) cladding formed around a silicon (Si) plasmonic cavity of length *L* with a 50 nm × 50 nm cross section. This silicon cavity is enclosed on either side by two waveguides, one of which acts as a plasmonic mirror with the same cross section. The other waveguide serves to direct emission for the extraction of electromagnetic waves. This waveguide is comprised of a 5 nm silica (SiO_2) layer, with a 45 nm crystalline silicon (c-Si) layer on top. The width of this waveguide is also adjustable. The plasmonic mirror waveguide is comprised of an outer cladding composed of SiO_2 and a square inner core composed of c-Si with a cross section of 20 nm × 20 nm. The center of the simulation volume incorporates a diamond sphere with 18 nm diameter representing a nanodiamond. This sphere is situated halfway between the c-Si and Ag cladding. The included MEEP material libraries supply the material parameters for the device. The electron behavior within the metal is implemented utilizing the Drude-Lorentz model and is thus a physically accurate description of the dielectric function for Ag.

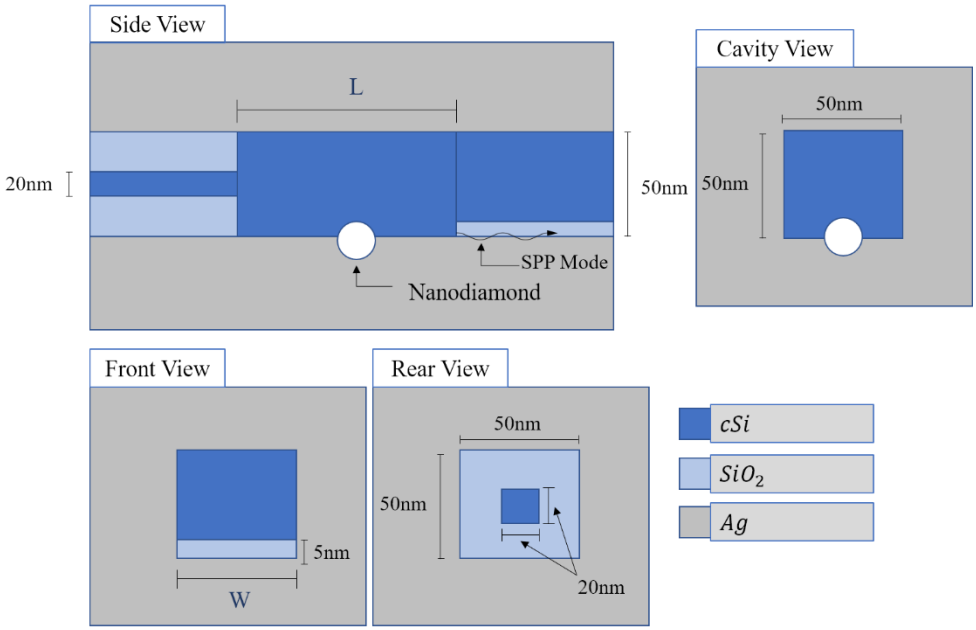

Fig. 4.1 Schematic diagram of the plasmonic cavity. L represents the length of the center cavity region. W represents the width of the transmission waveguide. Parameters in black are fixed. Parameters in blue are variable. The center cavity region has a cross section of 50nmx50nm. Situated halfway between the c-Si and Ag of the center cavity region is the nanodiamond. Simulations were performed by varying the central cavity length L as well as the width W of the transmission waveguide.

FDTD simulations are performed, varying the length of the center plasmonic cavity L from 30 nm to 130 nm in increments of 10 nm. Two-dimensional FDTD simulations using an iterative method are performed using MEEP and the included Harminv package to extract the resonant wavelengths and their associated quality factors. These simulations are performed using a dipole gaussian source situated within the diamond sphere which represents emission from NVs to identify potential resonant modes of the device at various resonator lengths. As resonant modes are identified, shorter dipole pulses centered at the frequency of the mode with the highest quality factor are applied in FDTD simulations until the desired accuracy is achieved. These simulations inform more robust, three-dimensional simulations. The mode volumes of the highest quality factor modes are simulated using a three-dimensional domain within MEEP. At each time step, the mode volume is calculated. In post-processing, the mode volume is estimated from the supplied data.

4.3 Results and Discussion

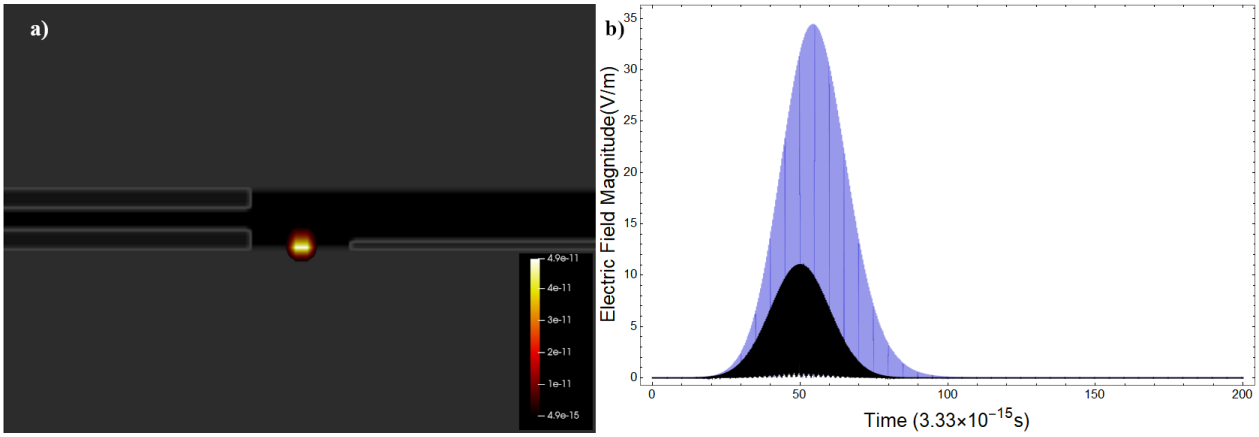

Fig. 4.2 (a) Electric field intensity ($\boldsymbol{E^2}$) mode profiles in the plasmonic cavity with L = 90nm. (b) Electric field amplitude vs time for the same cavity showing enhancement of the local fields within the vicinity of the nanodiamond.

Eleven devices, with central cavity lengths L ranging from 30 nm to 130 nm, are simulated, and the central cavity length is found to have negligible impact on the resonant wavelength of each device. Each device has a resonant wavelength of ~684nm, which is close to the peak of emission from the NV spectrum[183]. This is in good agreement to previous works utilizing a similar device structure[184]. The resonant wavelength identified arises from plasmonic effects occurring at the

diamond/Ag interface. As a result of these plasmonic effects, each device also displays formidable Purcell enhancement factors (~8.70×10^5) at room temperature owing to their incredibly small modal volumes (~4.8×10^{-8} μm^3). Previous simulations demonstrate a similar design reaching Purcell factors of around 36000 [185]. Other designs incorporating diamond nanorods reach Purcell enhancement factors on the order of 10^4 [231]. The incorporation of the nanodiamond within the design allows for much smaller mode volumes, which are what allow for the increased Purcell factor.

These Purcell enhancement factors allow for the efficient enhancement of emission from NVs. From further studies, it is found that the central cavity length *L*, while not having impact on the resonant properties of the device, is able to modulate the transmission properties of the device.

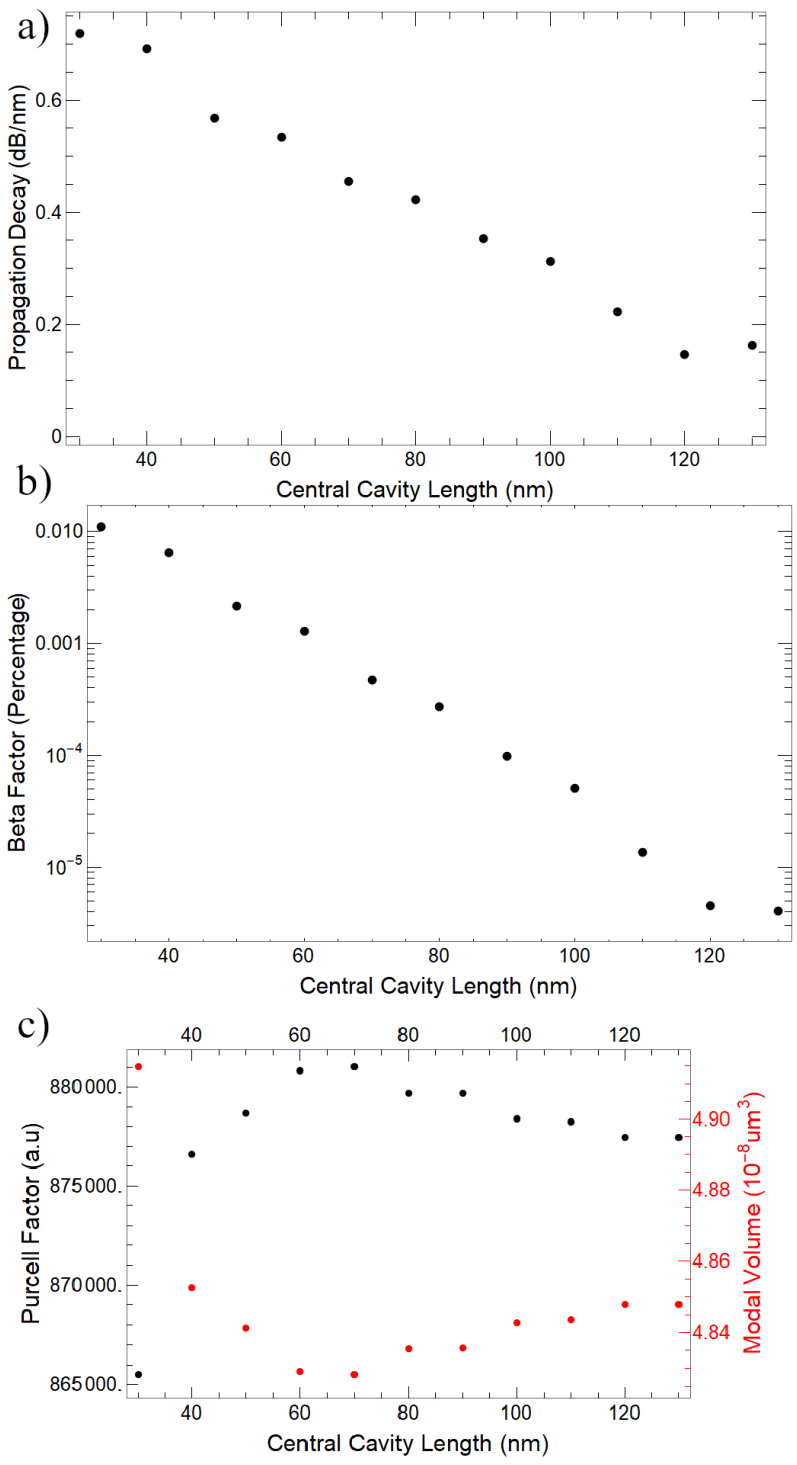

Fig. 4.3 Device characteristics modulated by the central cavity length L. a) Propagation decay vs. Cavity Length. By increasing the central cavity length, it is possible to modulate the decay of plasmonic modes leaving the cavity and traveling down the transmission waveguide. b) Beta Factor vs. Cavity Length. The amount of energy coupled out from the central cavity can also be modulated by the central cavity length. This creates a design tradeoff. c) Purcell Factor and Modal Volume vs. Cavity Length. The Purcell Enhancement Factor and modal volumes are shown. Each cavity has a robust Purcell Enhancement Factor owing to plasmonic effects at the diamond/Ag interface.

Device characteristics are summarized within Fig. 4.3. In tabulating the results, the propagation decay is plotted vs central cavity length in Fig. 4.3(a). Contrast this with the spontaneous emission coupling factor (β-factor) plot in Fig. 4.3(b). The β-factor is defined as [186]–[189]:

$$\beta = \frac{\text{Total Energy Radiated into Waveguide Mode}}{\text{Total Energy Radiated}} \tag{4.1}$$

From the results, a design tradeoff is introduced. Increasing the length of the central cavity lowers the amount of energy coupled out into the transmission waveguide, but also decreases the propagation decay of plasmon modes. This allows these devices to be custom tailored to a variety of applications. Figure 4.3(c) displays the calculated mode volumes and Purcell Enhancement factors at the resonant mode for each device. The mode volumes for each device were calculated with the following equation[190]:

$$V = \frac{\int \varepsilon E^2 dV}{\max(\varepsilon E^2)} \tag{4.2}$$

The integration of the fields throughout the entire simulation domain for each time step as well as the squared maximum electric field is readily available at each time step using supplied MEEP functionality. The Purcell enhancement factor was calculated for each device according to the equation[191]

$$F_p = \frac{3}{4\pi^2}\left(\frac{\lambda}{n}\right)^3\left(\frac{Q}{V}\right), \tag{4.3}$$

where λ is the free-space resonant wavelength, Q is its associated quality factor, V is the calculated modal volume, and n is the refractive at the dipole position, which is taken to be 2.417 for diamond.

4.3.1 Modulation of Device Characteristics via Transmission Waveguide Width

Of further interest is the modulation of device characteristics by varying the transmission waveguide width. Simulations were performed on a device with central cavity length L of 30 nm by varying the transmission waveguide width W from 50 nm to 100 nm in increments of 10 nm allowing for a robust study of relevant parameters. Results are tabulated in Figs. 4.4 and 4.5.

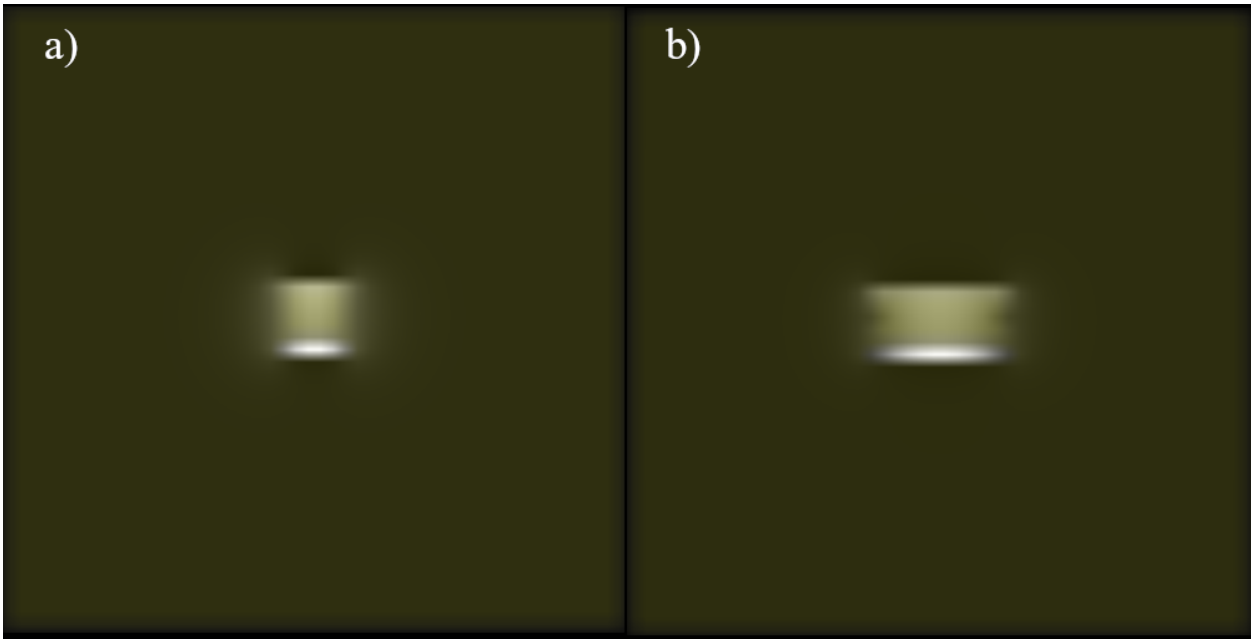

Fig. 4.4 Field profiles for devices with transmission waveguide widths, W of (a) 50 nm and (b) 100 nm. Both examples feature strongly localized fields in the 5 nm tall SiO_2 region.

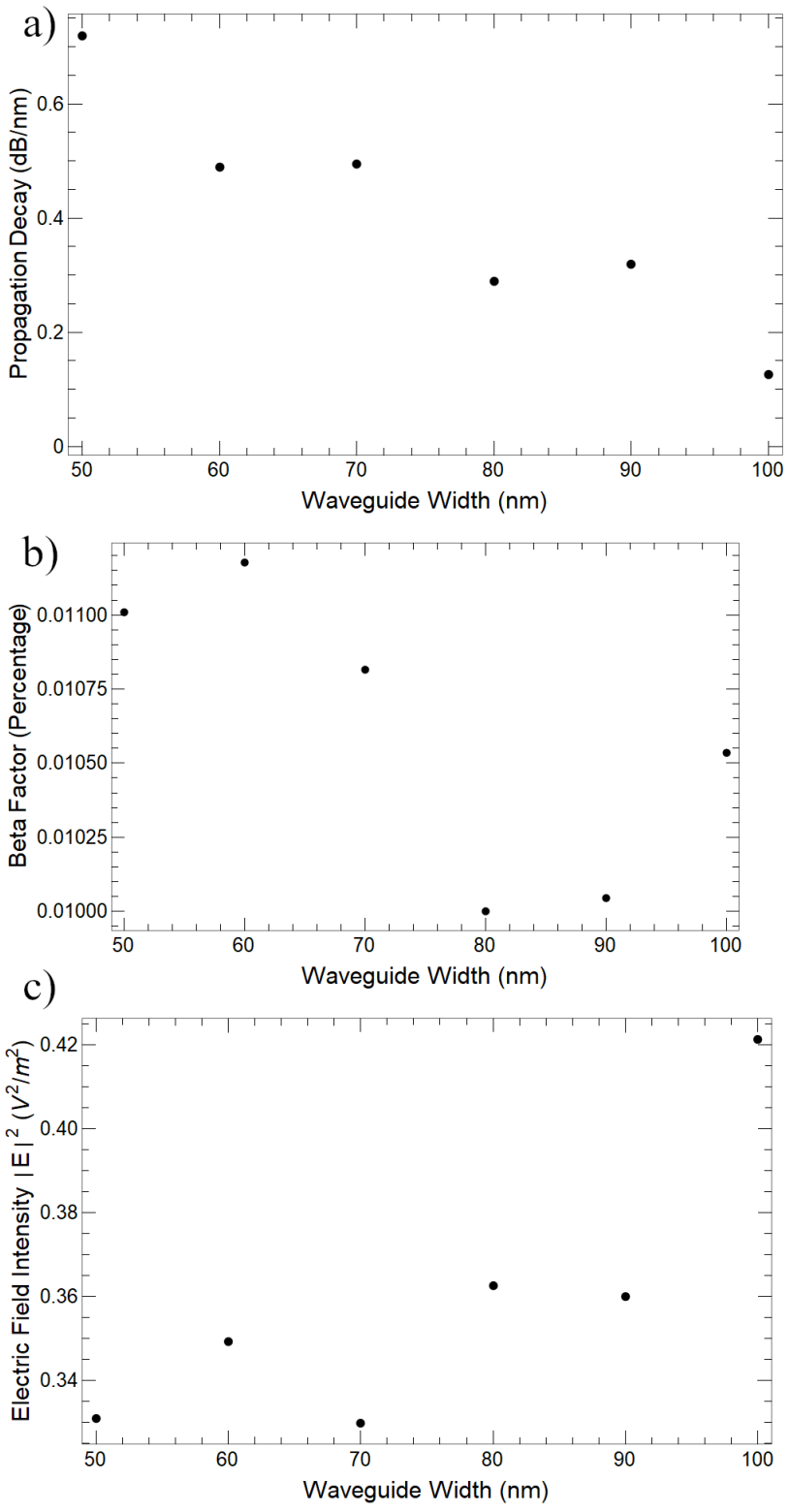

Fig. 4.5 Device parameters vs. transmission waveguide width. Propagation decay decreases with increased waveguide width a). β-factor remains largely constant with waveguide width b), however the electric field intensity measured at the end of the waveguide shows a general increase with the width of the transmission waveguide c).

Here, we see that the increasing of the transmission waveguide width W has an effect on device performance. The propagation decay decreases as the transmission waveguide width is increased. This is in addition to the intensity of the electric field measured at the end of the waveguide growing. All of this occurs while the β-factors remain largely constant. By varying the central cavity length and transmission waveguide width, devices tailored to several applications become possible.

Fabrication of this device is possible through AFM pick and place of nanodiamonds onto Ag films followed by a robust fabrication process. Ag is deposited, followed by Ag photolithography to ensure the nanodiamond is half-coated in Ag. Following this, Silica is deposited and patterned using masking techniques involving E-beam lithography. Fox resist is a good candidate for this process. Once the Silica has been patterned, Silicon is deposited and patterned using the same technique, followed by a final Ag deposition which will cover the entire device [192]. The process flow is shown in Fig. 4.6.

Fig. 4.6 Process flow for device fabrication. The device is fabricated using a combination of deposition of different materials in tandem with photolithographic techniques utilizing fox resist.

This device features a very complex fabrication process. AFM pick and place is used at the beginning to ensure the device can be fabricated in a controlled manner. The photolithographic techniques utilized require several depositions of resist and several liftoffs, which further complicate the fabrication process. Due to the complicated fabrication process, there could be several fabrication problems. Tapered sidewalls in the design could impact the field patterns as well as coupling parameters and propagation decay. Our analysis features several devices of varying physical dimensions, so in the case of tapered sidewalls, the performance of the device can be estimated from our prior simulations. Incomplete photoresist removal could also impact the performance of the device. Photoresist incorporated into the device could also change the coupling parameters by introducing regions of varying refractive index. Misalignment could also occur with the fabrication of the device, which necessitates a very precise fabrication environment. To successfully realize this device, an E-beam lithographic environment with a masking resolution of 20 nm is required. Fortunately, E-beam lithography allows for a resolution of sub 10 nm.

4.4 Summary

In this work we have investigated several plasmonic devices for the application of enhancement of emission from nitrogen vacancy color centers. Each device displays prodigious Purcell enhancement factors allowing for the robust enhancement of NV emission while also allowing for the tuning of transmission capabilities for robust photon extraction with many applications.

The enhancement of NV emission via plasmonic devices is an attractive method to position the NV center for quantum information applications. Combining this plasmonic enhancement with electrical generation of single photons within a symmetric, easily fabricated platform may open the door to a truly robust single photon source featuring fast repetition rates and on-demand single photon generation. It serves as the next logical step for this thesis, which will be explored further in the next chapter.

6. DESIGN OF AN ELECTRICALLY CONTROLLED DIAMOND-BASED PLASMONIC DEVICE FOR THE ELECTRICAL GENERATION AND ENHANCEMENT OF SINGLE PHOTON EMISSION FROM NITROGEN VACANCY COLOR CENTERS

6.1 Introduction

Nitrogen vacancy (NV) color centers are a promising platform for room temperature single photon sources[193]. The NV center is created by two adjacent defects in the diamond lattice: a substitutional nitrogen atom, and a vacancy (missing carbon atom). The NV center can exist in two charge states, NV^0 and NV^-. The NV^0 color center features broadband luminescence (~550-750 nm)[194], [195], with a zero-phonon line (ZPL) at 575 nm [196], [197]. NVs have a number of attractive optical properties, such as room temperature operation, little inhomogeneous broadening, and deterministic positioning through ion implantation. Another attractive feature for quantum applications is that the electric spin can be prepared, manipulated, and read out with optical and microwave excitations[198]. To realize room-temperature single photon generation, it is important to enhance the NV center photon production rate as well as increase the collection efficiency of emitted photons. Diamond, having a refractive index ($n = 2.43$)is a great candidate material for photonic structures. Several structures have been investigated to achieve enhancement of single photons, such as photonic crystal slabs in polycrystalline diamond on insulator films [199], microdisk resonators[200], [201], positioning nanodiamond crystals on wide bandgap materials and metallic nanostructures [202]–[204], single-mode waveguides[205], and diamond nanorods[206]–[208]. Plasmonic devices also serve as an attractive option for enhancement of single photon emission from NVs due to their small mode volumes[209], [210], which lead to large Purcell enhancement factors. Several plasmonic structures have also been investigated. Examples include diamond-silver apertures[211], plasmonic cavities[212], [213], nanodiamonds on silver substrates[214], and plasmonic nanoantennas [215]. Another exciting feature of NV color centers is the ability to electrically manipulate their charge states through the charge capture process for the electrical generation of single photons at room temperature [216]–[218]. A device combining the electrical generation of single photons with the enhancement of those photons via coupling to plasmonic modes could serve as a robust single photon emitter for quantum information applications. In this work, we describe a diamond-based device combining electrical

generation using hydrogen-terminated phosphorous-doped diamond and optical enhancement via coupling to diamond-silver plasmonic modes.

6.2 Numerical Model

Electrical simulations to determine carrier concentrations are carried out using Sentaurus TCAD by Synopsys. Optical simulations are performed using the MIT Electromagnetic Equation Propagation (MEEP) simulator. Sentaurus TCAD by Synopsys is a commercial semiconductor device simulation program that can solve the Poisson equation coupled to electron and hole continuity equations for a given structure using a mesh. In specifying device parameters, the program can account for semiconductor quantities, such as doping dependent mobilities, Fermi-statistics for carrier concentrations, band to band tunneling, the conduction and valence band density of states for electrons and holes, effective masses of electrons and holes, and generation and recombination phenomena. MEEP is an open-source finite difference time difference (FDTD) simulator that performs simulations by solving Maxwell's equations in two and three dimensions. MEEP simulation results are employed to extract device parameters, such as resonant wavelengths, quality factors, mode volumes, and Purcell enhancement factors. The device under consideration is shown in Fig. 5.1(a). The device features a cylindrical, 20 nm tall, n-type hydrogen-terminated diamond region with a 20 nm diameter. On top of this cylindrical region is a 4 nm tall p-type cylindrical crystalline silicon region of the same diameter. Both the n-type hydrogen-terminated diamond and crystalline silicon regions are topped by a cylindrical HfO_2 layer of 6 nm thickness. This region also extends cylindrically around both the diamond and silicon layers with a 2.5 nm thickness. The entire device is embedded within a silver substrate. square A silver contact with dimensions of 10 nm x 10 nm x 10 nm is located on the diamond region. Device parameters for diamond are obtained from various sources[219]–[223] and are tabulated in Table 1. All relevant parameters for HfO_2 and c-Si are included in supplied Sentaurus and MEEP material libraries. For Sentaurus simulations, the doping profiles are required. The n-type diamond region is simulated using a phosphorous doping concentration of 9×10^{16} cm^{-3}, which is typical of phosphorous doped diamond samples[224], [225]. The hydrogen terminated diamond surface is represented using a constant linear doping profile with concentration 1.5×10^{21} cm^{-3}. The p-type crystalline silicon region is doped with boron at a concentration of 2×10^{19} cm^{-3}. Figure 5.1(b) depicts the band structure under zero bias conditions of the device with the oxide layer on the left.

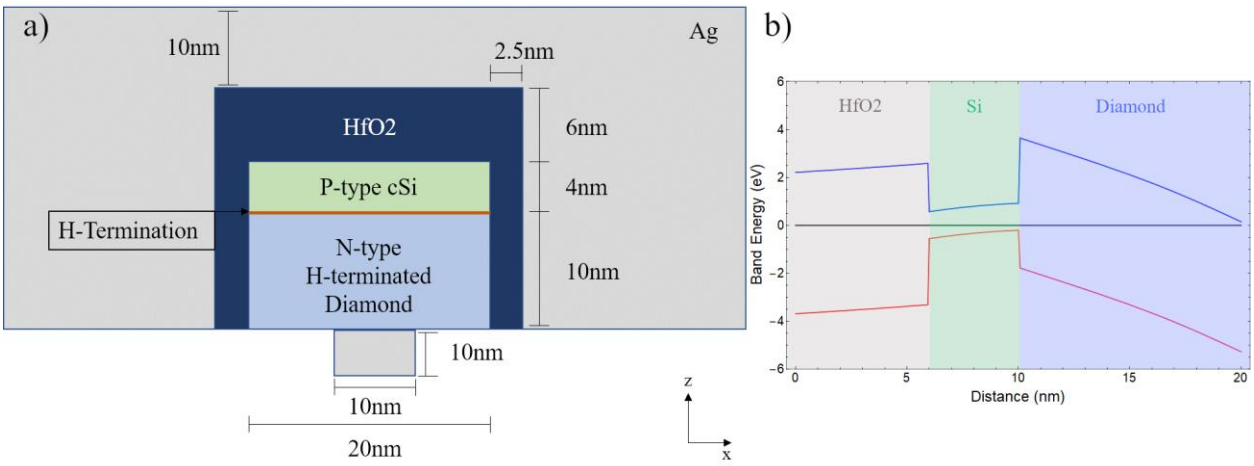

Fig. 6.1 (a) schematic cross section of cylindrical device showing relevant dimensions. (b) Band structure of device taken vertically from center of the HfO2 region.

Table 6.1 Diamond device parameters.

Diamond Parameter	**Value**	**Reference**
epsilon	5.7	[223]
Bandgap (eV)	5.47	[226]
Electron Affinity (eV)	1.3	[222]
Maximum Electric Field (MV/m)	20	[216]
Electron Mobility ($cm^2/V \cdot s$)	20.2	[230]
Hole Mobility ($cm^2/(V \cdot s)$)	20.2	[222]
Thermal Conductivity ($W/(cm \cdot K)$)	20	[226]
Hole Saturation Velocity <100> ($10^7 cm/s$)	1.1	[219]
Electron Saturation Velocity <100> ($10^7 cm/s$)	1.5	[219]
Hole Density of States (cm^{-3})	1.80E+19	[219]
Electron Density of states (cm^{-3})	6.41E+19	[219]

6.3 Device Simulation

Device simulations involving Sentaurus are carried out by applying a bias (V_g) to the silver cladding region while grounding the square silver contact. This is represented within Sentaurus by contacts with a work function of 4.26 eV [227]. Fermi statistics are employed in the simulation with a high-field saturation mobility model. Schottky-Reed Hall recombination is activated as well. Line search damping and relative error control are utilized to ensure convergence of the simulation. Carrier concentrations throughout the device are obtained by ramping the silver cladding contact

in increments of 1 mV to the desired value of $\pm$ 5 V and extracting the data from the supplied Sentaurus Visual software.

Device simulations involving MEEP are performed in three dimensions using the FDTD iterative method. A dipole gaussian source, representing emission from nitrogen vacancy color centers, is placed at the diamond-silicon interface. At each time step, the field magnitudes and mode volumes are tabulated. This data is used along with the supplied Harminv software package to determine resonant wavelengths of the device. Directional power plots of parallel and perpendicular dipole orientations are performed using two dimensional FDTD simulations with collection efficiencies calculated using MATLAB.

6.4 Results and Discussion

The charge capture process governs the transitions of NV^- color centers to NV^0 color centers before their emission of single photons and subsequent transition back to the NV^- ground state[213]. The governing equation for the photon emission rate due to this process is given by

$$R_{ph} = \Phi \frac{1}{\frac{1}{c_n n} + \frac{1}{c_p p} + \tau} \tag{5.1}$$

Where Φ is the quantum efficiency (30%), c_n and c_p are the electron and hole capture rate constants (1.7×10^{-8} cm^{3}s^{-1} and 3.9×10^7 cm^{3}s^{-1} respectively), n and p are the electron and hole densities in diamond, and τ is the excited state lifetime of NV^0 color centers (29.41 ns [228]).

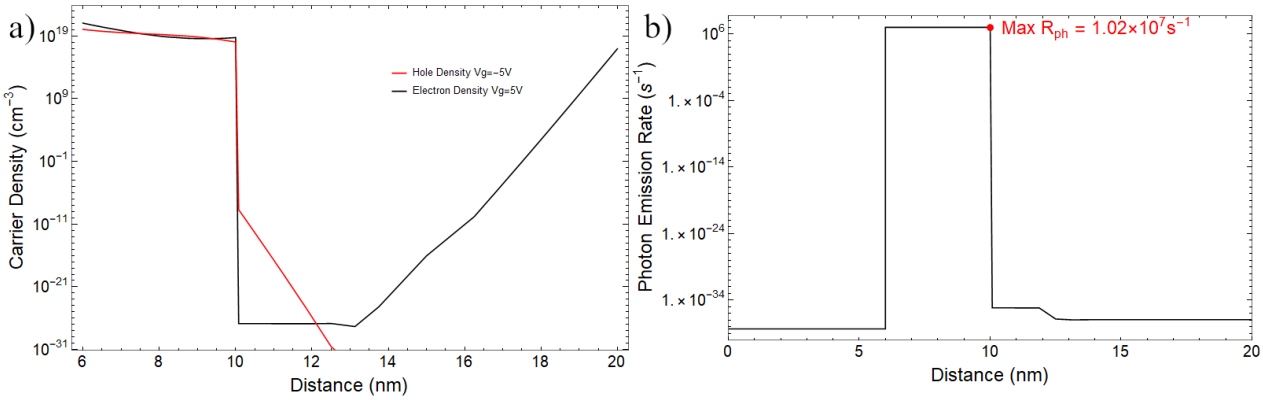

Fig. 6.2 (a) Carrier concentrations vs distance. Concentrations are along the center line of the device with the silicon/diamond interface featuring large carrier counts ~10^{19} cm^{-3}. (b) Photon emission rate vs distance determined by the charge capture equation with a quantum efficiency of 30%.

Under negative bias of $V_g = \pm 5$ V applied to the silver cladding region, there is an abundance of electrons and holes at the silicon/diamond interface with $n, p = \sim 10^{19}$ cm^{-3}. This corresponds to a photon emission rate $R_{ph} = 1.02 \times 10^7$ s^{-1}. These results are tabulated in Fig. 5.2. For best generation of single photons, and NV should ideally be placed at the diamond/silicon interface.

Because the charge capture process facilitates the emission of single photons from the NV^0 excited state, the device should enhance emission from NV^0 color centers for best results. This device also serves as a plasmonic cavity, which can enhance emission. The device shows some enhancement of radiation at the NV^0 zero-phonon line (ZPL) at 575 nm, but maximum enhancement is achieved with dipole sources of both parallel and perpendicular orientation at 593 nm. Fortunately, this wavelength is still within the NV^0 sidebands[196].

Attempts were made to match the frequency of the NV^0 zero phonon line with the plasmonic cavity resonance frequency. Conventional wisdom would dictate that increasing or shrinking the radius of the cavity, or other dimensions would also shift the resonance of the cavity. What was found through simulations is that the resonance of the cavity is not significantly affected by the cavity dimensions, beyond a certain point. When the radius of the diamond, or HfO_2 sidewall within the cavity is increased from the original value, the resonant frequency is not shifted further. Instead, the resonant frequency remains the same and the enhancement of emission is dominated by losses occurring due to the metal. The resonant frequency of the cavity is also nearly unchanged if the radius is decreased with minimal enhancement occurring. This peculiar behavior is due to the fact that the resonant behavior of the cavity is plasmonic in nature. The resonance occurs due to the creation of surface plasmons at the diamond and HfO_2 spacer/silver interface. Moving the NV center away from this interface by increasing the cavity radius will only suppress the creation of surface plasmons because of the reduced local density of states. Lowering this radius will assist somewhat in the creation of surface plasmons but will not provide as feasible of a design because of the smaller feature sizes required.

From our simulations, the only way that was found to substantially modulate the resonant frequency of the cavity was to change the material capping the diamond nano-rod. Silicon was selected because it provided a resonant wavelength close to that of NV^0 emission that was well within the NV^0 sidebands. Other materials were evaluated including transition metal oxides (TMOs), such as MoO_{3x} and H_yMoO_{3x}. However, those materials did not allow for charge capture

via electrical stimulation, or the resonant wavelength was shorter than the NV^0 zero phonon line. The key takeaway from these simulation studies is that while having a small cavity is helpful, the performance is not overly sensitive to dimensions within a certain range. Instead, it is best to focus on the material qualities and to ensure that the modeled material properties are an accurate reflection of what can be experimentally fabricated – this includes both the bulk material dispersion, as well as the surface roughness, or smoothness of the interfaces.

Tabulated within Fig. 5.3 is time series data showing the enhancement of emission from dipole placed at the silicon/diamond interface, along with the frequency response measured using MEEP's flux plane feature.

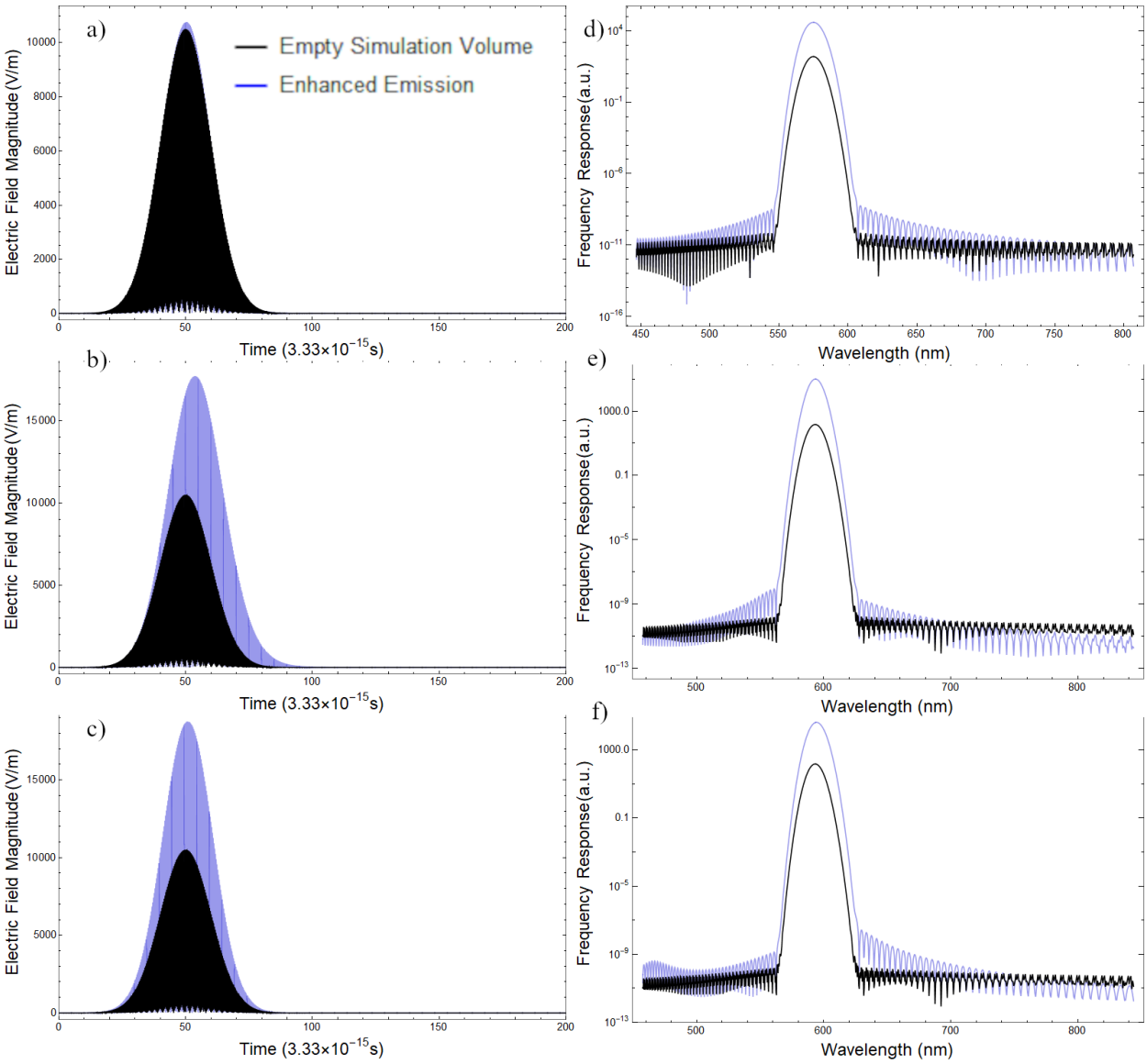

Fig. 6.3 Time series data showing enhancement of dipole emission (blue) compared to an empty simulation volume (black) at (a) the ZPL (575nm) of parallel polarized NV^0 color centers, (b) parallel polarized dipoles at 593nm, and (c) perpendicular polarized dipoles at 593nm. (d)-(f) Associated frequency spectrum with enhanced dipole emission in blue compared with an empty simulation volume in black.

To calculate the Purcell enhancement factor, the mode volume for the device was calculated within MEEP and uses the following equation [175]:

$$V = \frac{\int \varepsilon E^2 dV}{\max(\varepsilon E^2)} \tag{5.2}$$

The integration of the fields throughout the simulation volume and the maximum electric field is calculated at each time step within MEEP. The Purcell enhancement factor was calculated according to the following equation [230]:

$$F_p = \frac{3}{4\pi^2}\left(\frac{\lambda}{n}\right)^3\left(\frac{Q}{V}\right), \tag{5.3}$$

where λ is the free-space resonant wavelength, Q is its associated quality factor, V is the calculated modal volume, and n is the refractive at the dipole position, which is taken to be 2.417 for diamond. The Purcell enhancement factor is calculated to be 6.54×10^5 at a wavelength of 593 nm for the device This Purcell enhancement factor is an order of magnitude higher than previous works also involving diamond nanorods (~10^4) [231].

To estimate the Purcell enhancement factor at 575 nm, the maximum of the squared electric field for emission at 593 nm and 575 nm (Max(E^2)) was extracted and fit with a Lorentzian profile. The Lorentzian curve had the following equation:

$$L(x) = \frac{\mathrm{Max}(E^2)_{593nm}}{(x - 593nm)^2 + \left(\frac{1}{2}\Gamma\right)^2} \times \left(\frac{1}{2}\Gamma\right)^2, \tag{5.4}$$

where Γ corresponds to the width of the Lorentzian curve. This profile differs from normal Lorentzian profiles where $\int_{-\infty}^{\infty} L(x)dx = 1$ and is used as an approximation to the resonance shape at 593 nm. This profile was then used to estimate the quality factor of the off-resonant NV^0 ZPL at 575 nm, which was calculated to be 9.24. This was done by modulating Γ until the Lorentzian profile at $L(575\ \mathrm{nm})$ matched the $\max(E^2)$ electric field at 575 nm. Once a suitable value for Γ was found, the same profile was used with the quality factor at 593 nm Q_{593nm} replacing the squared electric field value. The Purcell enhancement factor calculated from this quality factor was $F_{p575nm} = 2.42 \times 10^5$. Thus, the device still boasts prodigious enhancement at the NV^0 zero phonon line.

Of further interest is the collection efficiency of single photons emitted by the device. Photon collection efficiencies are extracted from the far-field profile of the power emitted in the direction of the square contact (negative z direction). This is shown in Fig. 5.4. An objective lens with a numerical aperture NA 0.95 positioned at the square contact can collect light emitted into

the solid angle of 72°. In the case of parallel polarization, 61.4% of the emitted light can be collected, while only 16.4% of the emitted light can be collected for perpendicular polarization. This is due to reflection by the square contact. Better collection efficiencies can be achieved by modulating the size and shape of the square contact.

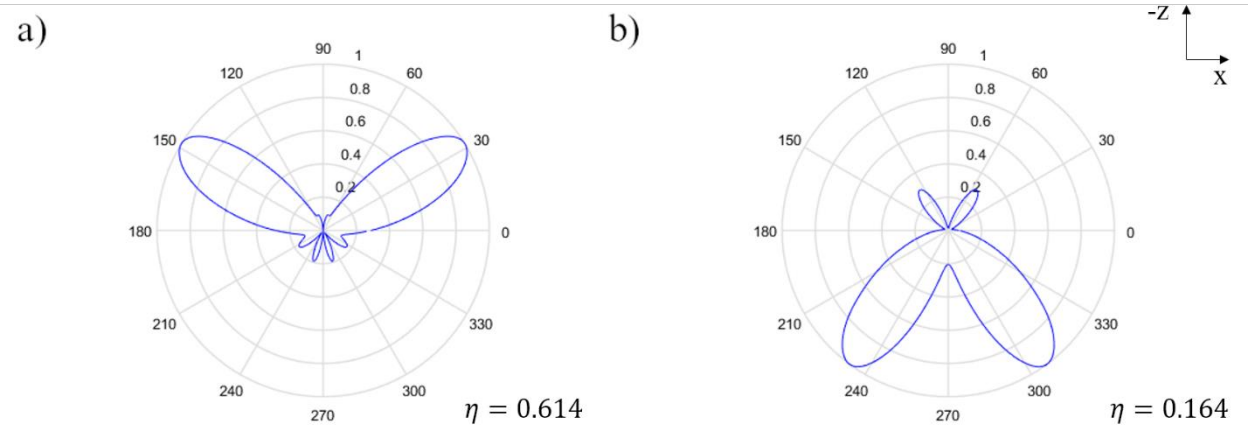

Fig. 6.4 Far-field profile of power emitted from an (a) parallel polarized and (b) perpendicular polarized dipole at the diamond/silicon interface. Calculated collection efficiencies η are also indicated.

Fabrication of this device is possible through a relatively simple series of process steps. A hydrogen terminated diamond substrate containing NVs is coated with a p-type silicon layer of 4nm thickness. Following this, fox resist is deposited, and e-beam lithography is carried out to produce a cylindrical region in the fox resist of 20 nm diameter. The silicon is etched using the fox resist as a mask. Following the silicon etch, the diamond is etched with inductively coupled plasma (ICP) reactive ion etching (RIE). For diamond, the ICP RIE process would most likely use some composition of additives added to an O_2 plasma. HfO_2 is deposited following this step, followed by Ag deposition via evaporation. The substrate is flipped and another round of ICP is conducted on the substrate side of the diamond. Finally, silver is deposited via evaporation and patterned using photolithographic techniques, such as silver photo-etch. This process flow is similar to previous works involving diamond nano posts [192]. In this work, diamond nano posts with diameters from 20nm-80nm were created. Due to the ability for E-beam lithographic features to obtain a sub 10nm resolution, a 20nm diameter for diamond nano posts is easily achievable.

As a result of the above analysis, some of the key fabrication challenges are to control the surface roughness and material quality in several deposition and etch steps. For example, the inductively coupled plasma reactive ion etch (ICP RIE) is known to have detrimental effects on surface roughness and surface material purity. This is due to the co-deposition and sputtering that typically occurs during the process that can lead to long, fibrous formations known as "grass" [237]. Several efforts have been made to improve the surface roughness of diamond during the ICP RIE process, such as the addition of argon, which may improve surface roughness by 20%-40% [238]. There have been recent advances in the surface smoothness of diamond during the ICP RIE process achieving ultra-smooth surfaces with RMS surface roughness of <0.5 nm [239]. These results can be achieved through 10% addition of CHF_3 in O_2 plasma at a radio frequency power of 400 W for single-crystal diamond, as reported in this previous work [239]. Finally, scaife polishing has been shown to yield surface roughness averaging less than 1 nm [240]. Using these one or more of these methods during the fabrication should yield a diamond surface that is sufficiently smooth for the next steps of the fabrication.

The deposition of silicon onto the diamond substrate will typically involve low-pressure chemical vapor deposition. This deposition method can yield films with RMS surface roughness of 1.15 ± 0.04 nm for amorphous silicon films and 3.06 ± 0.08 nm for poly-silicon films [241]. For a thin silicon layer, another approach could involve silicon deposition, followed by etching to the desired thickness of 4 nm prior to the deposition of fox resist.

Hafnium oxide (HfO_2) is typically deposited through atomic layer deposition. This process typically yields incredibly smooth surfaces with previous work reporting RMS surface roughness as low as 0.15 nm [242]. As the atomic layer deposition would occur after the removal of fox resist, it is of key importance to ensure all resist is properly removed prior to deposition. Following this approach, ALD process will conformally coat the silicon and diamond layers, resulting in a smooth surface for the deposition of silver to proceed.

Silver can be deposited via sputtering with some experiments reporting an RMS surface roughness of 4 nm[243] when deposited onto glass. This surface roughness can be controlled via modulation of the deposition rate with consistent results being obtained via low deposition rates (up to 0.1 ML/s). At these low deposition rates, the surface roughness is not dependent on layer thickness and is instead equal to the substrate surface roughness. Since we are depositing HfO_2 via ALD, and that surface will be incredibly smooth, it is reasonable to assume that the deposited

silver will also display a smooth surface as well in best case scenario, with the average case scenario of the silver surface having RMS surface roughness equal to ~4 nm as reported in previous works. While polishing or other methods may yield even lower surface roughness, based on work with other materials, additional experiments would be needed to confirm.

In summary, since surface quality and material purity are the key determinants of the alignment between theory and experiment, it is crucial to select approaches yielding favorable values of both variables. While several approaches have been outlined above based directly on recent experimental literature, the recommended approach still needs to be validated in experiment. Finally, it should not be taken to preclude a different fabrication route if a different set of fabrication tools are more readily available and can yield comparable or better results.

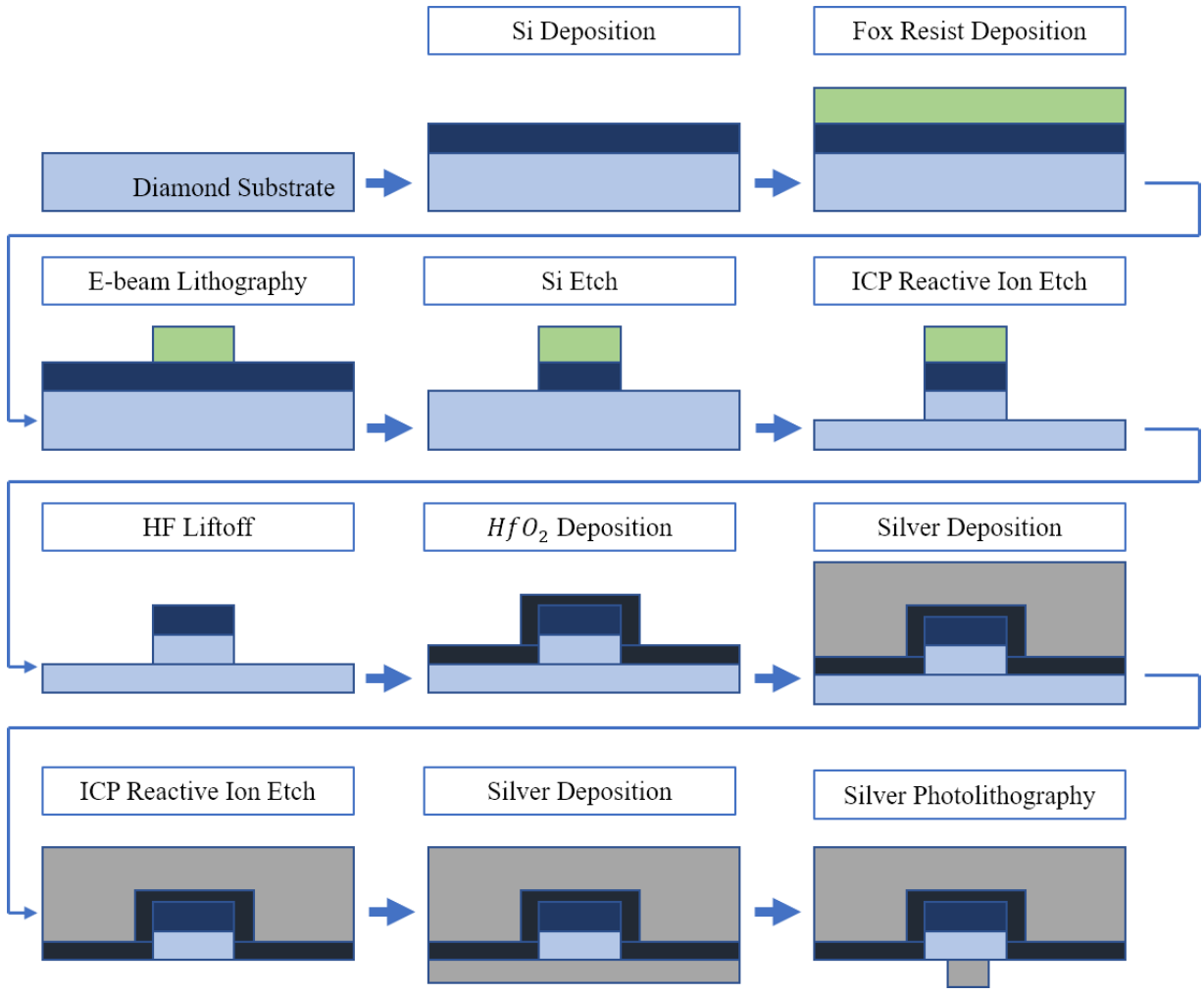

Fig. 6.5 Process flow for device fabrication. This device follows a simple fabrication process using e-beam lithography, silicon etching, and reactive ion etching to shape the silicon and diamond layers. HfO2 and silver are deposited before another round of reactive ion etching followed by silver deposition and patterning to create the contact.

6.5 Summary

We have demonstrated a device capable of electro generation and enhancement of single photon emission. This device achieves a photon emission rate of $R_{ph} = 1.02 \times 10^7\ \mathrm{s}^{-1}$ at the silicon/diamond interface. The emission is further enhanced by the device itself, which serves as a plasmonic cavity. The cavity shows some enhancement at the NV^0 ZPL with best enhancement at 593 nm, which is within the NV^0 sidebands. The Purcell enhancement factor was calculated to be $F_p = 6.54 \times 10^5$ at 593 nm. Collection efficiency of the device is highest with parallel dipole orientation at 61.4%, and lowest at perpendicular dipole orientation at 16.4%. Due to the high single photon generation rates and high Purcell enhancement factor of this device, it is well situated for quantum information applications. While these results conclude the new results of the thesis, we will next summarize our findings and suggest potential future work in this area.

7. CONCLUSIONS AND FUTURE WORK

In this thesis, we studied several methods to enhance the emission from nitrogen vacancy color centers. Experimental demonstrations, numerical models, and analytical studies were performed to identify and optimize the design of high-performance room-temperature quantum devices. To achieve a reduction in the excited state lifetime of NV centers, an experimental study was conducted and characterized using a custom confocal microscopy setup. Numerically, several designs of room temperature single photon sources were investigated with promising results aimed towards electroluminescence from nitrogen vacancy color centers as well as the enhancement of that luminescence via plasmonic cavities and waveguides. These contributions are summarized below.

- Chapter 2 demonstrated the experimental measurement of the reduced excited state lifetime of nitrogen vacancy color centers after doping with Xenon impurities. Dimond thin films were grown using a custom experimental procedure involving the salt-assisted ultrasonicated disaggregation of nanodiamond particles, followed by electrophoretic deposition onto a highly oriented pyrolytic graphite substrate. A custom confocal microscopy setup was utilized that enabled the measurement of the excited state lifetimes of several color centers. The measured excited state lifetime after doping was 297 ± 10 ps. A model utilizing coupled-mode theory was created to account for the reduced excited state lifetime, as well as the peculiar spectrum measured via the custom confocal microscopy setup

- Chapter 3 investigated the performance of a highly scaled diamond field effect transistor incorporating transition metal oxides, and its applications towards the electroluminescence from nitrogen vacancy color centers. The transport characteristics of the device were obtained and also compared to previous experimental work. The device's suitability as a single photon emitter was evaluated using two different methods. In the first method, a study involving solutions of the Schrodinger equation in the vicinity of the Diamond/TMO interface was employed along with calculations involving Fermi's Golden Rule. In the second method, a new device with an n-type, hydrogen terminated diamond region was

investigated. Charge capture rate equations were utilized to determine the photon emission rate at 30% quantum efficiency. The calculated photon emission rate was found to be $R_{ph} = 3.98 \times 10^6\ \mathrm{s}^{-1}$. This positions the diamond field effect transistor as a possible device for the electrical generation of single photons at room temperature.

- Chapter 4 analyzed several plasmonic structures for their enhancement of single photon emission from nitrogen vacancy color centers, as well the modulation of their propagation, coupling, and other device parameters, via the tuning of the device dimensions. Each device displays prodigious Purcell enhancement factor $F_P \sim 8.70 \times 10^5$ owning to their small mode volumes $V \sim 4.8 \times 10^{-8}\ \mathrm{um}^3$. By modulating the central cavity length L, as well as the width of the transmission waveguide W, the coupling from the central cavity along with the propagation decay can be finely adjusted, positioning this device as a good candidate for integration into several nanophotonic devices.

- Chapter 5 presented a room-temperature single photon emitter capable of electroluminescence from nitrogen vacancy color centers via charge capture processes, as well as enhancement of that luminescence via plasmonic interactions. The device featured a large Purcell enhancement factor $F_p = 6.54 \times 10^5$, as well as a photon emission rate of $R_{ph} = 1.02 \times 10^7\ \mathrm{s}^{-1}$. The device showed some enhancement at the NV^0 ZPL with best enhancement shown at 593 nm. The collection efficiency of radiation emitted from the device was largest with parallel dipole orientation equaling 61.4%. The electrical generation of single photons, along with their enhancement natively within the device itself presents an elegant solution for the creation of a robust single photon source operating at room temperatures.

To summarize, this thesis studied both the experimental procedures and numerical simulations of the enhancement of emission from nitrogen vacancy color centers for quantum information applications. In particular, the combined works explore photonic designs for enhanced performance (Purcell enhancement and electrical generation of single photons) via numerical simulations. They also experimentally demonstrate viable doping strategies for the reduction of the excited state lifetimes of NV centers. While these works address challenges in single photon

generation at room temperatures, future works are needed to fully realize the potential of these ideas. Summarized below are two possible future follow-up studies:

- There are very few publications exploring the implantation of Xenon into nanometer and bulk sized diamond samples. Since implantation with Xenon has been shown to reduce the excited state lifetimes of nitrogen vacancy color centers within nanodiamond, more work in this area is warranted to discover the full potential for lifetime reduction and also other quantum information applications. For example, spin preparation and readout of NV centers is commonly performed on NVs with a negative charge state [232]–[234]. The question arises of how nanodiamond samples implanted with xenon would affect the preparation and readout of NV spin states. The coupling of those spin states to single photons could also be explored. Along with these experiments, more research into the energy level structure of Xenon vacancy color centers, and their interaction with nitrogen vacancy color centers could also be conducted. Charge capture processes for silicon vacancy color centers are largely understood [235], but there has not been similar work done with the Xenon vacancy. Another topic of interest would be the modulation of the charge capture process via interaction with Xenon vacancy color centers.

- In chapters 2 through 5, several designs were numerically investigated to determine their potential for the electrical generation of single photons, their enhancement of single photon emission via plasmonic effects, or both. The next logical step after obtaining these designs would be their fabrication and experimental testing. The fabrication of these devices remains as a final test to determine their viability for quantum information applications. The designs of each device utilize readily available materials that have been extensively studied, such as diamond and silicon. Transition metal oxides, however, and their integration in diamond-based devices, remains an exciting area for further research. MoO_3 and H_yMoO_{3x}, and their ability to allow hydrogen terminated surfaces to survive the FET fabrication process [236], may enable new quantum technologies incorporating n-type hydrogen terminated diamond and these TMOs for electrical generation of single photons along with their enhancement.

APPENDIX A. FILM FORMATION AND ION IMPLANTATION

We conduct the nanodiamond film assembly process in two stages: film deposition and ion implantation. In the first stage, we create a very dense film to increase the chances of successful ion implantation. To achieve this goal, nanodiamonds in colloidal suspension in deionized (DI) water were purchased from Microdiamant at 0.4 wt%. We disaggregate these aqueous nanodiamonds using a process known as Salt-Assisted Ultrasonic disaggregation (SAUD) [86], [87], which is followed by film formation using an electrophoretic deposition.

To conduct the SAUD process, 62.5 ml of nanodiamond solution is heated to evaporate the water until a volume of 10 ml is achieved. 10 g of sodium chloride (Sigma Aldrich) is added, and the solution is sonicated at 60 kHz in a sonic bath for 100 minutes. The solution is dispersed between two 50 ml centrifuge tubes with DI water added to achieve a volume in both tubes of 50 ml. The sample is then washed via centrifugation at 4000 rpm for 10 minutes, after which the supernatant containing the sodium chloride is removed. After adding more DI water, a size selection via centrifugation is performed. The sample is centrifuged at 12000 rpm for 30 minutes, and the resulting colloidal suspension is divided into 20 ml samples by size into scintillation vials.

After obtaining suitably disaggregated nanodiamonds, two 20 ml scintillation vials of SAUD nanodiamonds are used for electrophoretic deposition onto highly-oriented pyrolytic graphite (HOPG) substrates[88]–[92]. For each HOPG substrate (Spi Technologies), a 100 ml beaker is affixed with two copper electrodes. 20 ml of SAUD nanodiamonds is poured into the beaker, and each HOPG substrate is placed onto the cathode electrode. A voltage of 0.3 V is applied to the electrodes to initiate electrophoretic deposition. After an hour, the voltage is switched off, and each HOPG substrate is retrieved. This process gives rise to a nanodiamond film on the surface of each substrate. Characterization of the film are conducted with the Hitachi S-4800 scanning electron microscope and reveal good surface coverage, and the films are satisfactory for ion implantation.

In the second stage, ion implantation of xenon is performed at Sandia National Laboratories. The implantation is conducted at 45 keV with fluences of 10^{12} ions/cm^2 and 10^{14} ions/cm^2 for each substrate, respectively. An anneal at 500℃ is performed in vacuum. Upon return from Sandia National Laboratories, the diamond films were characterized optically, using a visible light microscope and an air objective with a numerical aperture of 0.9.

APPENDIX B. OPTICAL CHARACTERIZATION OF XE-IMPLANTED NANODIAMONDS

All optical characterization was performed using a custom-made scanning confocal microscope with a 50 μm pinhole, based on a commercial inverted microscope body (Nikon Ti−U). Objective scanning was performed using a P-561 piezo stage driven by an E-712 controller (Physik Instrumente). The optical pumping in the CW experiments was administered by a 200 mW continuous wave 532 nm laser (Shanghai Laser Century). Lifetime characterization was performed using a 514 nm fiber-coupled diode laser with a nominal 100 ps pulse width and adjustable repetition rate in the 2−80 MHz range (BDL-514-SMNi, Becker & Hickl). The excitation beams in all the optical experiments were reflected off a 550 nm long-pass dichroic mirror (DMLP550L, Thorlabs), followed by a 550 nm long-pass filter (FEL0550, Thorlabs) that filter out the remaining pump power. Two avalanche detectors with a 30 ps time resolution and 35% quantum efficiency at 650 nm (PDM, Micro-Photon Devices) were used for single-photon detection during scanning and lifetime measurements. Time-correlated photon counting was performed by an acquisition card with a 4 ps internal jitter (SPC-150, Becker & Hickl).

REFERENCES

[1] Gazzano, O., Almeida, M. P., Nowak, A. K., Portalupi, S. L., Lemaître, A., Sagnes, I., White, A. G., & Senellart, P. (2013). Entangling quantum-logic gate operated with an ultrabright semiconductor single-photon source [Article]. *Physical Review Letters*, *110*(25), 250501–250501. https://doi.org/10.1103/PhysRevLett.110.250501

[2] Reimer, M. E., Bulgarini, G., Akopian, N., Hocevar, M., Bouwes Bavinck, M., Verheijen, M. A., Bakkers, E. P. A. M., Kouwenhoven, L. P., & Zwiller, V. (2012). Bright single-photon sources in bottom-up tailored nanowires [Article]. *Nature Communications*, *3*(1), 737-1/6. https://doi.org/10.1038/ncomms1746

[3] Alléaume, R., Treussart, F., Messin, G., Dumeige, Y., Roch, J.-F., Beveratos, A., Brouri-Tualle, R., Poizat, J.-P., & Grangier, P. (2004). Experimental open-air quantum key distribution with a single-photon source [Document]. In *New journal of physics* (Vol. 6). IOP Publishing. https://doi.org/10.1088/1367-2630/6/1/092

[4] Kiraz, A., Atatüre, M., & Imamoğlu, A. (2004). Quantum-dot single-photon sources: Prospects for applications in linear optics quantum-information processing [Article]. *Physical Review. A, Atomic, Molecular, and Optical Physics*, *69*(3), 1–32305. https://doi.org/10.1103/PhysRevA.69.032305

[5] Bouwmeester, D., Strauf, S., Rakher, M. T., Stoltz, N. G., Coldren, L. A., & Petroff, P. M. (2007). High-frequency single-photon source with polarization control [Article]. *Nature Photonics*, *1*(12), 704–708. https://doi.org/10.1038/nphoton.2007.227

[6] Yuan, Z., Kardynal, B. E., Stevenson, R. M., Shields, A. J., Lobo, C. J., Cooper, K., Beattie, N. S., Pepper, M., & Pepper, M. (2002). Electrically Driven Single-Photon Source [Article]. *Science (American Association for the Advancement of Science)*, *295*(5552), 102–105. https://doi.org/10.1126/science.1066790

[7] Migdall, A. L., Branning, D., & Castelletto, S. (2002). Tailoring single-photon and multiphoton probabilities of a single-photon on-demand source [Article]. *Physical Review. A, Atomic, Molecular, and Optical Physics*, *66*(5), 053805/4. https://doi.org/10.1103/PhysRevA.66.053805

[8] Khan, M., Hemmer, P. R., Babinec, T. M., Zhang, Y., Hausmann, B. J. M., Maze, J. R., & Lon ar, M. (2010). A diamond nanowire single-photon source [Article]. *Nature Nanotechnology*, *5*(3), 195–199. https://doi.org/10.1038/nnano.2010.6

[9] Huber, D., Reindl, M., Huo, Y., Huang, H., Wildmann, J. S., Schmidt, O. G., Rastelli, A., & Trotta, R. (2017). Highly indistinguishable and strongly entangled photons from symmetric GaAs quantum dots [Article]. *Nature Communications*, *8*(1), 15506–15506. https://doi.org/10.1038/ncomms15506

[10] Grangier, P., Sanders, B., & Vuckovic, J. (2004). Focus on Single Photons on Demand [Article]. *New Journal of Physics*, *6*. https://doi.org/10.1088/1367-2630/6/1/E04

[11] Riedel, D., Söllner, I., Shields, B. J., Starosielec, S., Appel, P., Neu, E., Maletinsky, P., & Warburton, R. J. (2017). Deterministic Enhancement of Coherent Photon Generation from a Nitrogen-Vacancy Center in Ultrapure Diamond [Article]. *Physical Review. X*, *7*(3), 031040. https://doi.org/10.1103/PhysRevX.7.031040

[12] Radulaski, M., Zhang, J. L., Tzeng, Y., Lagoudakis, K. G., Ishiwata, H., Dory, C., Fischer, K. A., Kelaita, Y. A., Sun, S., Maurer, P. C., Alassaad, K., Ferro, G., Shen, Z., Melosh, N. A., Chu, S., & Vučković, J. (2019). Nanodiamond Integration with Photonic Devices [Article]. *Laser & Photonics Reviews*, *13*(8), 1800316-n/a. https://doi.org/10.1002/lpor.201800316

[13] Gür, F. N., McPolin, C. P. T., Raza, S., Mayer, M., Roth, D. J., Steiner, A. M., Löffler, M., Fery, A., Brongersma, M. L., Zayats, A. v, König, T. A. F., & Schmidt, T. L. (2018). DNA-Assembled Plasmonic Waveguides for Nanoscale Light Propagation to a Fluorescent Nanodiamond [Article]. *Nano Letters*, *18*(11), 7323–7329. https://doi.org/10.1021/acs.nanolett.8b03524

[14] Siampour, H., Kumar, S., Davydov, V. A., Kulikova, L. F., Agafonov, V. N., & Bozhevolnyi, S. I. (2018). On-chip excitation of single germanium vacancies in nanodiamonds embedded in plasmonic waveguides [Article]. *Light, Science & Applications*, *7*(1), 61–69. https://doi.org/10.1038/s41377-018-0062-5

[15] Zhao, J., Cheng, Y., Shen, H., Hui, Y. Y., Wen, T., Chang, H.-C., Gong, Q., & Lu, G. (2018). Light Emission from Plasmonic Nanostructures Enhanced with Fluorescent Nanodiamonds [Article]. *Scientific Reports*, *8*(1), 3605–3608. https://doi.org/10.1038/s41598-018-22019-z

[16] Khan, M. B., & Khan, Z. H. (2017). Nanodiamonds: Synthesis and Applications [Bookitem]. In *Nanomaterials and Their Applications* (pp. 1–26). Springer Singapore. https://doi.org/10.1007/978-981-10-6214-8_1

[17] Volk, F., Johnson, J. D., Greiner, N. R., & Phillips, D. S. (1988). Diamonds in detonation soot [Article]. *Nature (London)*, *333*(6172), 440–442. https://doi.org/10.1038/333440a0

[18] Yang, G.-W., Wang, J.-B., & Liu, Q.-X. (1998). Preparation of nano-crystalline diamonds using pulsed laser induced reactive quenching [Article]. *Journal of Physics. Condensed Matter*, *10*(35), 7923–7927. https://doi.org/10.1088/0953-8984/10/35/024

[19] Boudou, J.-P., Curmi, P. A., Jelezko, F., Wrachtrup, J., Aubert, P., Sennour, M., Balasubramanian, G., Reuter, R., Thorel, A., & Gaffet, E. (2009). High yield fabrication of fluorescent nanodiamonds [Article]. *Nanotechnology*, *20*(23), 235602–235602. https://doi.org/10.1088/0957-4484/20/23/235602

[20] Frenklach, M., Howard, W., Huang, D., Yuan, J., Spear, K. E., & Koba, R. (1991). Induced nucleation of diamond powder [Article]. *Applied Physics Letters*, *59*(5), 546–548. https://doi.org/10.1063/1.105434

[21] Decarli, P. S., & Jamieson, J. C. (1961). Formation of Diamond by Explosive Shock [Article]. *Science (American Association for the Advancement of Science)*, *133*(3467), 1821–1822. https://doi.org/10.1126/science.133.3467.1821

[22] Viecelli, J. A., & Ree, F. H. (2000). Carbon particle phase transformation kinetics in detonation waves [Article]. *Journal of Applied Physics*, *88*(2), 683–690. https://doi.org/10.1063/1.373721

[23] Tatsii, V. F., Bochko, A. v, & Oleinik, G. S. (2009). Structure and properties of Dalan detonation diamonds [Article]. *Combustion, Explosion, and Shock Waves*, *45*(1), 95–103. https://doi.org/10.1007/s10573-009-0013-9

[24] Boudou, J.-P., Curmi, P. A., Jelezko, F., Wrachtrup, J., Aubert, P., Sennour, M., Balasubramanian, G., Reuter, R., Thorel, A., & Gaffet, E. (2009). High yield fabrication of fluorescent nanodiamonds (Nanotechnology (2009) 20 (235602)) [Article]. *Nanotechnology*, *20*(35). https://doi.org/10.1088/0957-4484/20/35/359801

[25] Juang, Z. Y., Lai, J. F., Weng, C. H., Lee, J. H., Lai, H. J., Lai, T. S., & Tsai, C. H. (2004). On the kinetics of carbon nanotube growth by thermal CVD method. *Diamond and Related Materials*, *13*(11–12), 2140–2146. https://doi.org/10.1016/J.DIAMOND.2004.03.007

[26. Wang, X., You, H., Liu, F., Li, M., Wan, L., Li, S., Li, Q., Xu, Y., Tian, R., Yu, Z., Xiang, D., & Cheng, J. (2009). Large-Scale Synthesis of Few-Layered Graphene using CVD [Article]. *Chemical Vapor Deposition*, *15*(1–3), 53–56. https://doi.org/10.1002/cvde.200806737

[27] Butler, J. E., & Sumant, A. v. (2008). The CVD of Nanodiamond Materials [Article]. *Chemical Vapor Deposition*, *14*(7–8), 145–160. https://doi.org/10.1002/cvde.200700037

[28] Ohsawa, Y., Tamou, Y., Kikuchi, N., Hiraga, K., & Oku, T. (1991). TEM observations of diamond films produced by hot filament thermal CVD [Article]. *Journal of Materials Science*, *26*(14), 3748–3752. https://doi.org/10.1007/BF01184965

[29] Kamo, M., Sato, Y., Matsumoto, S., & Setaka, N. (1983). Diamond synthesis from gas phase in microwave plasma. *Journal of Crystal Growth*, *62*(3), 642–644. https://doi.org/10.1016/0022-0248(83)90411-6

[30] Matsumoto, S. (1985). Chemical vapour deposition of diamond in RF glow discharge [Article]. *Journal of Materials Science Letters*, *4*(5), 600–602. https://doi.org/10.1007/BF00720043

[31] Frenklach, M., Howard, W., Huang, D., Yuan, J., Spear, K. E., & Koba, R. (1991). Induced nucleation of diamond powder [Article]. *Applied Physics Letters*, *59*(5), 546–548. https://doi.org/10.1063/1.105434

[32] Frenklach, M., Kematick, R., Huang, D., Howard, W., Spear, K. E., Phelps, A. W., & Koba, R. (1989). Homogeneous nucleation of diamond powder in the gas phase [Article]. *Journal of Applied Physics*, *66*(1), 395–399. https://doi.org/10.1063/1.343890

[33] Chen, X., & Zhang, W. (2017). Diamond nanostructures for drug delivery, bioimaging, and biosensing [Article]. *Chemical Society Reviews*, *46*(3), 734–776. https://doi.org/10.1039/c6cs00109b

[34] Gomes, M. da M., Quinhones, M. S., Engelhardt, E., Lerner, R. M., Andrés, A., Pereira, P. M. C. de M., Miguens, S., Nacional, S., Ministério da Educação e Ciência, Berger, J., Dubowy, C., Sehgal, A., Rosbash, M., Benzer, S., Picco, S., Villegas, L., Tonelli, F., Merlo, M., Rigau, J., … Doğan, Z. (2013). Diamond nanowire synthesis, properties and applications. *Intech*, *15*(1), 13. https://www.intechopen.com/books/advanced-biometric-technologies/liveness-detection-in-biometrics%0Ahttps://doi.org/10.32725/jab.2004.016

[35] Dräbenstedt, A., & Jelezko, F. (1999). Low-temperature microscopy and spectroscopy on single defect centers in diamond [Article]. *Physical Review B - Condensed Matter and Materials Physics*, *60*(16), 11503–11508. https://doi.org/10.1103/PhysRevB.60.11503

[36] Brouri, R., Beveratos, A., Poizat, J.-P., & Grangier, P. (n.d.). Photon antibunching in the fluorescence of individual color centers in diamond [Article]. *ArXiv.Org*, *25*(17), 1294–126. https://doi.org/10.1364/OL.25.001294

[37] Kurtsiefer, C., Mayer, S., Zarda, P., & Weinfurter, H. (2000). Stable solid-state source of single photons [Article]. *Physical Review Letters*, *85*(2), 290–293. https://doi.org/10.1103/PhysRevLett.85.290

[38] Jelezko, F., Gaebel, T., Popa, I., Domhan, M., Gruber, A., & Wrachtrup, J. (2004). Observation of coherent oscillation of a single nuclear spin and realization of a two-qubit conditional quantum gate [Article]. *Physical Review Letters*, *93*(13), 1–130501. https://doi.org/10.1103/PhysRevLett.93.130501

[39] Prawer, S., Rabeau, J. R., Hemmer, P. R., Wittmann, C., Greentree, A. D., Twamley, J., Meijer, J., Domhan, M., Wrachtrup, J., Gaebel, T., Jelezko, F., Popa, I., Neumann, P., & Stavrias, N. (2006). Room-temperature coherent coupling of single spins in diamond [Article]. *Nature Physics*, *2*(6), 408–413. https://doi.org/10.1038/nphys318

[40] Doherty, M. W., Manson, N. B., Delaney, P., Jelezko, F., Wrachtrup, J., & Hollenberg, L. C. L. (2013). The nitrogen-vacancy colour centre in diamond [Article]. *Physics Reports*, *528*(1), 1–45. https://doi.org/10.1016/j.physrep.2013.02.001

[41] Davies, G., Nazare, M. H., & Hamer, M. F. (1976). The H3 (2.463 eV) Vibronic Band in Diamond: Uniaxial Stress Effects and the Breakdown of Mirror Symmetry [Article]. *Proceedings of the Royal Society of London. Series A, Mathematical and Physical Sciences*, *351*(1665), 245–265. https://doi.org/10.1098/rspa.1976.0140

[42] Vlasov, I. I., Ralchenko, V. G., Khomich, A. V., Nistor, S. V., Shoemaker, D., & Khmelnitskii, R. A. (2000). Relative Abundance of Single and Vacancy-Bonded Substitutional Nitrogen in CVD Diamond [Article]. *Physica Status Solidi. A, Applied Research*, *181*(1), 83–90. https://doi.org/10.1002/1521-396X(200009)181:1<83::AID-PSSA83>3.0.CO;2-6

[43] Steeds, J. W., & Kohn, S. (2014). Annealing of electron radiation damage in a wide range of Ib and IIa diamond samples. *Diamond and Related Materials*, *50*, 110–122. https://doi.org/10.1016/J.DIAMOND.2014.09.012

[44] Naydenov, B., Reinhard, F., Lämmle, A., Richter, V., Kalish, R., D'Haenens-Johansson, U. F. S., Newton, M., Jelezko, F., & Wrachtrup, J. (2010). Increasing the coherence time of single electron spins in diamond by high temperature annealing [Article]. *Applied Physics Letters*, *97*(24), 242511. https://doi.org/10.1063/1.3527975

[45] Mita, Y. (1996). Change of absorption spectra in type-Ib diamond with heavy neutron irradiation [Article]. *Physical Review. B, Condensed Matter*, *53*(17), 11360–11364. https://doi.org/10.1103/PhysRevB.53.11360

[46] Loubser, J. H. N., & Wyk, J. A. van. (1978). Electron spin resonance in the study of diamond [Article]. *Reports on Progress in Physics*, *41*(8), 1201–1248. https://doi.org/10.1088/0034-4885/41/8/002

[47] Davies, G. (1979). Dynamic Jahn-Teller distortions at trigonal optical centres in diamond [Article]. *Journal of Physics. C, Solid State Physics*, *12*(13), 2551–2566. https://doi.org/10.1088/0022-3719/12/13/019

[48] Fraczek, E., Savitski, V. G., Dale, M., Breeze, B. G., Diggle, P., Markham, M., Bennett, A., Dhillon, H., Newton, M. E., & Kemp, A. J. (2017). Laser spectroscopy of NV- and NV0 colour centres in synthetic diamond [Article]. *Optical Materials Express*, *7*(7), 2571–2585. https://doi.org/10.1364/OME.7.002571

[49] Doherty, M. W., Manson, N. B., Delaney, P., & Hollenberg, L. C. L. (2011). The negatively charged nitrogen-vacancy centre in diamond: the electronic solution [Article]. *New Journal of Physics*, *13*(2), 025019. https://doi.org/10.1088/1367-2630/13/2/025019

[50] Felton, S., Edmonds, A. M., Newton, M. E., Martineau, P. M., Fisher, D., & Twitchen, D. J. (2008). Electron paramagnetic resonance studies of the neutral nitrogen vacancy in diamond [Article]. *Physical Review. B*, *77*(8). https://doi.org/10.1103/PhysRevB.77.081201

[51] Fedyanin, D. Y., & Agio, M. (2016). Ultrabright single-photon source on diamond with electrical pumping at room and high temperatures. *New Journal of Physics*, *18*(7). https://doi.org/10.1088/1367-2630/18/7/073012

[52] Pan, L. S., & Kania, D. R. (1995). *Diamond: Electronic Properties and Applications* (L. S. Pan & D. R. Kania, Eds.; 1st ed. 1995.) [Book].

[53] Abakumov, V. N. (1991). *Nonradiative recombination in semiconductors* (V. I. (Vladimir I. Perel & I. N. Yassievich, Eds.) [Book]. North-Holland ; Sole distributors for the USA and Canada, Elsevier Science Pub. Co.

[54] Pezzagna, S., Rogalla, D., Wildanger, D., Meijer, J., & Zaitsev, A. (2011). Creation and nature of optical centres in diamond for single-photon emission—overview and critical remarks [Article]. *New Journal of Physics*, *13*(3), 035024. https://doi.org/10.1088/1367-2630/13/3/035024

[55] Choy, J. T., Bulu, I., Hausmann, B. J. M., Janitz, E., Huang, I.-C., & Lončar, M. (2013). Spontaneous emission and collection efficiency enhancement of single emitters in diamond via plasmonic cavities and gratings [Article]. *Applied Physics Letters*, *103*(16), 161101. https://doi.org/10.1063/1.4817397

[56] Trusheim, M. E., Sakakibara, R., Karamlou, A., & Englund, D. (2017). Embedded plasmonic nanoantennas for enhanced diamond NV-spin readout [Proceeding]. *2017 Conference on Lasers and Electro-Optics Europe & European Quantum Electronics Conference (CLEO/Europe-EQEC)*, 1–1. https://doi.org/10.1109/CLEOE-EQEC.2017.8087661

[57] Li, L., Chen, E. H., Zheng, J., Mouradian, S. L., Dolde, F., Schröder, T., Karaveli, S., Markham, M. L., Twitchen, D. J., & Englund, D. (2015). Efficient Photon Collection from a Nitrogen Vacancy Center in a Circular Bullseye Grating [Article]. *Nano Letters*, *15*(3), 1493–1497. https://doi.org/10.1021/nl503451j

[58] Kress, S. J. P., Antolinez, F. v, Richner, P., Jayanti, S. v, Kim, D. K., Prins, F., Riedinger, A., Fischer, M. P. C., Meyer, S., McPeak, K. M., Poulikakos, D., & Norris, D. J. (2015). Wedge Waveguides and Resonators for Quantum Plasmonics [Article]. *Nano Letters*, *15*(9), 6267–6275. https://doi.org/10.1021/acs.nanolett.5b03051

[59] Akselrod, G. M., Argyropoulos, C., Hoang, T. B., Ciracì, C., Fang, C., Huang, J., Smith, D. R., & Mikkelsen, M. H. (2014). Probing the mechanisms of large Purcell enhancement in plasmonic nanoantennas [Article]. *Nature Photonics*, *8*(11), 835–840. https://doi.org/10.1038/nphoton.2014.228

[60] Curto, A. G., Volpe, G., Taminiau, T. H., Kreuzer, M. P., Quidant, R., & van Hulst, N. F. (2010). Unidirectional Emission of a Quantum Dot Coupled to a Nanoantenna [Article]. *Science (American Association for the Advancement of Science)*, *329*(5994), 930–933. https://doi.org/10.1126/science.1191922

[61] Andersen, S. K. H., Kumar, S., & Bozhevolnyi, S. I. (2016). Coupling of nitrogen-vacancy centers in a nanodiamond to a silver nanocube [Article]. *Optical Materials Express*, *6*(11), 3394–3406. https://doi.org/10.1364/OME.6.003394

[62] Gerard, J.-M., & Gayral, B. (1999). Strong Purcell effect for InAs quantum boxes in three-dimensional solid-state microcavities [Article]. *Journal of Lightwave Technology*, *17*(11), 2089–2095. https://doi.org/10.1109/50.802999

[63] Maier, S. A. (2006). Effective Mode Volume of Nanoscale Plasmon Cavities [Article]. *Optical and Quantum Electronics*, *38*(1), 257–267. https://doi.org/10.1007/s11082-006-0024-7

[64] Spiller, T. P., Munro, W. J., Barrett, S. D., & Kok, P. (n.d.). An introduction to quantum information processing: applications and realizations [Article]. *Contemporary Physics*, *46*(6), 407–436. https://doi.org/10.1080/00107510500293261

[65] Aharonovich, I., Englund, D., & Toth, M. (2016). Solid-state single-photon emitters. *Nature Photonics*, *10*(10), 631–641. https://doi.org/10.1038/nphoton.2016.186

[66] Somaschi, N., Giesz, V., de Santis, L., Loredo, J., Almeida, M., Hornecker, G., Portalupi, S., Grange, T., Anton, C., Demory, J., Gomez, C., Sagnes, I., Lanzillotti Kimura, N., Lemaitre, A., Auffeves, A., White, A., Lanco, L., & Senellart, P. (n.d.). Near optimal single photon sources in the solid state [Article]. *ArXiv.Org*, *10*(5), 340–345. https://doi.org/10.1038/nphoton.2016.23

[67] Yu-Ming He, Yu He, Yu-Jia Wei, Dian Wu, Mete Atatüre, Christian Schneider, Sven Höfling, Martin Kamp, Chao-Yang Lu, & Jian-Wei Pan. (n.d.). On-demand semiconductor single-photon source with near-unity indistinguishability [Article]. *Nature Nanotechnology*, *8*(3), 213. https://doi.org/10.1038/nnano.2012.262

[68] Trivedi, R., Fischer, K. A., Vučković, J., & Müller, K. (n.d.). Generation of Non-Classical Light Using Semiconductor Quantum Dots [Article]. *Advanced Quantum Technologies*, *3*(1), n/a-n/a. https://doi.org/10.1002/qute.201900007

[69] Sipahigil, A., Jahnke, K. D., Rogers, L. J., Teraji, T., Isoya, J., Zibrov, A. S., Jelezko, F., & Lukin, M. D. (n.d.). Indistinguishable photons from separated silicon-vacancy centers in diamond [Article]. *Physical Review Letters*, *113*(11), 113602–113602. https://doi.org/10.1103/PhysRevLett.113.113602

[70] Sipahigil, A., Goldman, M. L., Togan, E., Chu, Y., Markham, M., Twitchen, D. J., Zibrov, A. S., Kubanek, A., & Lukin, M. D. (n.d.). Quantum interference of single photons from remote nitrogen-vacancy centers in diamond [Article]. *Physical Review Letters*, *108*(14), 143601–143601. https://doi.org/10.1103/PhysRevLett.108.143601

[71] Sun, S., Kim, H., Luo, Z., Solomon, G. S. & Waks, E. (2016). Quantum memory. *Science*, *361*(6397), 57–60. https://doi.org/10.1088/0953-4075/45/12/120201

[72] Gao, W. B. (2015). Coherent manipulation, measurement and entanglement of individual solid-state spins using optical fields. [Article]. *Nature Photonics*, *9*(6), 363–374. https://doi.org/10.1038/nphoton.2015.58

[73] Awschalom, D., Bassett, L., Dzurak, A., Hu, E., & Petta, J. (n.d.). Quantum Spintronics: Engineering and Manipulating Atom-Like Spins in Semiconductors [Article]. *Science*, *339*(6124), 1174–1179. https://doi.org/10.1126/science.1231364

[74] Zhong, T., Kindem, J. M., Bartholomew, J. G., Rochman, J., Craiciu, I., Miyazono, E., Bettinelli, M., Cavalli, E., Verma, V., Nam, S. W., Marsili, F., Shaw, M. D., Beyer, A. D., & Faraon, A. (n.d.). Nanophotonic rare-earth quantum memory with optically controlled retrieval [Article]. *Science (New York, N.Y.)*, *357*(6358), 1392. https://doi.org/10.1126/science.aan5959

[75] Rondin, L., Tetienne, J.-P., Hingant, T., Roch, J.-F., Maletinsky, P., & Jacques, V. (n.d.). Magnetometry with nitrogen-vacancy defects in diamond [Article]. *Reports on Progress in Physics*, *77*(5), 056503. https://doi.org/10.1088/0034-4885/77/5/056503

[76] F. Dolde, H. Fedder, M. W. Doherty, T. Nöbauer, F. Rempp, G. Balasubramanian, T. Wolf, F. Reinhard, L. C. L. Hollenberg, F. Jelezko, & J. Wrachtrup. (n.d.). Electric-field sensing using single diamond spins [Article]. *Nature Physics*, *7*(6), 459. https://doi.org/10.1038/nphys1969

[77] Zaitsev, A. M. (2001). *Optical Properties of Diamond A Data Handbook* (1st ed. 2001.) [Book].

[78] Doherty, M. W., Manson, N. B., Delaney, P., Jelezko, F., Wrachtrup, J., & Hollenberg, L. C. L. (2013). The nitrogen-vacancy colour centre in diamond. *Physics Reports*, *528*(1), 1–45. https://doi.org/10.1016/j.physrep.2013.02.001

[79] Sild, Olev., & Haller, Kristjan. (1988). *Zero-Phonon Lines And Spectral Hole Burning in Spectroscopy and Photochemistry* (O. Sild & K. Haller, Eds.; 1st ed. 1988.) [Book].

[80] Kurtsiefer, Mayer, Zarda, & Weinfurter. (n.d.). Stable solid-state source of single photons [Article]. *Physical Review Letters*, *85*(2), 290. https://doi.org/10.1103/PhysRevLett.85.290

[81] Brouri, R., Beveratos, A., Poizat, J. P., & Grangier, P. (2000). Photon antibunching in the fluorescence of individual color centers in diamond [Article]. *Optics Letters*, *25*(17), 1294–1296. https://doi.org/10.1364/OL.25.001294

[82] Drabenstedt, A., Fleury, L., Tietz, C., Jelezko, F., Kilin, S., Nizovtzev, A., & Wrachtrup, J. (1999). Low-temperature microscopy and spectroscopy on single defect centers in diamond [Article]. *Physical Review. B*, *60*(16), 11503–11508. https://doi.org/10.1103/PhysRevB.60.11503

[83] Bogdanov, S. I., Makarova, O. A., Lagutchev, A. S., Shah, D., Chiang, C.-C., Saha, S., Baburin, A. S., Ryzhikov, I. A., Rodionov, I. A., Kildishev, A. v., Boltasseva, A., & Shalaev, V. M. (2019). *Deterministic integration of single nitrogen-vacancy centers into nanopatch antennas*. http://arxiv.org/abs/1902.05996

[84] Okubo, R., Hirano, M., Zhang, Y., & Hirano, T. (n.d.). Pulse-resolved measurement of quadrature phase amplitudes of squeezed pulse trains at a repetition rate of 76 MHz [Article]. *Optics Letters*, *33*(13), 1458. https://doi.org/10.1364/OL.33.001458

[85] Khalid, A., Chung, K., Rajasekharan, R., Lau, D. W. M., Karle, T. J., Gibson, B. C., & Tomljenovic-Hanic, S. (2015). Lifetime reduction and enhanced emission of single photon color centers in nanodiamond via surrounding refractive index modification. *Scientific Reports*, *5*(June), 1–12. https://doi.org/10.1038/srep11179

[86] Laube, C., Oeckinghaus, T., Lehnert, J., Griebel, J., Knolle, W., Denisenko, A., Kahnt, A., Meijer, J., Wrachtrup, J., & Abel, B. (2019). Controlling the fluorescence properties of nitrogen vacancy centers in nanodiamonds. *Nanoscale*, *11*(4), 1770–1783. https://doi.org/10.1039/c8nr07828a

[87] Bradac, C., Gaebel, T., Naidoo, N., Sellars, M. J., Twamley, J., Brown, L. J., Barnard, A. S., Plakhotnik, T., Zvyagin, A. v., & Rabeau, J. R. (2010). Observation and control of blinking nitrogen-vacancy centres in discrete nanodiamonds. *Nature Nanotechnology*, *5*(5), 345–349. https://doi.org/10.1038/nnano.2010.56

[88] Chung, P.-H., Perevedentseva, E., & Cheng, C.-L. (2007). The particle size-dependent photoluminescence of nanodiamonds [Article]. *Surface Science*, *601*(18), 3866–3870. https://doi.org/10.1016/j.susc.2007.04.150

[89] Reineck, P., Capelli, M., Lau, D. W. M., Jeske, J., Field, M. R., Ohshima, T., Greentree, A. D., & Gibson, B. C. (2017). Bright and photostable nitrogen-vacancy fluorescence from unprocessed detonation nanodiamond. *Nanoscale*, *9*(2), 497–502. https://doi.org/10.1039/c6nr07834f

[90] Reineck, P., Lau, D. W. M., Wilson, E. R., Nunn, N., Shenderova, O. A., & Gibson, B. C. (2018). Visible to near-IR fluorescence from single-digit detonation nanodiamonds: Excitation wavelength and pH dependence. *Scientific Reports*, *8*(1), 2–8. https://doi.org/10.1038/s41598-018-20905-0

[91] Martinovich, V. A., Turukhin, A. v., Zaitsev, A. M., & Gorokhovsky, A. A. (2003). Photoluminescence spectra of xenon implanted natural diamonds. *Journal of Luminescence*, *102–103*(SPEC), 785–790. https://doi.org/10.1016/S0022-2313(02)00642-7

[92] Li, Q., Wang, T., Su, Y., Yan, M., & Qiu, M. (2010). Coupled mode theory analysis of mode-splitting in coupled cavity system. *Optics Express*, *18*(8), 8367. https://doi.org/10.1364/oe.18.008367

[93] Huang, W. (1991). *Coupled-Mode Theory*. *19*(10), 1505–1518.

[94] Popovic, M., Manolatou, C., & Watts, M. (2006). Coupling-induced resonance frequency shifts in coupled dielectric multi-cavity filters. *Optics Express*, *14*(3), 1208. https://doi.org/10.1364/oe.14.001208

[95] Huxter, M., Oliver, T. A. A., Budker, D., & Fleming, G. R. (2013). Vibrational and electronic ultrafast relaxation of the nitrogen-vacancy centers in diamond. *EPJ Web of Conferences*, *41*, 6–8. https://doi.org/10.1051/epjconf/20134104009

[96] Vadym N. Mochalin, Olga Shenderova, Dean Ho, & Yury Gogotsi. (n.d.). The properties and applications of nanodiamonds [Article]. *Nature Nanotechnology*, *7*(1), 11. https://doi.org/10.1038/nnano.2011.209

[97] Lindner, S., Bommer, A., Muzha, A., Krueger, A., Gines, L., Mandal, S., Williams, O., Londero, E., Gali, A., & Becher, C. (n.d.). Strongly inhomogeneous distribution of spectral properties of silicon-vacancy color centers in nanodiamonds [Article]. *ArXiv.Org*, *20*(11), 1–14. https://doi.org/10.1088/1367-2630/aae93f

[98] Lindner, S., Bommer, A., Muzha, A., Krueger, A., Gines, L., Mandal, S., Williams, O., Londero, E., Gali, A., & Becher, C. (2018). Strongly inhomogeneous distribution of spectral properties of silicon-vacancy color centers in nanodiamonds. *New Journal of Physics*, *20*(11), 115002. https://doi.org/10.1088/1367-2630/aae93f

[99] Trinh, C. T., Lee, J., & Lee, K. G. (2018). Fluorescent impurity emitter in toluene and its photon emission properties. *Scientific Reports*, *8*(1), 1–8. https://doi.org/10.1038/s41598-018-26686-w

[100] Song, H.-Z. (2020). The Development of Quantum Emitters Based on Semiconductor Quantum Dots. In P. Yu & Z. M. Wang (Eds.), *Quantum Dot Optoelectronic Devices* (pp. 83–106). Springer International Publishing. https://doi.org/10.1007/978-3-030-35813-6_3

[101] Cheung, J. Y., Chunnilall, C. J., Woolliams, E. R., Fox, N. P., Mountford, J. R., Wang, J., & Thomas, P. J. (n.d.). The quantum candela: a re-definition of the standard units for optical radiation [Article]. *Journal of Modern Optics*, *54*(2–3), 373–396. https://doi.org/10.1080/09500340600769521

[102] Beveratos, A., Brouri, R., Gacoin, T., Villing, A., Poizat, J.-P., & Grangier, P. (n.d.). Single Photon Quantum Cryptography [Article]. *Physical Review Letters*, *89*(18), 187901–187901. https://doi.org/10.1103/physrevlett.89.187901

[103] Aspuru-Guzik, A., & Walther, P. (n.d.). Photonic quantum simulators [Article]. *Nature Physics*, *8*(4), 285–291. https://doi.org/10.1038/nphys2253

[104] Kok, P., Munro, W. J., Nemoto, K., Ralph, T. C., Dowling, J. P., & Milburn, G. J. (n.d.). Linear optical quantum computing with photonic qubits [Article]. *Reviews of Modern Physics*, *79*(1), 135–174. https://doi.org/10.1103/revmodphys.79.135

[105] O'Brien, J. L., Furusawa, A., & Vučković, J. (n.d.). Photonic quantum technologies [Article]. *Nature Photonics*, *3*(12), 687–695. https://doi.org/10.1038/nphoton.2009.229

[106] Yonezu, Y., Wakui, K., Furusawa, K., Takeoka, M., Semba, K., & Aoki, T. (n.d.). Efficient Single-Photon Coupling from a Nitrogen-Vacancy Center Embedded in a Diamond Nanowire Utilizing an Optical Nanofiber [Article]. *Scientific Reports*, *7*(1), 12985–12989. https://doi.org/10.1038/s41598-017-13309-z

[107] Sild, Olev., & Haller, Kristjan. (1988). *Zero-Phonon Lines And Spectral Hole Burning in Spectroscopy and Photochemistry* (Olev. Sild & Kristjan. Haller, Eds.; 1st ed. 1988.) [Book]. Springer Berlin Heidelberg. https://doi.org/10.1007/978-3-642-73638-4

[108] Doherty, M. W., Manson, N. B., Delaney, P., Jelezko, F., Wrachtrup, J., & Hollenberg, L. C. L. (2013). The nitrogen-vacancy colour centre in diamond [Article]. *Physics Reports*, *528*(1), 1–45. https://doi.org/10.1016/j.physrep.2013.02.001

[109] Rondin, L., Tetienne, J.-P., Hingant, T., Roch, J.-F., Maletinsky, P., & Jacques, V. (2014). Magnetometry with nitrogen-vacancy defects in diamond [Article]. *Reports on Progress in Physics*, *77*(5), 056503–056503. https://doi.org/10.1088/0034-4885/77/5/056503

[110] Royal Melbourne Institute of Technology University Details Findings in Nitrogen (Bright and photostable nitrogen-vacancy fluorescence from unprocessed detonation nanodiamond). (2017). [Article]. In *Nanotechnology Weekly* (p. 410). NewsRX LLC.

[111] Recent Findings in Nitrogen Described by C. Laube and Colleagues (Controlling the fluorescence properties of nitrogen vacancy centers in nanodiamonds). (2019). [Article]. In *Chemicals & Chemistry* (p. 2633). NewsRX LLC.

[112] Gaebel, T., Sellars, M. J., Barnard, A. S., Brown, L. J., Bradac, C., Naidoo, N., Rabeau, J. R., Twamley, J., Plakhotnik, T., & Zvyagin, A. v. (2010). Observation and control of blinking nitrogen-vacancy centres in discrete nanodiamonds [Article]. *Nature Nanotechnology*, *5*(5), 345–349. https://doi.org/10.1038/nnano.2010.56

[113] Wong, H. Y., Braga, N., & Mickevicius, R. V. (n.d.). Prediction of highly scaled hydrogen-terminated diamond MISFET performance based on calibrated TCAD simulation [Article]. *Diamond & Related Materials*, *80*, 14–17. https://doi.org/10.1016/j.diamond.2017.10.004

[114] Fu, Y., Xu, R., Xu, Y., Zhou, J., Wu, Q., Kong, Y., Zhang, Y., Chen, T., & Yan, B. (2018). Characterization and Modeling of Hydrogen-Terminated MOSFETs with Single-Crystal and Polycrystalline Diamond. *IEEE Electron Device Letters*, *39*(11), 1704–1707. https://doi.org/10.1109/LED.2018.2870668

[115] Rashid, S. J., Tajani, A., Twitchen, D. J., Coulbeck, L., Udrea, F., Butler, T., Rupesinghe, N. L., Brezeanu, M., Isberg, J., Garraway, A., Dixon, M., Balmer, R. S., Chamund, D., Taylor, P., & Amaratunga, G. A. J. (2008). Numerical parameterization of Chemical-Vapor-Deposited (CVD) single-crystal diamond for device simulation and analysis. *IEEE Transactions on Electron Devices*, *55*(10), 2744–2756. https://doi.org/10.1109/TED.2008.2003225

[116] Yin, Z., Tordjman, M., Lee, Y., Vardi, A., Kalish, R., & del Alamo, J. A. (2018). Enhanced transport in transistor by tuning transition-metal oxide electronic states interfaced with diamond. *Science Advances*, *4*(9). https://doi.org/10.1126/sciadv.aau0480

[117] Jürgen Ristein. (n.d.). Surface Transfer Doping of Semiconductors [Article]. *Science (American Association for the Advancement of Science)*, *313*(5790), 1057–1058.

[118] Chakrapani, V., Angus, J. C., Anderson, A. B., Wolter, S. D., Stoner, B. R., & Sumanasekera, G. U. (n.d.). Charge Transfer Equilibria Between Diamond and an Aqueous Oxygen Electrochemical Redox Couple [Article]. *Science (American Association for the Advancement of Science)*, *318*(5855), 1424–1430. https://doi.org/10.1126/science.1148841

[119] Xia, F., Shao, Z., He, Y., Wang, R., Wu, X., Jiang, T., Duhm, S., Zhao, J., Lee, S.-T., & Jie, J. (n.d.). Surface Charge Transfer Doping via Transition Metal Oxides for Efficient p-Type Doping of II–VI Nanostructures [Article]. *ACS Nano*, *10*(11), 10283–10293. https://doi.org/10.1021/acsnano.6b05884

[120] Xiang, D., Han, C., Wu, J., Zhong, S., Liu, Y., Lin, J., Zhang, X.-A., Ping Hu, W., Özyilmaz, B., Neto, A. H. C., Wee, A. T. S., & Chen, W. (n.d.). Surface transfer doping induced effective modulation on ambipolar characteristics of few-layer black phosphorus [Article]. *Nature Communications*, *6*(1), 6485–6485. https://doi.org/10.1038/ncomms7485

[121] Yang, J., Xiao, Y., Deng, Y., Duhm, S., Ueno, N., Lee, S., Li, Y., & Tang, J. (n.d.). Electric-Field-Assisted Charge Generation and Separation Process in Transition Metal Oxide-Based Interconnectors for Tandem Organic Light-Emitting Diodes [Article]. *Advanced Functional Materials*, *22*(3), 600–608. https://doi.org/10.1002/adfm.201102136

[122] Chen, Z., Santoso, I., Wang, R., Xie, L. F., Mao, H. Y., Huang, H., Wang, Y. Z., Gao, X. Y., Chen, Z. K., Ma, D., Wee, A. T. S., & Chen, W. (n.d.). Surface transfer hole doping of epitaxial graphene using MoO3 thin film [Article]. *Applied Physics Letters*, *96*(21), 213104. https://doi.org/10.1063/1.3441263

[123] Russell, S. A. O., Cao, L., Qi, D., Tallaire, A., Crawford, K. G., Wee, A. T. S., & Moran, D. A. J. (n.d.). Surface transfer doping of diamond by MoO3: A combined spectroscopic and Hall measurement study [Article]. *Applied Physics Letters*, *103*(20), 202112. https://doi.org/10.1063/1.4832455

[124] Tordjman, M., Saguy, C., Bolker, A., & Kalish, R. (n.d.). Superior Surface Transfer Doping of Diamond with MoO3 [Article]. *Advanced Materials Interfaces*, *1*(3), 1300155-n/a. https://doi.org/10.1002/admi.201300155

[125] Crawford, K. G., Cao, L., Qi, D., Tallaire, A., Limiti, E., Verona, C., Wee, A. T. S., & Moran, D. A. J. (n.d.). Enhanced surface transfer doping of diamond by V2O5 with improved thermal stability [Article]. *Applied Physics Letters*, *108*(4), 42103. https://doi.org/10.1063/1.4940749

[126] Tordjman, M., Weinfeld, K., & Kalish, R. (n.d.). Boosting surface charge-transfer doping efficiency and robustness of diamond with WO3 and ReO3 [Article]. *Applied Physics Letters*, *111*(11), 111601. https://doi.org/10.1063/1.4986339

[127] Rashid, S. J., Tajani, A., Twitchen, D. J., Coulbeck, L., Udrea, F., Butler, T., Rupesinghe, N. L., Brezeanu, M., Isberg, J., Garraway, A., Dixon, M., Balmer, R. S., Chamund, D., Taylor, P., & Amaratunga, G. (2008). Numerical Parameterization of Chemical-Vapor-Deposited (CVD) Single-Crystal Diamond for Device Simulation and Analysis [Article]. *IEEE Transactions on Electron Devices*, *55*(10), 2744–2756. https://doi.org/10.1109/TED.2008.2003225

[128] Cui, J. B., Graupner, R., Ristein, J., & Ley, L. (1999). Electron affinity and band bending of single crystal diamond (111) surface. *Diamond and Related Materials*, *8*(2–5), 748–753. https://doi.org/10.1016/s0925-9635(98)00309-4

[129] Vasilopoulou, M., Kostis, I., Douvas, A. M., Georgiadou, D. G., Soultati, A., Papadimitropoulos, G., Stathopoulos, N. A., Savaidis, S. S., Argitis, P., & Davazoglou, D. (2013). Vapor-deposited hydrogenated and oxygen-deficient molybdenum oxide thin films for application in organic optoelectronics [Article]. *Surface & Coatings Technology*, *230*, 202–207. https://doi.org/10.1016/j.surfcoat.2013.05.033

[130] Kröger, M., Hamwi, S., Meyer, J., Riedl, T., Kowalsky, W., & Kahn, A. (2009). Role of the deep-lying electronic states of MoO3 in the enhancement of hole-injection in organic thin films. *Applied Physics Letters*, *95*(12), 2007–2010. https://doi.org/10.1063/1.3231928

[131] Balendhran, S., Deng, J., Ou, J. Z., Walia, S., Scott, J., Tang, J., Wang, K. L., Field, M. R., Russo, S., Zhuiykov, S., Strano, M. S., Medhekar, N., Sriram, S., Bhaskaran, M., & Kalantar-zadeh, K. (2013). Enhanced Charge Carrier Mobility in Two-Dimensional High Dielectric Molybdenum Oxide [Article]. *Advanced Materials (Weinheim)*, *25*(1), 109–114. https://doi.org/10.1002/adma.201203346

[132] Kamoun, O., Mami, A., Amara, M. A., Vidu, R., & Amlouk, M. (2019). Nanostructured Fe,Co-codoped MoO3 thin films. *Micromachines*, *10*(2). https://doi.org/10.3390/mi10020138

[133] BHAGAVANTAM, S., & NARAYANA RAO, D. A. A. S. (n.d.). Dielectric Constant of Diamond [Article]. *Nature (London)*, *161*(4097), 729–729. https://doi.org/10.1038/161729a0

[134] Rohlf, J. W. (1994). *Modern physics from [alpha] to Z^0* (1st ed.) [Book]. John Wiley.

[135] Richtmyer, F. K. (Floyd K. (1969). *Introduction to modern physics* (E. H. (Earle H. Kennard & J. N. Cooper, Eds.; 6th ed.) [Book]. McGraw-Hill.

[136] Dziechciarczyk, L., Zhu, S., Lin, D., Hawkins, T. W., Dong, L., Kemp, A., Nilsson, J., Savitski, V., Huang, Z., Demetriou, G., Cheng, D., Pidishety, S., Feng, Y., Feng, Y., Wang, G., & Lin, H. (2019). 9 W Average Power, 150 kHz Repetition Rate Diamond Raman Laser at 1519 nm, Pumped by a Yb Fibre Amplifier [Proceeding]. *2019 Conference on Lasers and Electro-Optics Europe & European Quantum Electronics Conference (CLEO/Europe-EQEC)*, 1–1. https://doi.org/10.1109/CLEOE-EQEC.2019.8873181

[137] Fedyanin, D. Y., & Agio, M. (2016). Ultrabright single-photon source on diamond with electrical pumping at room and high temperatures [Article]. *New Journal of Physics*, *18*(7), 73012. https://doi.org/10.1088/1367-2630/18/7/073012

[138] Kao, K.-C. (2004). *Dielectric phenomena in solids with emphasis on physical concepts of electronic processes* [Book]. Academic Press.

[139] Claeys, C., & Simoen, E. (2013). *Radiation Effects in Advanced Semiconductor Materials and Devices* [Book]. Springer Berlin / Heidelberg.

[140] Nebel, C. E. (2003). Electronic properties of CVD diamond [Article]. *Semiconductor Science and Technology*, *18*(3), S1–S11. https://doi.org/10.1088/0268-1242/18/3/301

[141] Abakumov, V. N. (1991). *Nonradiative recombination in semiconductors* (V. I. (Vladimir I. Perel & I. N. Yassievich, Eds.) [Book]. North-Holland.

[142] Smirnov, B. M. (2012). *Fundamentals of ionized gases : basic topics in plasma physics* [Book].

[143] Volpe, P.-N., Pernot, J., Muret, P., & Omnès, F. (2009). High hole mobility in boron doped diamond for power device applications [Article]. *Applied Physics Letters*, *94*(9), 092102-092102–092103. https://doi.org/10.1063/1.3086397

[144] Storteboom, J., Dolan, P., Castelletto, S., Li, X., & Gu, M. (2015). Lifetime investigation of single nitrogen vacancy centres in nanodiamonds [Article]. *Optics Express*, *23*(9), 11327–11333. https://doi.org/10.1364/OE.23.011327

[145] Roychoudhury, R., Charlson, E. J., Stacy, T., Hajsaid, M., Charlson, E. M., & Meese, J. M. (1997). Growth and characterization of phosphorus doped diamond films using trimethyl phosphite as the doping source. *Journal of Applied Physics*, *81*(8), 3644–3646. https://doi.org/10.1063/1.365483

[146] Takeuchi, D., Ri, S. G., Kato, H., Nebel, C. E., & Yamasaki, S. (2005). Total photoyield experiments on hydrogen terminated n-type diamond. *Diamond and Related Materials*, *14*(11–12), 2019–2022. https://doi.org/10.1016/j.diamond.2005.08.061

[147] Grotz, B., Hauf, M. v., Dankerl, M., Naydenov, B., Pezzagna, S., Meijer, J., Jelezko, F., Wrachtrup, J., Stutzmann, M., Reinhard, F., & Garrido, J. A. (2012). Charge state manipulation of qubits in diamond. *Nature Communications*, *3*. https://doi.org/10.1038/ncomms1729

[148] W. B. Gao, A. Imamoglu, H. Bernien, & R. Hanson. (n.d.). Coherent manipulation, measurement and entanglement of individual solid-state spins using optical fields [Article]. *Nature Photonics*, *9*(6), 363. https://doi.org/10.1038/nphoton.2015.58

[149] O'Brien, J. L. (n.d.). Optical Quantum Computing [Article]. *Science (American Association for the Advancement of Science)*, *318*(5856), 1567–1570. https://doi.org/10.1126/science.1142892

[150] Moerner WE. (2015). Single-molecule spectroscopy and imaging over the decades. [Other]. In *Faraday discussions* (Vol. 184, p. 9). https://doi.org/10.1039/c5fd00149h

[151] Sydor AM. (2015). Super-Resolution Microscopy: From Single Molecules to Supramolecular Assemblies. [Other]. In *Trends in cell biology* (Vol. 25, Issue 12, p. 730). https://doi.org/10.1016/j.tcb.2015.10.004

[152] Pelton, M. (2015). Modified spontaneous emission in nanophotonic structures. [Article]. *Nature Photonics*, *9*(7), 427–436. https://doi.org/10.1038/nphoton.2015.103

[153] Riedrich-Möller, J., Pezzagna, S., Meijer, J., Pauly, C., Mücklich, F., Markham, M., Edmonds, A. M., & Becher, C. (n.d.). Nanoimplantation and Purcell enhancement of single nitrogen-vacancy centers in photonic crystal cavities in diamond [Article]. *Applied Physics Letters*, *106*(22), 221103. https://doi.org/10.1063/1.4922117

[154] Wolters, J. (2010). Enhancement of the zero phonon line emission from a single nitrogen vacancy center in a nanodiamond via coupling to a photonic crystal cavity. [Article]. *Applied Physics Letters*, *97*(14), 141108–141111. https://doi.org/10.1063/1.3499300

[155] Albrecht, R. (2014). Narrow-band single photon emission at room temperature based on a single nitrogen-vacancy center coupled to an all-fiber-cavity. [Article]. *Applied Physics Letters*, *105*(7), 1–5. https://doi.org/10.1063/1.4893612

[156] Koenderink AF. (2017). Single-Photon Nanoantennas. [Other]. In *ACS photonics* (Vol. 4, Issue 4, p. 710). https://doi.org/10.1021/acsphotonics.7b00061

[157] Jeong CY. (2013). Circular hybrid plasmonic waveguide with ultra-long propagation distance. [Other]. In *Optics express* (Vol. 21, Issue 14, p. 17404). https://doi.org/10.1364/OE.21.017404

[158] Kang JH. (2011). Room-temperature high-Q channel-waveguide surface plasmon nanocavity. [Other]. In *Optics express* (Vol. 19, Issue 15, p. 13892). https://doi.org/10.1364/OE.19.013892

[159] Ren-Min Ma. (2011). Room-temperature sub-diffraction-limited plasmon laser by total internal reflection. [Article]. *Nature Materials*, *10*(2), 110–114. https://doi.org/10.1038/nmat2919

[160] Oulton, R. F. (2009). Plasmon lasers at deep subwavelength scale. [Article]. *Nature*, *461*(7264), 629–633. https://doi.org/10.1038/nature08364

[161] Hill MT. (2009). Lasing in metal-insulator-metal sub-wavelength plasmonic waveguides. [Other]. In *Optics express* (Vol. 17, Issue 13, p. 11107).

[162] Soon-Hong Kwon, Ju-Hyung Kang, Sun-Kyung Kim, & Hong-Gyu Park. (n.d.). Surface Plasmonic Nanodisk/Nanopan Lasers [Article]. *IEEE Journal of Quantum Electronics*, *47*(10), 1346–1353. https://doi.org/10.1109/JQE.2011.2166537

[163] Soon-Hong Kwon. (2010). Subwavelength Plasmonic Lasing from a Semiconductor Nanodisk with Silver Nanopan Cavity. [Article]. *Nano Letters*, *10*(9), 3679–3684. https://doi.org/10.1021/nl1021706

[164] Seo MK. (2009). Full three-dimensional subwavelength high-Q surface-plasmon-polariton cavity. [Other]. In *Nano letters* (Vol. 9, Issue 12, p. 4078). https://doi.org/10.1021/nl902274m

[165] Wencheng Yue. (2017). Surface plasmon polariton nanocavity with ultrasmall mode volume. [Article]. *Journal of Physics: D Applied Physics*, *50*(31), 1–2. https://doi.org/10.1088/1361-6463/aa77ed

[166] Kuttge M. (2010). Ultrasmall mode volume plasmonic nanodisk resonators. [Other]. In *Nano letters* (Vol. 10, Issue 5, p. 1537). https://doi.org/10.1021/nl902546r

[167] Nozaki, K., Kita, S., & Baba, T. (n.d.). Room temperature continuous wave operation and controlled spontaneous emission in ultrasmall photonic crystal nanolaser [Article]. *Optics Express*, *15*(12), 7506–7514. https://doi.org/10.1364/OE.15.007506

[168] Park, H.-G. (2004). Electrically Driven Single-Cell Photonic Crystal Laser. [Article]. *Science*, *305*(5689), 1444–1448. https://doi.org/10.1126/science.1100968

[169] Painter O. (1999). Two-dimensional photonic band-Gap defect mode laser [Other]. In *Science (New York, N.Y.)* (Vol. 284, Issue 5421, p. 1819).

[170] Kim, Y.-H., Kwon, S.-H., Lee, J. M., Hwang, M.-S., Kang, J.-H., Park, W. il, & Park, H.-G. (2012). Graphene-contact electrically driven microdisk lasers [Article]. *Nature Communications*, *3*(1), 1123–1123. https://doi.org/10.1038/ncomms2137

[171] Song, Q. (2009). Near-IR subwavelength microdisk lasers. [Article]. *Applied Physics Letters*, *94*(6), N.PAG. https://doi.org/10.1063/1.3081106

[172] Liu Liu. (2010). An ultra-small, low-power, all-optical flip-flop memory on a silicon chip. [Article]. *Nature Photonics*, *4*(3), 182–188. https://doi.org/10.1038/nphoton.2009.268

[173] Seo, M.-K., Yang, J.-K., Jeong, K.-Y., Park, H.-G., Qian, F., Ee, H.-S., No, Y.-S., & Lee, Y.-H. (n.d.). Modal Characteristics in a Single-Nanowire Cavity with a Triangular Cross Section [Article]. *Nano Letters*, *8*(12), 4534–4538. https://doi.org/10.1021/nl8027125

[174] Duan, X. (2003). Single-nanowire electrically driven lasers. [Article]. *Nature*, *421*(6920), 241–246. https://doi.org/10.1038/nature01353

[175] Huang MH. (2001). Room-temperature ultraviolet nanowire nanolasers. [Other]. In *Science (New York, N.Y.)* (Vol. 292, Issue 5523, p. 1897).

[176] Lu, C.-Y. (2010). Metal-cavity surface-emitting microlaser at room temperature. [Article]. *Applied Physics Letters*, *96*(25), 251101–251102. https://doi.org/10.1063/1.3455316

[177] Nezhad, M. P. (2010). Room-temperature subwavelength metallo-dielectric lasers. [Article]. *Nature Photonics*, *4*(6), 395–400. https://doi.org/10.1038/nphoton.2010.88

[178] Yu K. (2010). Subwavelength metal-optic semiconductor nanopatch lasers. [Other]. In *Optics express* (Vol. 18, Issue 9, p. 8790). https://doi.org/10.1364/OE.18.008790

[179] Hill, M. T., Oei, Y. S., Smalbrugge, E., Zhu, Y. C., Vries, de, Veldhoven, van, Otten, van, Eijkemans, T. J., Turkiewicz, J. P., Waardt, de, Geluk, E. J., Kwon, S.-H., Lee, Y.-H., Nötzel, R., & Smit, M. K. (2007). Lasing in metallic-coated nano-cavities [Article]. *Nature Photonics*, *1*(10), 589–594.

[180] Sipahigil, A. (2016). An integrated diamond nanophotonics platform for quantum-optical networks. [Article]. *Science*, *354*(6314), 847–851.

[181] Bogdanov, S. I., Shalaginov, M. Y., Lagutchev, A. S., Chiang, C.-C., Shah, D., Baburin, A. S., Ryzhikov, I. A., Rodionov, I. A., Kildishev, A. v, Boltasseva, A., & Shalaev, V. M. (2018). Ultrabright Room-Temperature Sub-Nanosecond Emission from Single Nitrogen-Vacancy Centers Coupled to Nanopatch Antennas. *Nano Letters*, *8*, 4837–4844.

[182] Shackleford, J. A. (2009). Integrated plasmonic lens photodetector. [Article]. *Applied Physics Letters*, *94*(8), 083501–083504. https://doi.org/10.1063/1.3086898

[183] Doherty, M. W., Manson, N. B., Delaney, P., Jelezko, F., Wrachtrup, J., & Hollenberg, L. C. L. (2013). The nitrogen-vacancy colour centre in diamond [Article]. *Physics Reports*, *528*(1), 1–45. https://doi.org/10.1016/j.physrep.2013.02.001

[184] Bulu, I., Babinec, T., Hausmann, B., Choy, J. T., & Loncar, M. (n.d.). Plasmonic resonators for enhanced diamond NV-center single photon sources [Article]. *Optics Express*, *19*(6), 5268–5276. https://doi.org/10.1364/OE.19.005268

[185] Kwon, S.-H., No, Y.-S., & Park, H.-G. (2014). Design of plasmonic cavities. *Nano Convergence*, *1*(1), 1–9. https://doi.org/10.1186/s40580-014-0008-4

[186] Vuckovic, J., Painter, O., Yong Xu, Yariv, A., & Scherer, A. (n.d.). Finite-difference time-domain calculation of the spontaneous emission coupling factor in optical microcavities [Article]. *IEEE Journal of Quantum Electronics*, *35*(8), 1168–1175. https://doi.org/10.1109/3.777216

[187] Björk, G., Heitmann, H., & Yamamoto, Y. (1993). Spontaneous-emission coupling factor and mode characteristics of planar dielectric microcavity lasers [Article]. *Physical Review. A, Atomic, Molecular, and Optical Physics*, *47*(5), 4451–4463. https://doi.org/10.1103/PhysRevA.47.4451

[188] Yokoyama, H., Nishi, K., Anan, T., Nambu, Y., Brorson, S. D., Ippen, E. P., & Suzuki, M. (n.d.). Controlling spontaneous emission and threshold-less laser oscillation with optical microcavities [Article]. *Optical and Quantum Electronics*, *24*(2), S245–S272. https://doi.org/10.1007/BF00625827

[189] Brorson, S. D., Yokoyama, H., & Ippen, E. P. (n.d.). Spontaneous emission rate alteration in optical waveguide structures [Article]. *IEEE Journal of Quantum Electronics*, *26*(9), 1492–1499. https://doi.org/10.1109/3.102626

[190] Kristensen, P. T., & Hughes, S. (n.d.). Modes and Mode Volumes of Leaky Optical Cavities and Plasmonic Nanoresonators [Article]. *ACS Photonics*, *1*(1), 2–10. https://doi.org/10.1021/ph400114e

[191] Englund D. (2005). Controlling the spontaneous emission rate of single quantum dots in a two-dimensional photonic crystal. [Other]. In *Physical review letters* (Vol. 95, Issue 1, p. 013904).

[192] Hausmann, B., Bulu, I., Babinec, T., Khan, M., Hemmer, P., & Loncar, M. (2010). Top-down fabricated hybrid diamond-plasmon nanoparticles [Proceeding]. *CLEO/QELS: 2010 Laser Science to Photonic Applications*, 1–2. https://doi.org/10.1364/CLEO.2010.CMFF3

[193] Kurtsiefer, C., Mayer, S., Zarda, P., & Weinfurter, H. (2000). Stable solid-state source of single photons [Article]. *Physical Review Letters*, *85*(2), 290–293. https://doi.org/10.1103/PhysRevLett.85.290

[194] Doherty, M. W., Manson, N. B., Delaney, P., Jelezko, F., Wrachtrup, J., & Hollenberg, L. C. L. (2013). The nitrogen-vacancy colour centre in diamond [Article]. *Physics Reports*, *528*(1), 1–45. https://doi.org/10.1016/j.physrep.2013.02.001

[195] Fraczek, E., Savitski, V. G., Dale, M., Breeze, B. G., Diggle, P., Markham, M., Bennett, A., Dhillon, H., Newton, M. E., & Kemp, A. J. (2017). Laser spectroscopy of NV- and NV0 colour centres in synthetic diamond [Article]. *Optical Materials Express*, *7*(7), 2571–2585. https://doi.org/10.1364/OME.7.002571

[196] Zaitsev, A. M. (2001). *Optical Properties of Diamond A Data Handbook* (1st ed. 2001.) [Book]. Springer Berlin Heidelberg. https://doi.org/10.1007/978-3-662-04548-0

[197] Davies, G., & Hamer, M. F. (1976). Optical Studies of the 1.945 eV Vibronic Band in Diamond [Article]. *Proceedings of the Royal Society of London. Series A, Mathematical and Physical Sciences*, *348*(1653), 285–298. https://doi.org/10.1098/rspa.1976.0039

[198] Prawer, S., Rabeau, J. R., Hemmer, P. R., Wittmann, C., Greentree, A. D., Twamley, J., Meijer, J., Domhan, M., Wrachtrup, J., Gaebel, T., Jelezko, F., Popa, I., Neumann, P., & Stavrias, N. (2006). Room-temperature coherent coupling of single spins in diamond [Article]. *Nature Physics*, *2*(6), 408–413. https://doi.org/10.1038/nphys318

[199] Baldwin, J. W., Zalalutdinov, M., Butler, J. E., Feygelson, T., & Houston, B. H. (2005). 2D photonic crystals fabricated in wide bandgap nanocrystalline diamond [Proceeding]. *Proceedings of SPIE*, *6002*(1), 600213–600219. https://doi.org/10.1117/12.631871

[200] Wang, C. F., Hanson, R., Awschalom, D. D., Hu, E. L., Feygelson, T., Yang, J., & Butler, J. E. (2007). Fabrication and characterization of two-dimensional photonic crystal microcavities in nanocrystalline diamond [Article]. *Applied Physics Letters*, *91*(20), 201112-201112–201113. https://doi.org/10.1063/1.2813023

[201] Wang, C. F., Choi, Y.-S., Lee, J. C., Hu, E. L., Yang, J., & Butler, J. E. (2007). Observation of whispering gallery modes in nanocrystalline diamond microdisks [Article]. *Applied Physics Letters*, *90*(8), 081110-081110–081113. https://doi.org/10.1063/1.2709626

[202] Schietinger, S., Barth, M., Aichele, T., & Benson, O. (2009). Plasmon-Enhanced Single Photon Emission from a Nanoassembled Metal−Diamond Hybrid Structure at Room Temperature [Article]. *Nano Letters*, *9*(4), 1694–1698. https://doi.org/10.1021/nl900384c

[203] Barclay, P. E., Santori, C., Fu, K.-M., Beausoleil, R. G., & Painter, O. (2009). Coherent interference effects in a nano-assembled diamond NV center cavity-QED system [Article]. *Optics Express*, *17*(10), 8081–8097. https://doi.org/10.1364/OE.17.008081

[204] Rivoire, K., Faraon, A., & Vuckovic, J. (2008). Gallium phosphide photonic crystal nanocavities in the visible [Article]. *Applied Physics Letters*, *93*(6), 063103-063103–3. https://doi.org/10.1063/1.2971200

[205] Gould, M., Schmidgall, E. R., Dadgostar, S., Hatami, F., & Fu, K.-M. C. (2016). Efficient Extraction of Zero-Phonon-Line Photons from Single Nitrogen-Vacancy Centers in an Integrated GaP-on-Diamond Platform [Article]. *Physical Review Applied*, *6*(1). https://doi.org/10.1103/PhysRevApplied.6.011001

[206] Sumikura, H., Hirama, K., Nishiguchi, K., Shinya, A., & Notomi, M. (2020). Highly nitrogen-vacancy doped diamond nanostructures fabricated by ion implantation and optimum annealing [Article]. *APL Materials*, *8*(3), 31113-031113–031117. https://doi.org/10.1063/5.0001922

[207] Yu, Y., Wu, L., & Zhi, J. (2014). Diamond Nanowires: Fabrication, Structure, Properties, and Applications [Article]. *Angewandte Chemie (International Ed.)*, *53*(52), 14326–14351. https://doi.org/10.1002/anie.201310803

[208] Hausmann, B. J. M., Khan, M., Zhang, Y., Babinec, T. M., Martinick, K., McCutcheon, M., Hemmer, P. R., & Lončar, M. (2010). Fabrication of diamond nanowires for quantum information processing applications. *Diamond and Related Materials*, *19*(5–6), 621–629. https://doi.org/10.1016/j.diamond.2010.01.011

[209] Maier, S. A. (2006). Effective Mode Volume of Nanoscale Plasmon Cavities [Article]. *Optical and Quantum Electronics*, *38*(1), 257–267. https://doi.org/10.1007/s11082-006-0024-7

[210] Huang, S., Ming, T., Lin, Y., Ling, X., Ruan, Q., Palacios, T., Wang, J., Dresselhaus, M., & Kong, J. (2016). Ultrasmall Mode Volumes in Plasmonic Cavities of Nanoparticle-On-Mirror Structures [Article]. *Small (Weinheim an Der Bergstrasse, Germany)*, *12*(37), 5190–5199. https://doi.org/10.1002/smll.201601318

[211] Choy, J. T., Hausmann, B. J. M., Babinec, T. M., Bulu, I., Khan, M., Maletinsky, P., Yacoby, A., & Loňar, M. (2011). Enhanced single-photon emission from a diamond-Silver aperture [Article]. *Nature Photonics*, *5*(12), 738–743. https://doi.org/10.1038/nphoton.2011.249

[212] Siampour, H., Kumar, S., & Bozhevolnyi, S. I. (2017). Chip-integrated plasmonic cavity-enhanced single nitrogen-vacancy center emission. *Nanoscale*, *9*(45), 17902–17908. https://doi.org/10.1039/c7nr05675c

[213] Bogdanov, S., Shalaginov, M. Y., Lagutchev, A., Chiang, C.-C., Shah, D., Baburin, A. S., Ryzhikov, I. A., Rodionov, I. A., Boltasseva, A., & Shalaev, V. M. (2018). Ultrabright Room-Temperature Emission from Single Plasmon-Enhanced Nitrogen-Vacancy Centers in Diamond. *2018 Conference on Lasers and Electro-Optics, CLEO 2018 - Proceedings*.

[214] Kumar, S., Lausen, J. L., Garcia-Ortiz, C. E., Andersen, S. K. H., Roberts, A. S., Radko, I. P., Smith, C. L. C., Kristensen, A., & Bozhevolnyi, S. I. (2015). Excitation of surface plasmon polariton modes with multiple nitrogen vacancy centers in single nanodiamonds [Article]. *Journal of Optics (2010)*, *18*(2), 24002. https://doi.org/10.1088/2040-8978/18/2/024002

[215] Trusheim, M. E., Sakakibara, R., Karamlou, A., & Englund, D. (2017). Embedded plasmonic nanoantennas for enhanced diamond NV-spin readout [Proceeding]. *2017 Conference on Lasers and Electro-Optics Europe & European Quantum Electronics Conference (CLEO/Europe-EQEC)*, 1–1. https://doi.org/10.1109/CLEOE-EQEC.2017.8087661

[216] Grotz, B., Hauf, M. v, Dankerl, M., Naydenov, B., Pezzagna, S., Meijer, J., Jelezko, F., Wrachtrup, J., Stutzmann, M., Reinhard, F., & Garrido, J. A. (2012). Charge state manipulation of qubits in diamond [Article]. *Nature Communications*, *3*(1), 729–729. https://doi.org/10.1038/ncomms1729

[217] Fedyanin, D. Y., & Agio, M. (2016). Ultrabright single-photon source on diamond with electrical pumping at room and high temperatures [Article]. *New Journal of Physics*, *18*(7), 73012. https://doi.org/10.1088/1367-2630/18/7/073012

[218] Doi, Y., Makino, T., Kato, H., Takeuchi, D., Ogura, M., Okushi, H., Morishita, H., Tashima, T., Miwa, S., Yamasaki, S., Neumann, P., Wrachtrup, J., Suzuki, Y., & Mizuochi, N. (2014). Deterministic electrical charge-state initialization of single nitrogen-vacancy center in diamond [Article]. *Physical Review. X*, *4*(1), 011057. https://doi.org/10.1103/PhysRevX.4.011057

[219] New Mineralogy Study Findings Have Been Reported by Researchers at Synopsys, Inc. (Prediction of highly scaled hydrogen-terminated diamond MISFET performance based on calibrated TCAD simulation). (2018). [Article]. In *Chemicals & Chemistry* (p. 2476). NewsRX LLC.

[220] Yin, Z., Tordjman, M., Lee, Y., Vardi, A., Kalish, R., & del Alamo, J. A. (2018). Enhanced transport in transistor by tuning transition-metal oxide electronic states interfaced with diamond [Article]. *Science Advances*, *4*(9), eaau0480–eaau0480. https://doi.org/10.1126/sciadv.aau0480

[221] Rashid, S. J., Tajani, A., Twitchen, D. J., Coulbeck, L., Udrea, F., Butler, T., Rupesinghe, N. L., Brezeanu, M., Isberg, J., Garraway, A., Dixon, M., Balmer, R. S., Chamund, D., Taylor, P., & Amaratunga, G. (n.d.). Numerical Parameterization of Chemical-Vapor-Deposited (CVD) Single-Crystal Diamond for Device Simulation and Analysis [Article]. *IEEE Transactions on Electron Devices*, *55*(10), 2744–2756. https://doi.org/10.1109/TED.2008.2003225

[222] Cui, J. B., Ristein, J., & Ley, L. (1998). Electron affinity of the bare and hydrogen covered single crystal diamond (111) surface [Article]. *Physical Review Letters*, *81*(2), 429–432. https://doi.org/10.1103/PhysRevLett.81.429

[223] NARAYANA RAO, D. A. A. S., & BHAGAVANTAM, S. (1948). Dielectric Constant of Diamond [Article]. *Nature (London)*, *161*(4097), 729–729. https://doi.org/10.1038/161729a0

[224] Yu, S., Xu, J., Kato, H., Yang, N., Schulte, A., Schönherr, H., & Jiang, X. (2019). Phosphorus-Doped Nanocrystalline Diamond for Supercapacitor Application [Article]. *ChemElectroChem*, *6*(4), 1088–1093. https://doi.org/10.1002/celc.201801543

[225] Pinault-Thaury, M.-A., Temgoua, S., Gillet, R., Bensalah, H., Stenger, I., Jomard, F., Issaoui, R., & Barjon, J. (2019). Phosphorus-doped (113) CVD diamond: A breakthrough towards bipolar diamond devices [Article]. *Applied Physics Letters*, *114*(11), 112106. https://doi.org/10.1063/1.5079924

[226] Rashid, S. J., Tajani, A., Twitchen, D. J., Coulbeck, L., Udrea, F., Butler, T., Rupesinghe, N. L., Brezeanu, M., Isberg, J., Garraway, A., Dixon, M., Balmer, R. S., Chamund, D., Taylor, P., & Amaratunga, G. (2008). Numerical Parameterization of Chemical-Vapor-Deposited (CVD) Single-Crystal Diamond for Device Simulation and Analysis [Article]. *IEEE Transactions on Electron Devices*, *55*(10), 2744–2756. https://doi.org/10.1109/TED.2008.2003225

[227] Chelvayohan, M., & Mee, C. H. B. (1982). Work function measurements on (110), (100) and (111) surfaces of silver [Article]. *Journal of Physics. C, Solid State Physics*, *15*(10), 2305–2312. https://doi.org/10.1088/0022-3719/15/10/029

[228] Storteboom, J., Dolan, P., Castelletto, S., Li, X., & Gu, M. (2015). Lifetime investigation of single nitrogen vacancy centres in nanodiamonds [Article]. *Optics Express*, *23*(9), 11327–11333. https://doi.org/10.1364/OE.23.011327

[229] Kristensen, P. T., & Hughes, S. (2014). Modes and Mode Volumes of Leaky Optical Cavities and Plasmonic Nanoresonators [Article]. *ACS Photonics*, *1*(1), 2–10. https://doi.org/10.1021/ph400114e

[230] Yonezu, Y., Wakui, K., Furusawa, K., Takeoka, M., Semba, K., & Aoki, T. (2017). Efficient Single-Photon Coupling from a Nitrogen-Vacancy Center Embedded in a Diamond Nanowire Utilizing an Optical Nanofiber [Article]. *Scientific Reports*, *7*(1), 12985–12989. https://doi.org/10.1038/s41598-017-13309-z

[231] Szenes, A., Bánhelyi, B., Csendes, T., Szabó, G., & Csete, M. (2018). Enhancing Diamond Fluorescence via Optimized Nanorod Dimer Configurations [Article]. *Plasmonics (Norwell, Mass.)*, *13*(6), 1977–1985. https://doi.org/10.1007/s11468-018-0713-7

[232] BJ Shields, Q. U. N. L. H. P. M. L. (2015). Efficient readout of a single spin state in diamond via spin-to-charge conversion. *Phys. Rev. Lett.*, *114*(13), 136402. https://doi.org/10.1103/physrevlett.114.136402

[233] D Hopper, H. S. L. B. (2018). Spin readout techniques of the nitrogen-vacancy center in diamond. *Micromachines*, *9*(9), 437. https://doi.org/10.3390/mi9090437

[234] Irber, D. M., Poggiali, F., Kong, F., Kieschnick, M., Lühmann, T., Kwiatkowski, D., Meijer, J., Du, J., Shi, F., & Reinhard, F. (2021). Robust all-optical single-shot readout of nitrogen-vacancy centers in diamond. *Nature Communications 2021 12:1*, *12*(1), 1–6. https://doi.org/10.1038/s41467-020-20755-3

[235] Fedyanin, D. Y., & Agio, M. (2016). Ultrabright single-photon source on diamond with electrical pumping at room and high temperatures [Article]. *New Journal of Physics*, *18*(7), 73012. https://doi.org/10.1088/1367-2630/18/7/073012

[236] Yin, Z., Tordjman, M., Lee, Y., Vardi, A., Kalish, R., & del Alamo, J. A. (2018). Enhanced transport in transistor by tuning transition-metal oxide electronic states interfaced with diamond [Article]. *Science Advances*, *4*(9), eaau0480–eaau0480. https://doi.org/10.1126/sciadv.aau0480

[237] Gogolides, E., Constantoudis, V., Kokkoris, G., Kontziampasis, D., Tsougeni, K., Boulousis, G., Vlachopoulou, M., & Tserepi, A. (2011). Controlling roughness: from etching to nanotexturing and plasma-directed organization on organic and inorganic materials [Article]. *Journal of Physics. D, Applied Physics*, *44*(17), 174021. https://doi.org/10.1088/0022-3727/44/17/174021

[238] Hicks, M.-L., Pakpour-Tabrizi, A. C., Zuerbig, V., Kirste, L., Nebel, C., & Jackman, R. B. (2019). Optimizing reactive ion etching to remove sub-surface polishing damage on diamond [Article]. *Journal of Applied Physics*, *125*(24), 244502. https://doi.org/10.1063/1.5094751

[239] Zheng, Y., Liu, J., Zhang, R., Cumont, A., Wang, J., Wei, J., Ye, H., & Li, C. (2020). Fast smoothing on diamond surface by inductively coupled plasma reactive ion etching [Article]. *Journal of Materials Research*, *35*(5), 462–472. https://doi.org/10.1557/jmr.2019.369

[240] Muchnikov, A. B., Vikharev, A. L., Butler, J. E., Chernov, V. v, Isaev, V. A., Bogdanov, S. A., Okhapkin, A. I., Yunin, P. A., & Drozdov, Y. N. (2015). Homoepitaxial growth of CVD diamond after ICP pretreatment [Article]. *Physica Status Solidi. A, Applications and Materials Science*, *212*(11), 2572–2577. https://doi.org/10.1002/pssa.201532171

[241] Novak, A. v, & Novak, V. R. (2013). Roughness of amorphous, polycrystalline and hemispherical-grained silicon films [Article]. *Technical Physics Letters*, *39*(10), 858–861. https://doi.org/10.1134/S106378501310009X

[242] Kim, J.-H., Moon, S., Kim, J.-W., Lee, D., Park, B. C., Kim, D.-H., Jeong, Y., Hand, S., Osborne, J., de Wolf, P., Kim, Y. S., & Shin, C. (2019). Advanced measurement and diagnosis of the effect on the underlayer roughness for industrial standard metrology [Article]. *Scientific Reports*, *9*(1), 1018–1018. https://doi.org/10.1038/s41598-018-36991-z

[243] Petrovic, R., Strbac, S., Bundaleski, N., & Rakocevic, Z. (2001). Surface roughness minimum: Ag thin layer deposited on a glass [Article]. *Journal of the Serbian Chemical Society*, *66*(7), 483–490. https://doi.org/10.2298/JSC0107483P

[244] Ruch, J. G. (1972). Electron dynamics in short channel field-effect transistors [Article]. *IEEE Transactions on Electron Devices*, *19*(5), 652–654. https://doi.org/10.1109/T-ED.1972.17468

[245] Jyegal, J. (2015). Velocity overshoot decay mechanisms in compound semiconductor field-effect transistors with a submicron characteristic length [Article]. *AIP Advances*, *5*(6), 67118-067118–13. https://doi.org/10.1063/1.4922332

[246] Smith, J., Monroy-Ruz, J., Rarity, J. G., & C. Balram, K. (2020). Single photon emission and single spin coherence of a nitrogen vacancy center encapsulated in silicon nitride [Article]. *Applied Physics Letters*, *116*(13), 134001. https://doi.org/10.1063/5.0002709

[247] Chiang, C.-C., Bogdanov, S. I., Makarova, O. A., Xu, X., Saha, S., Shah, D., Wang, D., Lagutchev, A. S., Kildishev, A. v, Boltasseva, A., & Shalaev, V. M. (2020). A Quantum Plasmonic Launcher for Integrated Ultrafast Single-Photon Sources [Proceeding]. *2020 Conference on Lasers and Electro-Optics (CLEO)*, 1–2.

[248] Khramtsov, I. A., & Fedyanin, D. Y. (2020). On-demand generation of high-purity single-photon pulses by NV centers in diamond under electrical excitation. *Optics InfoBase Conference Papers*. https://doi.org/10.1364/FIO.2020.FW4C.7

VITA

Education and Experience

Purdue University, West Lafayette, IN, 2016 – 2021

PhD., Dept. of Electrical and Computer Engineering (advisor: Peter A. Bermel)

GPA: 3.85/4.0

- Studied plasmonic designs for quantum emitter technologies including room temperature single photon sources
- Developed experimental techniques to characterize emission from doped nanodiamond samples
- Experimentally demonstrated novel lifetime shortening methods of room temperature quantum emitters
- Purdue Doctoral Fellowship
- Eta Kappa Nu Member
- Mentored undergraduate and graduate students in research.

U.S. Army, 2012-2016

- Equipped, trained, and managed a company of over 200 soldiers
- Managed accounts worth more than ten million dollars annually

University of Cincinnati, Cincinnati, OH, 2007-2012

B.S., College of Engineering, GPA: 3.62/4.0

- Quantum Algorithms curriculum
- Cum Laude

PUBLICATION

- O. Akomolede and P. Bermel, “Xenon implantation of nanodiamond films for targeted color center emission at sub-nanosecond time scales,” *Optical materials express*, vol. 11, no. 8, p. 2369, 2021, doi: 10.1364/OME.431743.

Skills

- **Fabrication:** Wet chemistry synthesis, Electrophoretic deposition, Sputtering, Ultrasonication techniques, Diamond film formation
- **Characterization:** Scanning Electron Microscope (SEM), Atomic Force Microscope (AFM), Furnace Operation, Fourier Transform Infrared Spectroscopy (FTIR), Scanning Confocal Microscopy, Automatic Probing
- **General:** High Vacuum Technology, Cleanroom Processing, Machine Learning
- **Programming:** MATLAB, Mathematica, C++, C, Python, Scheme
- **Software Packages:** Meep, Sentaurus, COMSOL